Fatigue Limit of Ni-based Superalloy 718 Fabricated by Additive Manufacturing: Quantitative Evaluation via Shear-mode Threshold and its Dominating Factor

朴, 成哲

https://hdl.handle.net/2324/7157349

出版情報：Kyushu University, 2023, 博士（工学）, 課程博士
バージョン：
権利関係：

Doctorate Dissertation in September 2023

Fatigue Limit of Ni-based Superalloy 718 Fabricated by Additive Manufacturing: Quantitative Evaluation *via* Shear-mode Threshold and its Dominating Factor

Supervisor: **Prof. Hisao Matsunaga**

Department of Hydrogen Energy Systems

Kyushu University

Park Sungcheol

Table of Content

1. Introduction

1.1 Research background

Ni-based superalloy 718 (Alloy 718) has gained significant popularity in extreme-temperature aerospace applications over the decades, owing to its outstanding mechanical properties, fatigue and creep resistance at high temperature up to 700 °C, as well as its exceptional corrosion resistance. In addition, it is known to have good weldability ascribed to its relatively sluggish precipitation kinetics [1–3]. The face-centered cubic (FCC) matrix of Alloy 718 contains a large percentage of alloying elements such as Cr, Nb and Mo, and small additions of Ti and Al [4,5]. The remarkable strength of the alloy is mainly attributed to the presence of coherent ordered, disc-shaped γ''-Ni_3Nb [6]. The γ'' precipitate is a metastable phase with a body-centered tetragonal (BCT) $D0_{22}$ crystal structure with lattice parameters a = 0.363 nm, and c = 0.741 nm [7,8]. With continued aging, this phase can undergo a transformation into the equilibrium, incoherent δ phase ($D0_a$ orthorhombic, Ni_3Nb) with lattice parameters a = 0.514 nm, b = 0.423, and c = 0.453 nm [8,9]. While the precipitation of the δ phase can indirectly enhance mechanical strength by suppressing grain growth during solution annealing and thus resulting in a microstructure of fine grain size, it also signifies the loss of strengthening γ'' phases due to the depletion of Nb elements, leading to severe degradation of mechanical properties [10–12]. In addition, some strengthening contribution also arises from coherent ordered γ' precipitates ($L1_2$ face-centered cubic, $Ni_3(Al,Ti)$) with a spheroidal/cuboidal morphology [6]. Fig. 1.1 showcases the aforementioned three phases observed *via* transmission electron microscope (TEM) [6,13]. On the other hand, Fig. 1.2 represents a schematic illustration of the crystal structures of the phases [14].

The excellent strength of Alloy 718 provides substantial benefits; nevertheless, they also pose challenges from a manufacturing technology standpoint. The conventional manufacturing methods for Alloy 718 components typically involve casting, forging, and machining processes. While these techniques have been widely used, they often entail complicated procedures and multiple manufacturing steps. Consequently, the production cycle becomes longer, which can result in cost inefficiencies for the overall process [15]. Given that this alloy is increasingly employed in aerospace applications requiring complex structural geometries such as turbine blades with internal cooling channels or intricate nozzles for liquid rocket engine injectors, the drawbacks of conventional manufacturing methods should become even more pronounced in this field [16,17]. As an illustrative example, Fig. 1.3 demonstrates the processes employed for the production of aero-engine discs through the conventional methods [18]. The production of the disc involves a series of sequential processes. Firstly, Alloy 718 billets are prepared through ingot metallurgy. This process begins with triple melting processes including vacuum induction melting, electro-slag remelting, and vacuum arc remelting. Once the billets are annealed for compositional homogeneity, they undergo thermal-mechanical working (*i.e.*, cogging) to break down the as-cast structure and reduce the grain size to acceptable levels. The *cast-and-wrought* billet, obtained through ingot metallurgy, is then subjected to a three-stage forging process, consisting of upsetting, blocking, and finishing. Finally, the forged disc undergoes machining to achieve precise final shape of the disc. It is important to note that these manufacturing steps are obviously inefficient and result in a significant loss of material.

To address these challenges, additive manufacturing (AM), also known as 3D printing, has emerged as a promising production method for Alloy 718 parts. This innovative approach offers the potential to realize the complicate geometry and achieve cost-effective production of Alloy 718 components, hence highly desirable in various fields, especially, in the aerospace sector [19]. As an example, Fig. 1.4 illustrates an AM fuel injector in the LE-9 engine [20], a hydrogen-fueled rocket engine for the first stage propulsion of H3 launch vehicle, newly developed by the Japan Aerospace Exploration Agency (JAXA) in collaboration with Mitsubishi Heavy Industries (MHI) [21–23]. Previously, the manufacturing process for this component involved the production of approximately 500 individual parts through machining and joining processes. However, by implementing AM technology, the fuel injector can now be manufactured as a single, unified part. This advancement has resulted in a remarkable reduction of the overall production time and cost [20].

Despite the numerous advantages of AM, the widespread adoption of the method for producing Alloy 718 parts is hindered by uncertainties regarding their mechanical integrity. This uncertainty is primarily due to the presence of small defects such as porosities and surface roughness and complex microstructural features, which will be discussed in detail in the following section. In the aerospace sector, where Alloy 718 is used as a major structural material, fatigue-related failures account for approximately 55% of all detected failures [24]. Therefore, it is of paramount importance to evaluate the fatigue strength of additively-manufactured (AM) Alloy 718 from the viewpoint of material strength design. Fatigue failures still remain a critical and unresolved concern for metallic parts, and specifically for the implementation of AM technologies in the industry. While the fatigue properties of conventionally manufactured Alloy 718, *i.e.*, wrought (WR) Alloy 718, are well-established and utilized for part design, it is expected that there will be deviations from these properties in AM alloy, which are relatively less explored [25]. This knowledge gap necessitates extensive research to bridge the understanding, and this thesis aims to contribute to filling this gap to the best of its abilities.

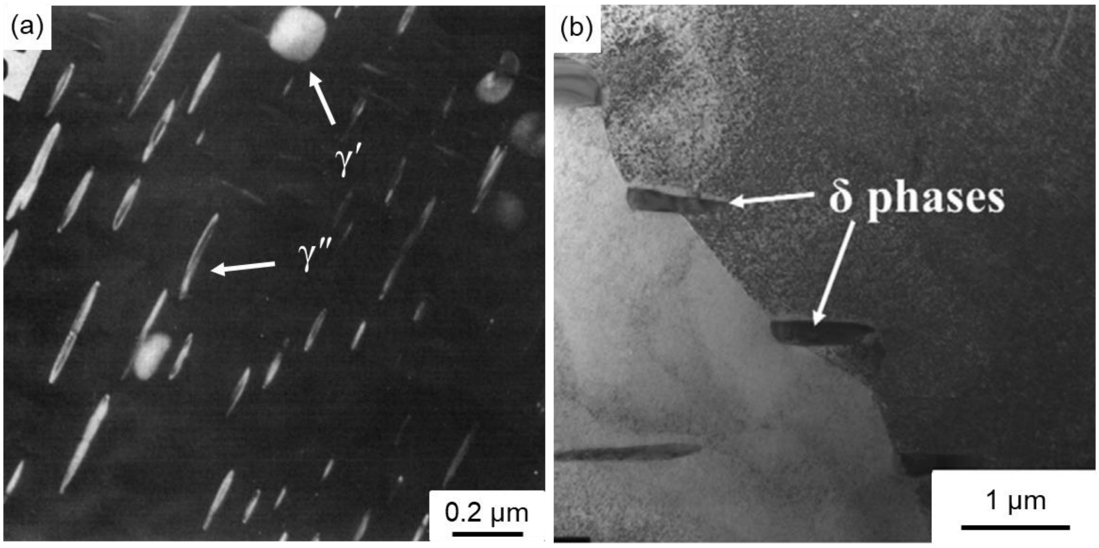

Fig. 1.1. (a) Dark field image viewed along a (001) direction of the microstructure of an Alloy 718 sample aged at 1073 K for 24 hours, illustrating the morphologies of γ' and γ'' particles [6]; (b) TEM micrograph showcasing δ phases along the grain boundary [13].

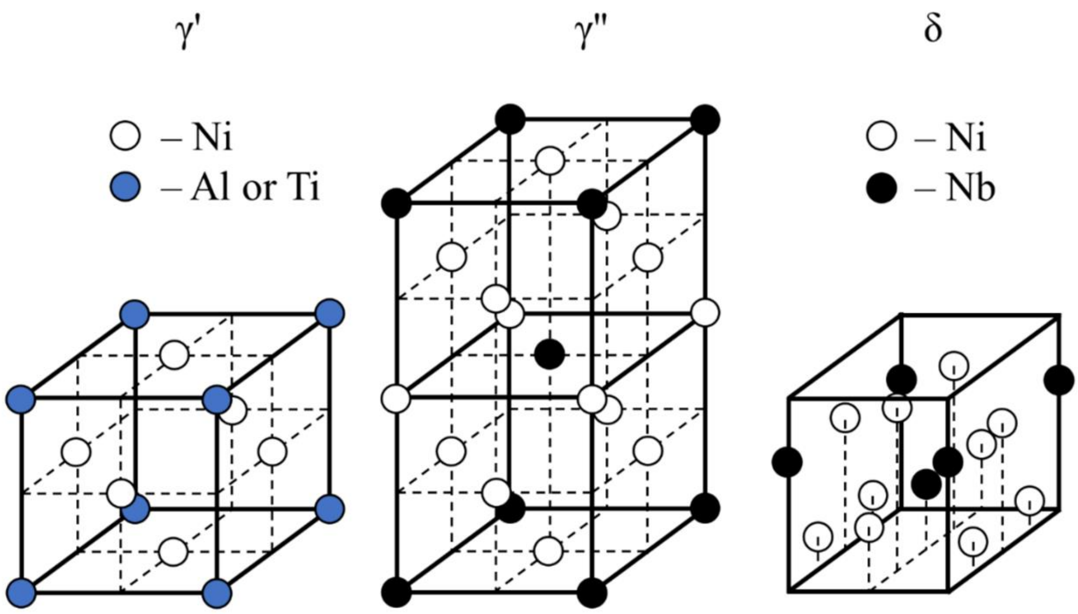

Fig. 1.2. Schematic illustration of the unit cell of γ′ phase (FCC $L1_2$), γ″ phase (BCT $D0_{22}$) and δ phase (orthorhombic $D0_a$). The open circles represent nickel atoms, blue solid circles represent either aluminum or titanium atoms and the black solid circles represent niobium atoms [14].

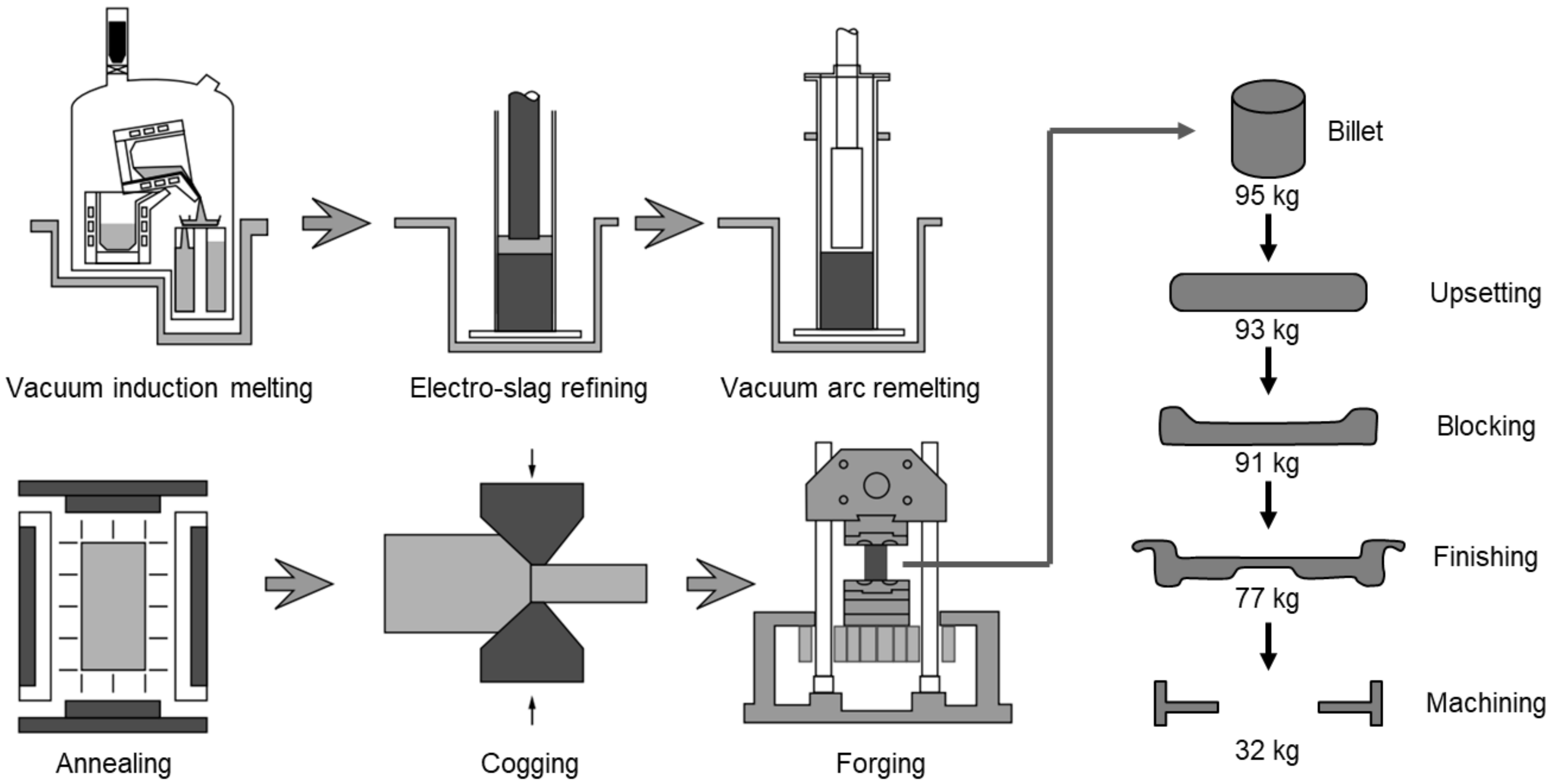

Fig. 1.3. Schematic illustration of sequential processes to produce aero-engine discs *via* conventional manufacturing methods [18].

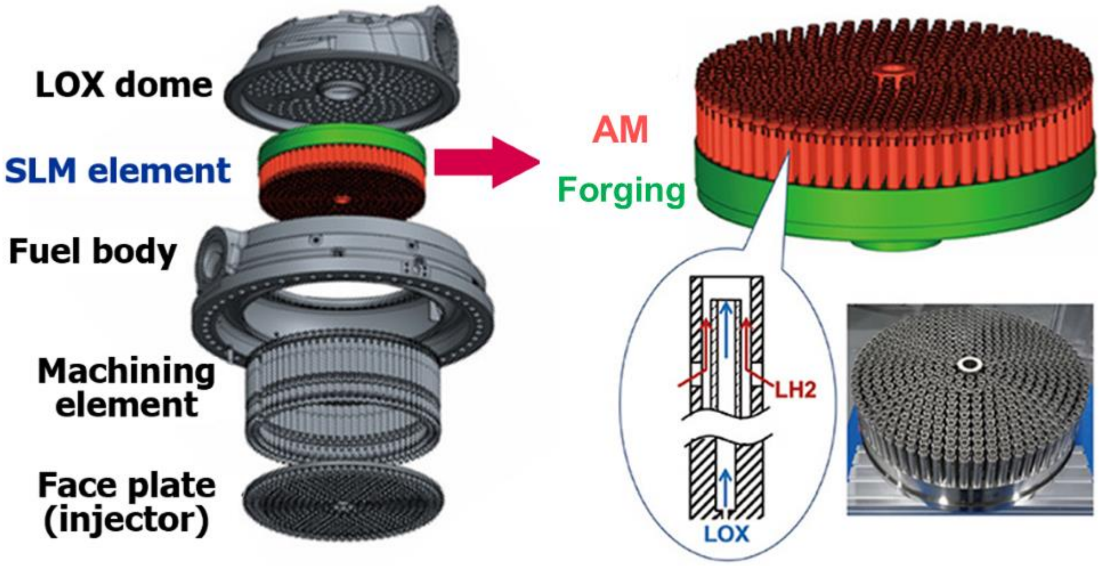

Fig. 1.4. Application of AM method in LE-9 engine fuel injector [20].

1.2 A brief introduction to additive manufacturing

As mentioned in the previous section, the presence of small defects and the intricate microstructure of AM materials introduce challenges in assessing fatigue strength. Therefore, it is essential to gain a comprehensive understanding of the impact of each factor on fatigue strength in order to ensure the structural integrity. Before commencing this exploration, it is crucial to provide a concise overview of key concepts of the AM method and the unique features of AM materials, in comparison to materials fabricated by conventional manufacturing methods. This initial step will establish a foundation for further examination of the topic.

1.2.1 Key concepts of AM method

Additive manufacturing is defined to be the "process of joining materials to make parts from 3D model data, usually layer upon layer, as opposed to subtractive manufacturing and formative manufacturing methodologies" [26]. Among the various categorized AM processes, our primary focus will be put on powder bed fusion (PBF). PBF has attracted considerable attention in recent years due to its capability to fabricate metal components with nearly complete density. The PBF falls into two categories depending on the energy sources as laser powder bed fusion (L-PBF) and electron beam powder bed fusion (E-PBF).

L-PBF, also known as selective laser melting (SLM), operates within a protective atmosphere, typically argon or nitrogen. Schematic illustration of L-PBF system is presented in Fig. 1.5 [27]. To begin the process, a layer of powder with a controlled thickness is uniformly spread on the build platform. The laser beam selectively irradiates specific areas of the powder layer based on a CAD model. The build platform is then lowered by the thickness of the new powder layer. A subsequent layer of powder is added on top of the preceding layer, and this process is repeated iteratively until the final object is fabricated. L-PBF is not limited to metals and can also be utilized for polymers, ceramics, and cermets [28]. Fig. 1.6 provides a schematic overview of the interaction between the laser beam and the powder bed [29]. When the laser beam irradiates the top surface of the powder bed, a small portion of the laser energy is dissipated through radiation and convection. Most of the laser energy is absorbed by the powder particles, causing them to heat up quickly and melt in localized areas. Once the laser moves away from the melted region, known as the molten pool, the molten material rapidly solidifies, resulting in the consolidation of the melt. This process enables the bonding of adjacent tracks and neighboring layers through fusion.

In L-PBF, there are four representative parameters to be considered for process optimization; laser power, scanning speed, hatch spacing, and layer thickness, as illustrated in Fig. 1.7 [30]. The combined influence of these parameters is quantified as the energy density which is the ratio of the energy beam power to the product of scanning speed, layer thickness, and hatch spacing. The product of scanning speed, layer thickness, and hatch spacing is referred to as the build rate [31]. Extensive research has demonstrated that the energy density has a significant impact on the microstructures and mechanical properties of AM components [32–34].

E-PBF functions similarly to L-PBF, with the difference of employing an electron beam as the heat source instead of a laser, as schematically presented in Fig. 1.8 [35]. The E-PBF process follows a four-step cycle: powder layer spreading, preheating, selective melting, and lowering of the build platform. The preheating step serves two purposes: sintering the powder bed using a defocused electron beam to establish good electrical conductivity for a stable process, and minimizing residual stresses [36,37]. Because E-PBF takes place within a vacuum chamber, the process helps reduce impurities, particularly for materials that are sensitive to oxygen [37]. On the other hand, to interact with the electron beam, the powder bed in E-PBF must possess conductivity, which restricts the applicability of E-PBF to conductive materials such as metals [28].

Regardless of the specific categories they belong to, AM technologies have the following advantages in common. Firstly, they allow for the production of complex or custom parts directly from the design shape, eliminating the need for expensive tools like punches, dies, or casting molds. Since intricate parts can be made in one step, the number of manufacturing steps can be dramatically reduced. Additionally, AM technique significantly reduces the number of parts by eliminating or reducing the need to assemble multiple components. It not only lowers the production cost but also reduces potential failure modes across joined parts. Moreover, the technology enables the achievement of superior performance than conventional manufacturing method by realizing mechanical, thermal, and other optimization approaches for the design of complex parts, incorporating internal features such as conformal cooling channels on combustion chambers or turbine blades [37,38].

1.2.2 Typical features of AM materials

Distinct characteristics in as-built AM materials, as compared with that of wrought (*i.e.*, forged or rolled) materials, can be summarized as strong crystallographic texture, micro-segregation, residual stress and defects. These AM features need to be thoroughly considered in view of fatigue design, particularly in critical applications such as aerospace. Since AM methods involve the localized and epitaxial solidification identical to traditional welding processes, they produce microstructures closely resembling those in multi-pass welds [39]. Therefore, as a first step to understand the AM features, it would be beneficial to refer to the underlying mechanism of the solidification behavior in the molten pool in welding process.

In fusion welding without a filler metal, crystals or grains at the solid-liquid interface between the base metal and the liquid metal, *i.e.*, the fusion boundary [40,41] grow into the molten pool, by making the atoms in the liquid follow the arrangement of atoms in the base metal grains. That is, the grains inherit the crystallographic orientation of the base metal grains [42], as depicted in Fig. 1.9 [43]. This growth process is referred to as epitaxial solidification. Once grain growth is initiated at the boundary of the molten pool, grains tend to grow along the direction perpendicular to the molten pool boundary, in which heat dissipates fastest. Simultaneously, grains are likely to grow in the easy-growth direction. The most favorable orientation for grain growth in FCC materials is the <001> direction [42]. Hence, grains with easy-growth direction perpendicular to the pool boundary can continue growing into the interior of the molten pool. On the other hand, grains with less favorable orientation with respect to the direction perpendicular to the boundary are impeded and grow only a limited distance [43] (*cf.* Fig. 1.9). This phenomenon is commonly known as competitive growth [44]. Similarly, in AM process, grain growth predominantly initiates at the solid-liquid interface, and grains in the newly-solidified materials are promoted to grow succeeding the crystallographic orientation of grains in materials adjoining the molten pool, and mainly along the build direction (BD) which is parallel to a global heat flux direction. Furthermore, through sequential solidification of AM, the re-melting of underlying layers facilitates the restart of the grain growth process, enabling it to span multiple layers. These two distinct mechanisms, *i.e.*, epitaxial solidification and competitive growth, are primarily responsible for the development of strong crystallographic texture with elongated grain morphology of AM materials [45].

Meanwhile, solidified microstructures can exhibit various sub-structures, which are governed by two parameters: the thermal gradient G and the solidification rate R. The G/R ratio determines the morphology of the structure, while the product of G and R, called the cooling rate, determines the size of the structure [46]. The impact of G/R and GR on the solidification structure is depicted in Fig. 1.10 [42]. According to G/R values, the solidification structure can be planar, cellular, columnar dendritic to equiaxed dendritic. On the other hand, as the cooling rate GR increases, all four structures become finer. Based on the numerical calculation of the G/R value *via* heat transfer and liquid metal flow model, Wei *et al*. [47] reported that during L-PBF process, the formation of either cellular or columnar dendritic structure is favorable. However, it is noted that the presence of various morphologies is possible due to variations in temperature gradient and solidification rate across different regions of the molten pool [48].

Micro-segregation is another microstructural feature observed in AM materials. During AM process, the rapid cooling in the highly localized melt pool results in a non-equilibrium solidification condition. Namely, there is limited time for the solute alloying elements in the liquid phase to diffuse back into the solid phase, leading to the micro-segregation of refractory alloying elements [39]. For as-built AM Alloy 718, the micro-segregation of alloying elements such as Nb brings about the precipitation of brittle particles such as Laves phases ($(Ni,Fe,Cr)_2(Nb,Mo,Ti)$) at the interdendritic regions, as reported in numerous literatures [49–51]. The high fraction of these particles is significantly undesirable since they are known to deplete beneficial alloying elements and promote the initiation and propagation of cracks, causing the degradation of the mechanical properties including tensile ductility, ultimate tensile strength, fracture toughness, and fatigue life [52,53]. Fig. 1.11 depicts the micro-segregation of refractory alloying elements, along with the evolution of solidification sub-structures in AM microstructure [54].

Residual stress is also a major concern that limits the widespread adoption of AM method. The process involves localized rapid heating and cooling steps, leading to significant thermal gradients in the molten pools. These non-uniform cooling rates and large thermal gradients inevitably accompany elevated levels of residual stress in AM materials [55]. Fig. 1.12 [55] illustrates a temperature-gradient mechanism suggested by Mercelis and Kruth [56] to describe the development of residual stress during AM. Firstly, the laser-beam irradiation of a new layer results in the uniform expansion of the layer. The expansion of the new layer is limited by the cooler underlying layers, leading to the formation of compressive stresses in the new layer and tensile stresses in the underlying part. Upon cooling, the new layer contracts at a faster rate than the underlying layers, causing tensile stresses in the new layer and compressive stresses in the layers below. However, it must be noted that the actual mechanism of residual stress generation in AM parts is much more complicated by the fact that new layers are not uniformly heated/melted but separately according to scan strategy [57]. The presence of high tensile residual stress can give rise to cracking, delamination, fatigue failure, and thermal deformation [58,59]. Therefore, to minimize the impact of residual stresses and improve the quality of AM parts, various techniques such as post heat treatment [60] and optimization of process parameters [39] can be employed.

Finally, the presence of small defects such as porosity and surface roughness is a long-standing and significant challenge observed in almost all of the metallic AM components ascribed to the processing nature [61]. Porosity can be categorized as either "powder-induced" or "process-induced", as depicted in Fig. 1.13(a) [62]. Powder-induced porosities refer to gas pores that may form within the powder feedstock during powder atomization. On the other hand, process-induced porosities result from improper process conditions. For instance, inadequate power supply can induce the generation of lack of fusion, which is characterized by an irregular shape and a range of sizes, from sub-micron to macroscopic, and can be identified by un-melted powders visible in or near the pore. Conversely, excessive power can cause vaporization of the metal from the melt pool, known as spatter ejection, leading to the formation of voids or poor surface quality [62]. Gas pores can also form due to the entrapment of shielding gas within the molten pool [44]. In addition to porosity, surface roughness is an unavoidable feature in as-built AM parts as shown in Fig. 1.13(b) [63]. Surface roughness can be attributed to several factors such as inherent stepwise layer-by-layer build which forms “staircases”, insufficient heat energy resulting in un-melted powders on the surface, or the liquid metal's contraction into a spherical shape driven by surface tension, known as the balling phenomenon [64–67]. The evolution of porosities and surface roughness during the AM process is schematically presented in Fig. 1.14 [61].

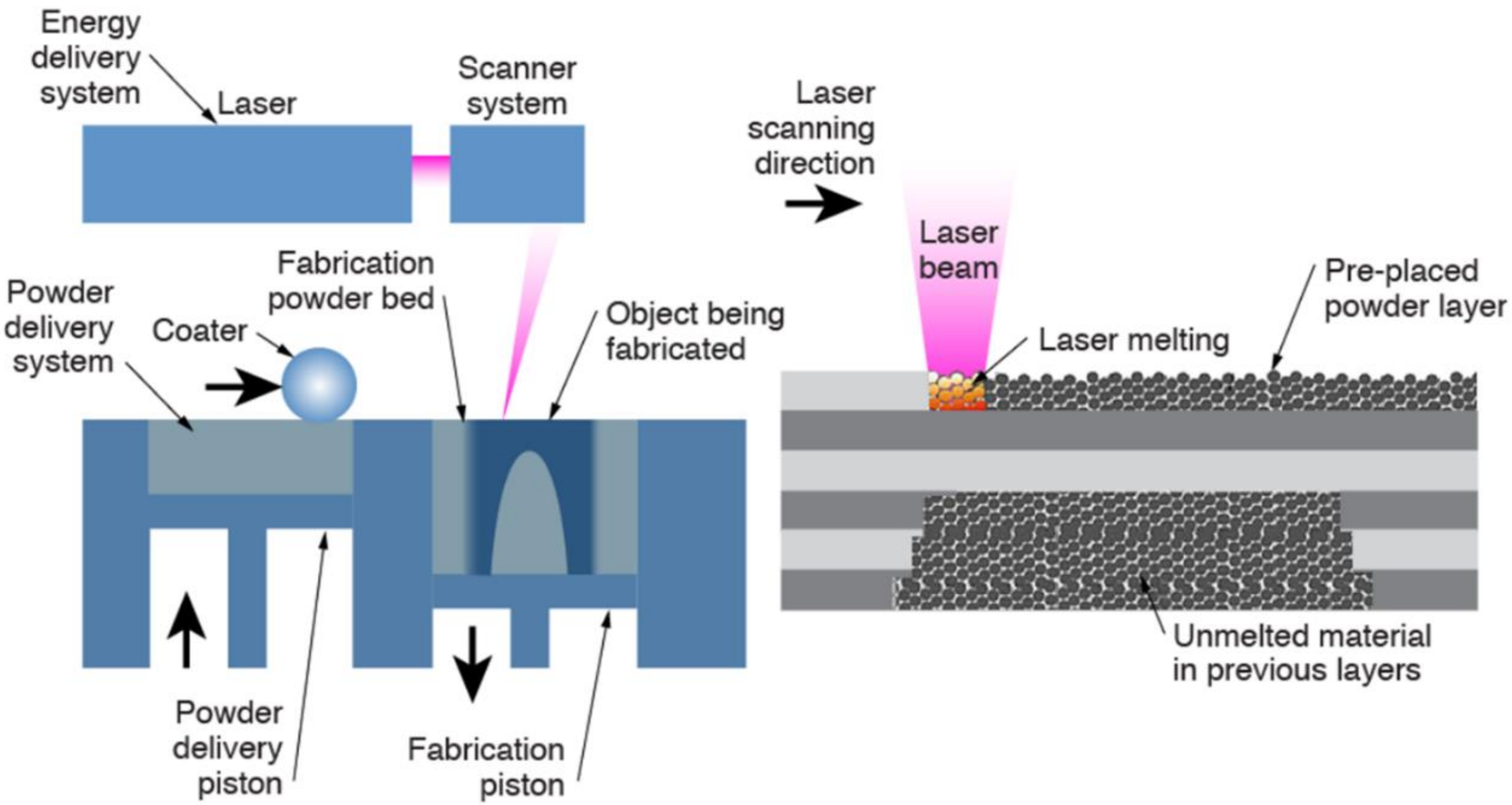

Fig. 1.5. Schematic overview of laser powder bed fusion (L-PBF) system [27].

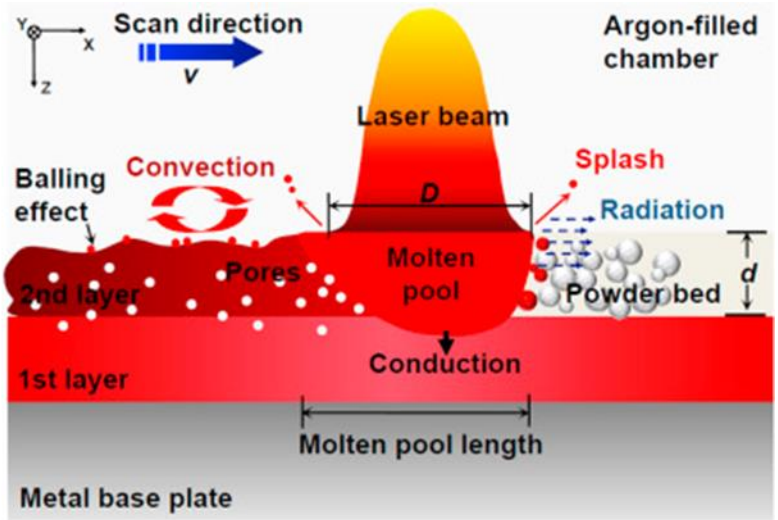

Fig. 1.6. Schematic illustration of the interaction between laser beam and powder bed [68].

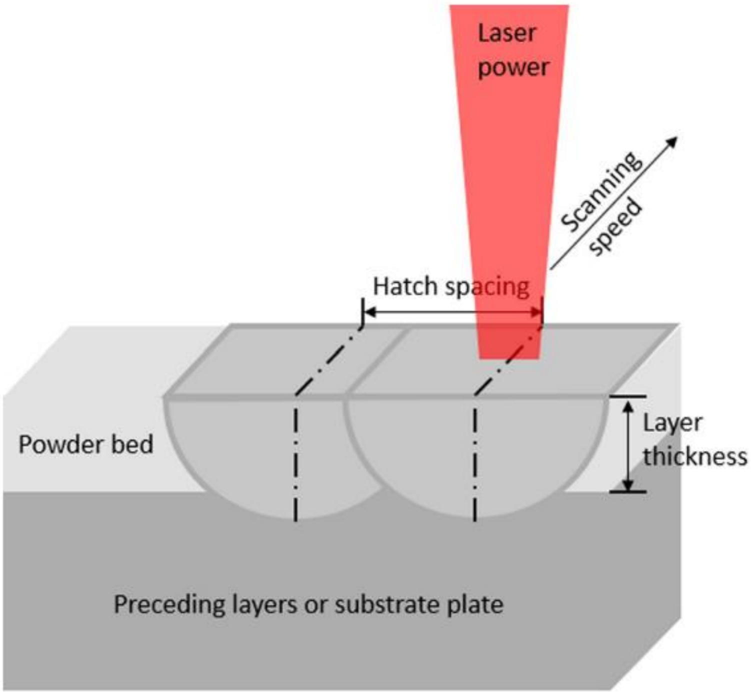

Fig. 1.7. Schematic illustration of L-PBF process parameters: laser power, scanning speed, hatch spacing, and layer thickness [30].

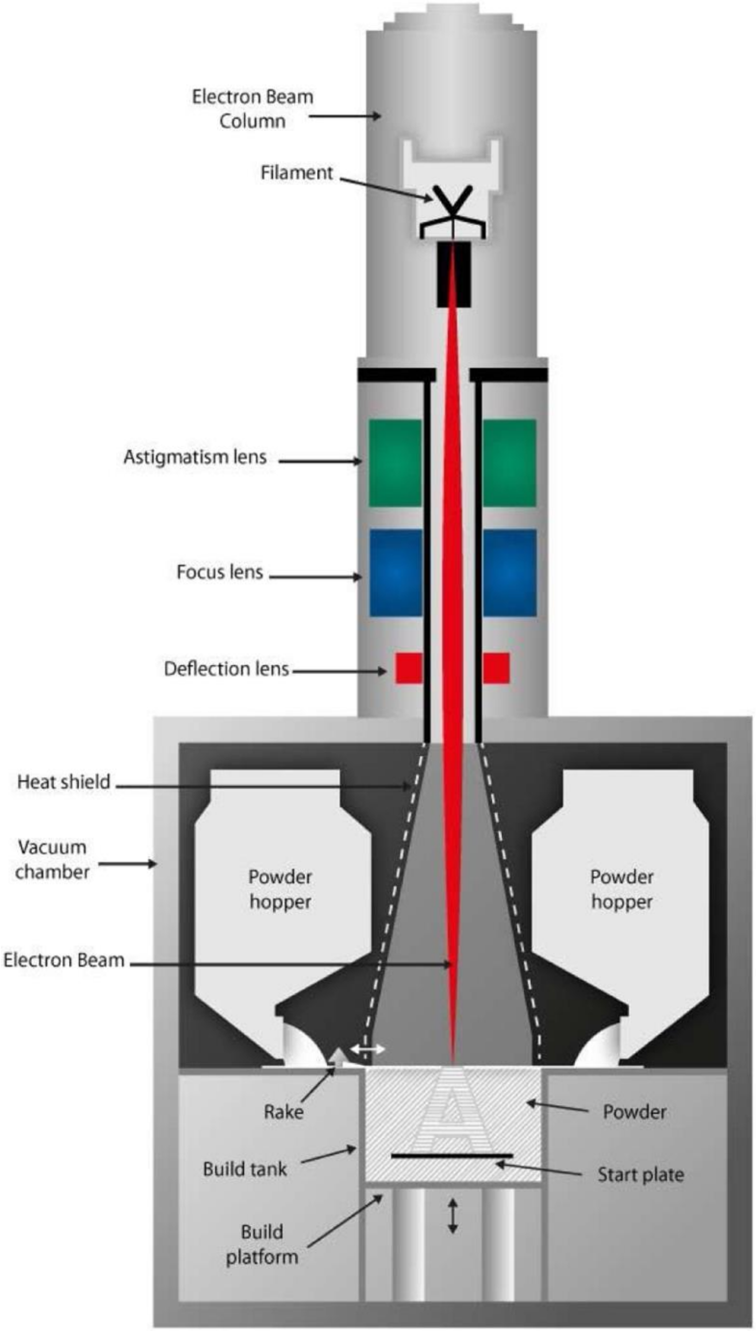

Fig. 1.8. Schematic overview of electron beam powder bed fusion (E-PBF) system [35].

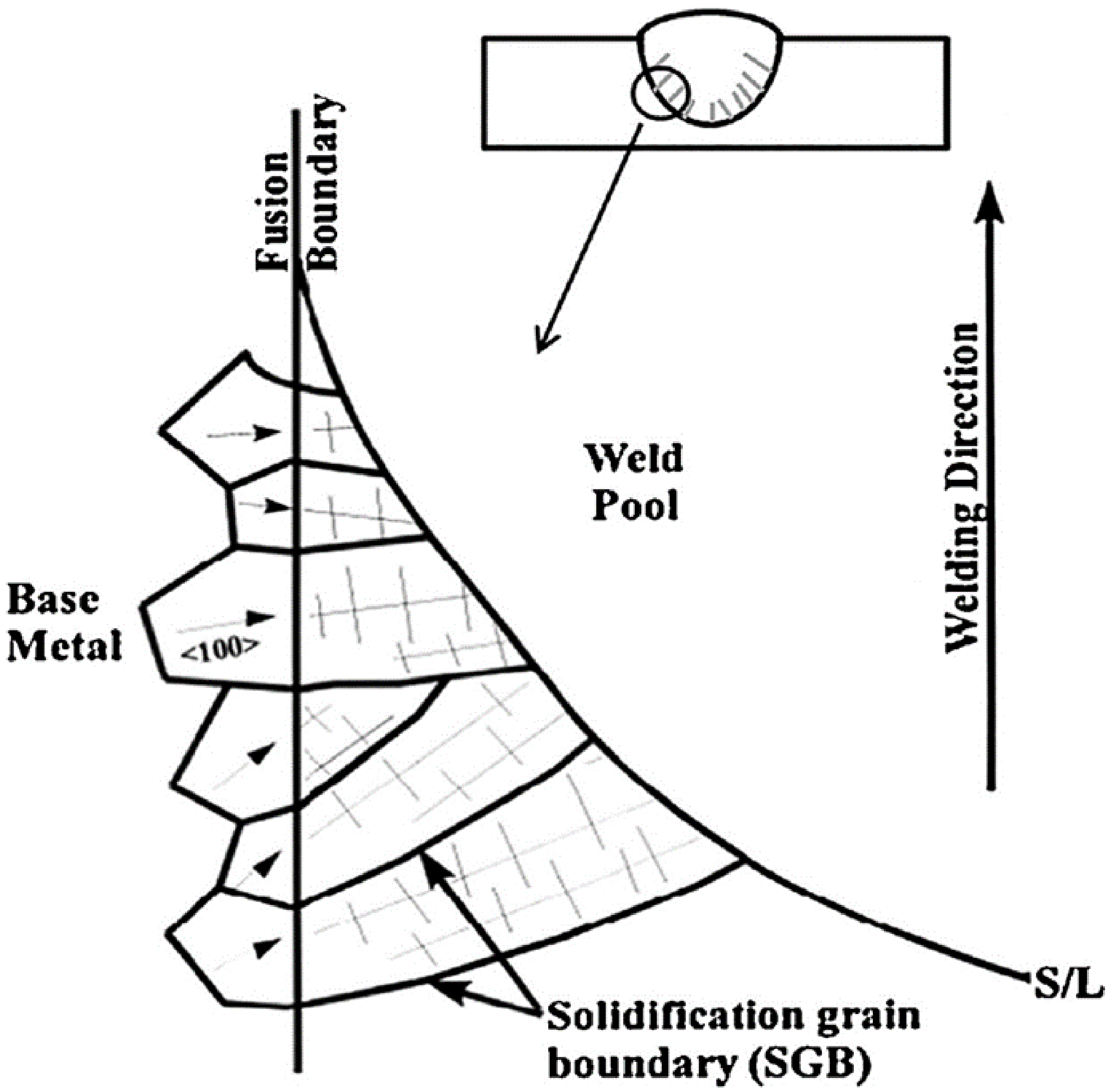

Fig. 1.9. Process of epitaxial solidification and competitive growth of grains within a welded molten zone [43].

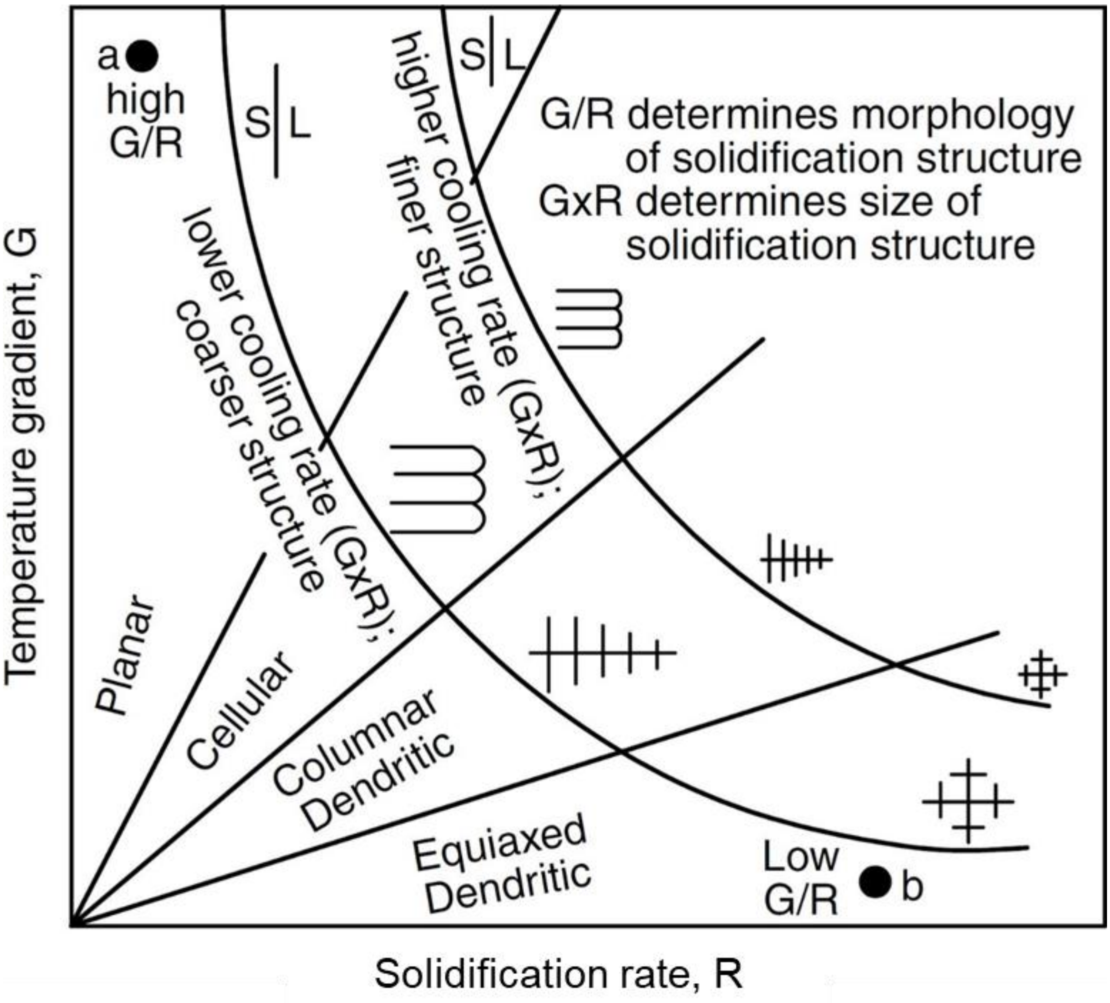

Fig. 1.10. Effect of temperature gradient G and solidification rate R on the morphology and size of solidification structure [42].

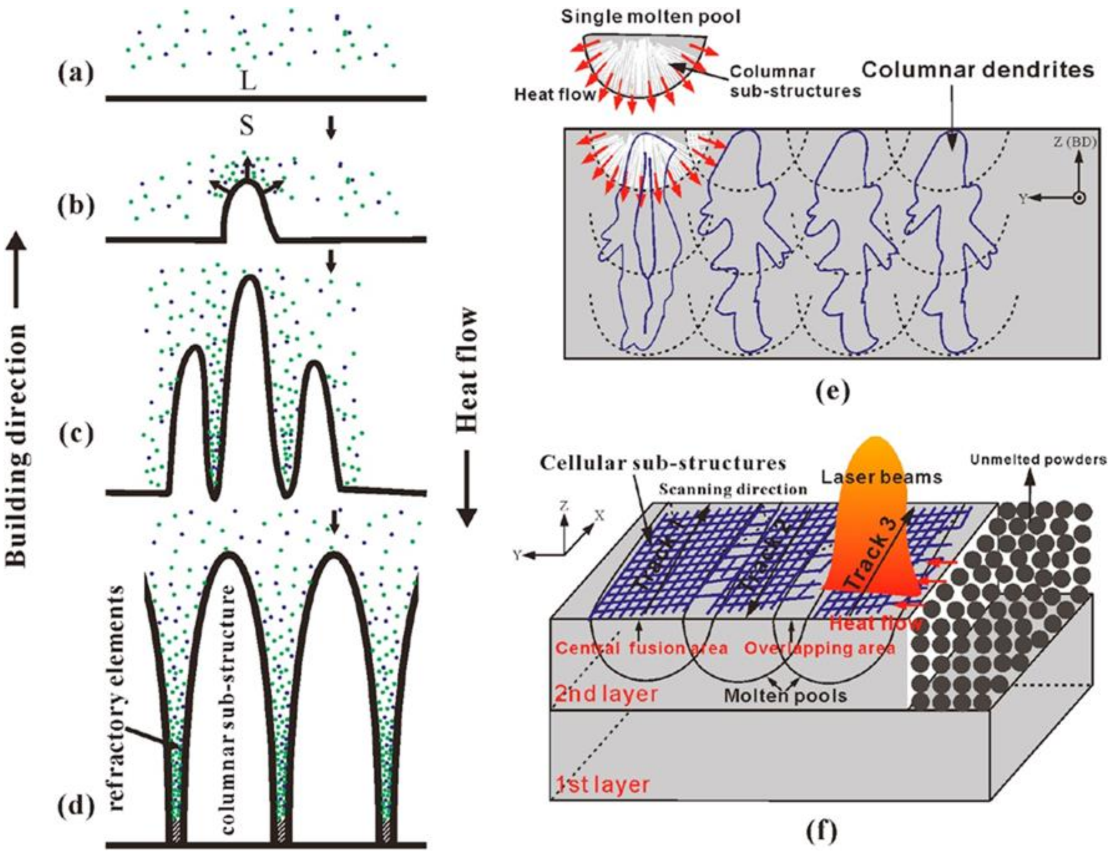

Fig. 1.11. Schematic illustration of micro-segregation of refractory alloying elements and the evolution of solidification sub-structures in AM microstructure [54].

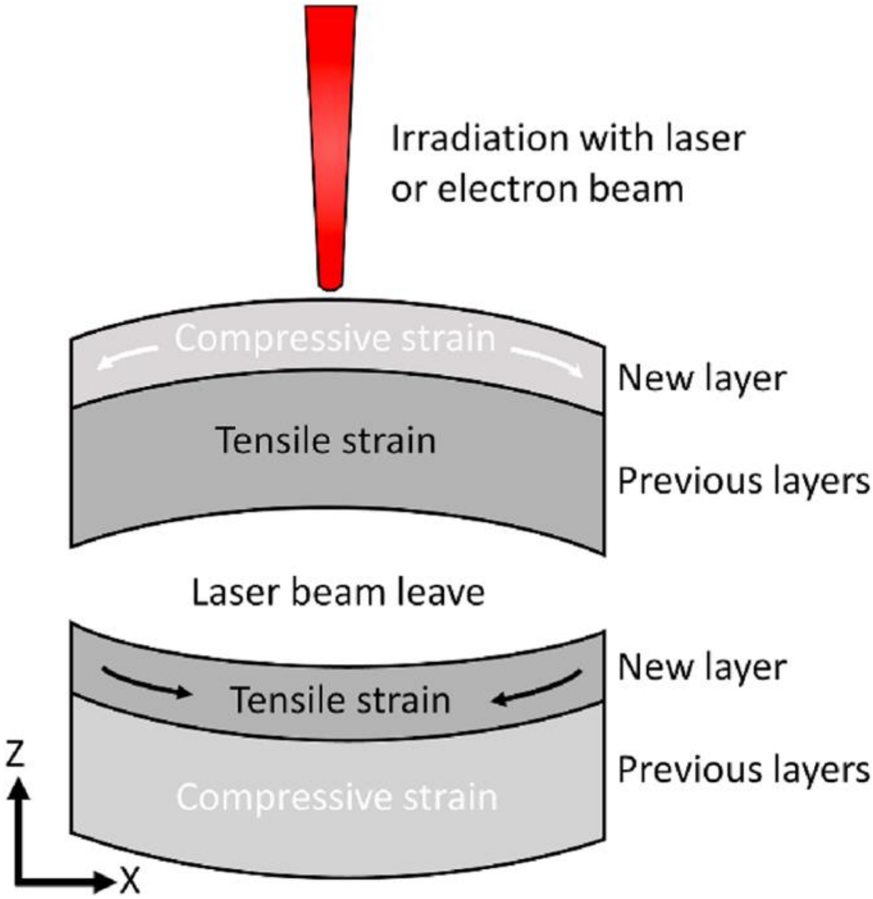

Fig. 1.12. Schematic illustration of the temperature-gradient mechanism for the development of residual stress during AM [55].

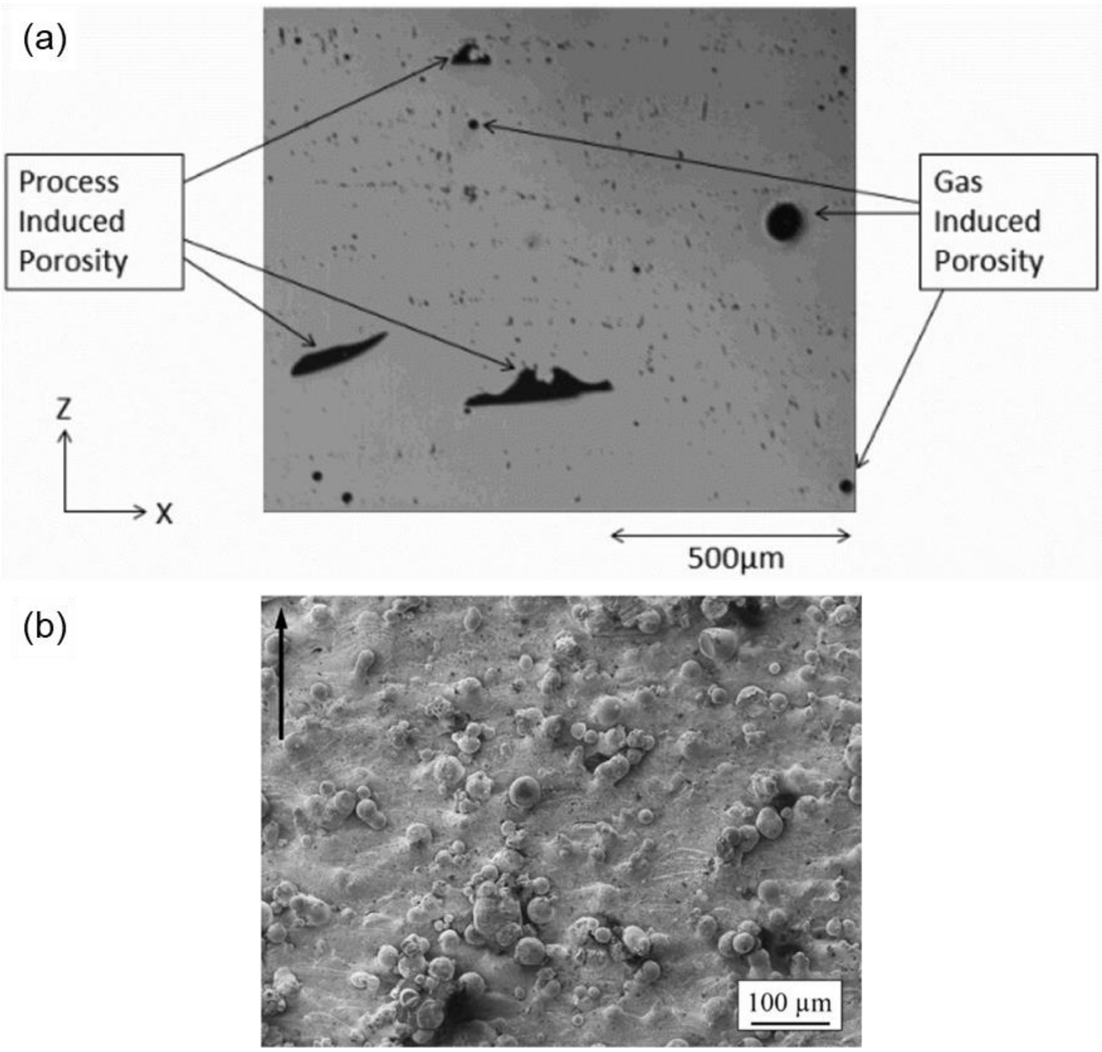

Fig. 1.13. Examples of defects introduced during AM process: (a) porosities including lack of fusion and gas pores [62]; (b) surface roughness with um-melted powders. Arrows in the images indicate the build direction [63].

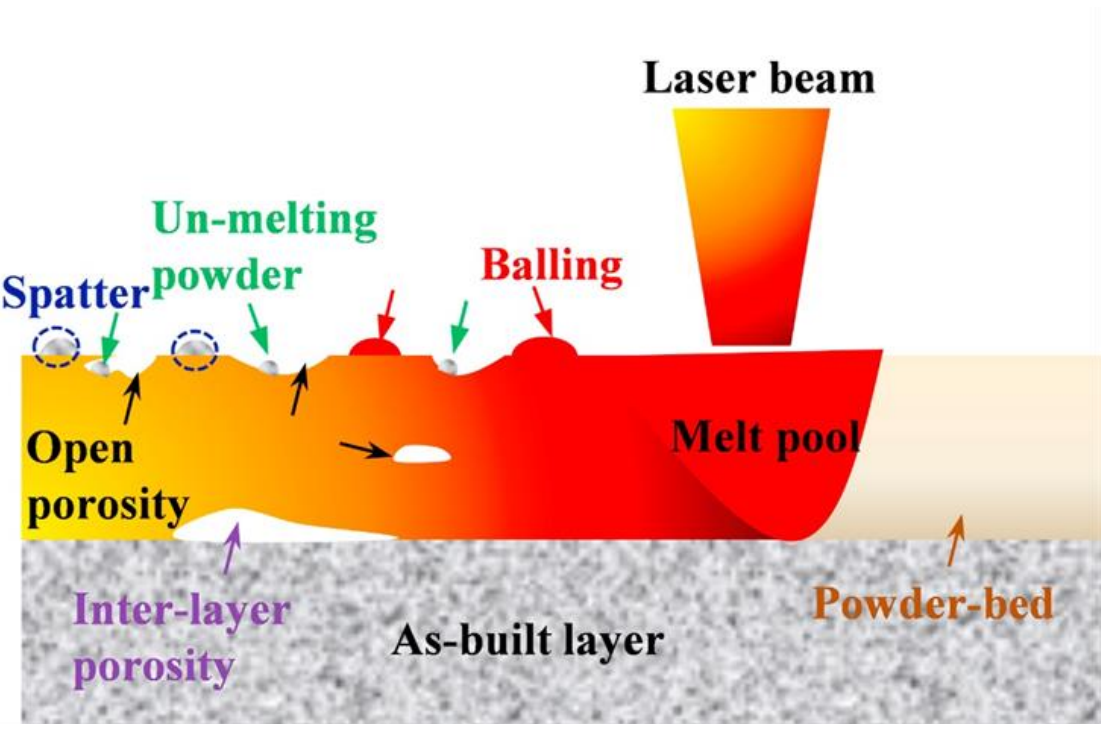

Fig. 1.14. Schematic illustration of the evolution of porosities and surface roughness during the AM process [61].

1.3 Literature review

Alloy 718 is frequently utilized in applications such as aerospace where components are subjected to numerous loading cycles during operation [69]. Hence, the high-cycle fatigue (HCF) properties of the alloy are of utmost importance in maintaining the structural integrity and safety of critical systems. However, the innate characteristics induced by the AM process such as crystallographic texture, micro-segregation, residual stresses and defects might add complexity to the evaluation of fatigue strength of AM Alloy 718. To ensure the reliable design for AM components, it is crucial to thoroughly understand the influence of each factor in a comprehensive manner.

While all of the AM features are mutually correlated each other, particular attention should be given to the process-induced defects such as lack of fusion, pores, and surface roughness [70], all of which are known to manifestly deteriorate the fatigue properties of AM parts when compared to their WR counterparts [71,72]. The influence of surface roughness is particularly pronounced for specimens in the as-built condition [73]. Previous research conducted by Kelley *et al*. [74] has demonstrated that AM Alloy 718 specimens with a machined surface exhibit significantly longer fatigue life compared to those with an as-built surface condition. In fact, the difference in lifetimes was found to be between 100 and 1000 times. Moreover, Witkin *et al*. [75] revealed that machined AM Alloy 718 specimens showed the fatigue strength similar to that of WR specimens while testing with as-built surfaces led to a decrease in fatigue life. The presence of porosities near the surface also subsequently degrades the fatigue performance of AM Alloy 718, as supported by the studies of Balachandramurthi *et al*. [63] and Pei *et al*. [76].

The hot isostatic pressing (HIP) technique is commonly employed to address surface defects near the sub-surface and internal defects [77]. Indeed, it has been observed that HIP-processed AM Alloy 718 specimens with the machined surface exhibit fatigue properties equivalent to those of WR Alloy 718 [74,75]. However, it is important to note that HIP is not effective in eliminating surface defects such as surface roughness and open pores on the surface and, therefore, its influence on the fatigue strength of specimens without surface machining is marginal [77]. Furthermore, considering that one of the major advantages of the AM process is its capability to produce complex geometries with internal features, post surface finishing may not be feasible [78]. Therefore, from a practical perspective of fatigue design, it is essential to quantify the effects of the process-induced defects on the fatigue strength.

Despite the abundant publications to date, there is still a relative scarcity of papers that specifically concentrate on the quantitative evaluation of the effect of the defects. A fracture mechanics-based, $\sqrt{area}$ parameter model, proposed by Murakami and Endo [79], has been broadly used for the quantitative evaluation of fatigue strength of materials containing small defects as a small-crack problem. Recently, some research groups have attempted to apply the model to the fatigue limit evaluation of Alloy 718. To validate the applicability of the $\sqrt{area}$ parameter model, Kevinsanny *et al.* [80] performed fully-reversed, uniaxial fatigue tests using WR Alloy 718 with different grain sizes and a variety of artificial small defects. As a result, they confirmed that in a small-crack regime, the predicted fatigue limits were in good agreement with the experimental results. Yamashita *et al.* [81] also assessed the fatigue limit of AM Alloy 718 *via* a small, Mode I, fatigue crack-growth threshold. They reported that in the evaluation based on the opening-mode threshold, the fatigue limit of the AM alloy had been overestimated by more than 10%. On the other hand, Okazaki *et al.* [82] observed an arrested crack lying along the maximum shear-stress plane at the bottom of a circumferential notch during the tension-compression fatigue test of WR Alloy 718. In their experiment, the criterion based on the opening-mode threshold provided a far from conservative prediction of the fatigue limit. Moreover, in a study by Tanaka *et al.* [83], push-pull and torsional fatigue tests of the WR Alloy 718 revealed that the fatigue limit was determined as the non-propagating condition of a small, shear-mode fatigue crack. In spite of the numerous studies to have been conducted on the fatigue limit of Alloy 718, the mechanism determining the fatigue limit has remained obscure; a lack of systematic experimentation has precluded the establishment of a universal method for the fatigue strength assessment of AM Alloy 718. Moreover, the fatigue threshold and small-crack behavior in this AM alloy have yet to be investigated in detail.

On the other hand, several researchers have investigated the relationship between microstructural factors other than defects and fatigue performance of AM Alloy 718. For example, Nishikawa *et al*. [84] observed small fatigue crack initiation and growth behavior in Alloy 718 specimens fabricated by rolling and AM. The findings indicated that the fatigue lives of the AM specimens with a strong [001] texture were shorter compared to the rolled plate specimens. It was suggested that a strong texture tends to generate low-angle grain boundaries (LAGBs) due to the close alignment of grains with a specific orientation and that the presence of a large fraction of LAGBs accelerated the shear mode, fatigue crack-growth rate at an early stage of propagation, ultimately resulting in a decrease in fatigue life. The similar results were acquired from the study of Ghorbanpour *et al*. [85] in which the values of fatigue crack-growth threshold of L-PBF samples were dependent on the fraction of the LAGBs. In addition, Konečná *et al*. [86] performed fatigue crack growth (FCG) tests with as-built AM Alloy 718 specimens and revealed that the threshold value of the AM alloy was significantly lower than that of WR alloy, which was potentially attributed to residual stress. However, there is a lack of evidence regarding the relationship between residual stress and small fatigue crack behavior in the HCF regime because Ni-based superalloys are typically subjected to post heat treatment for precipitate hardening after printing. Meanwhile, the role of Laves and δ phases, resulting from the micro-segregation of Nb in AM Alloy 718, has been a topic of debate. Gribben *et al*. [87] argued that the presence of δ phase caused a depletion of γ'' phases, which weakened the HCF strength of AM Alloy 718 at room temperature. Similarly, in a study by Sivaprasad and Raman [88], a large amount of Laves and δ phases resulted in inferior fatigue resistance in Alloy 718 tungsten inert gas (TIG) weldments. On the contrary, Sui *et al*. [89] reported that the HCF strength of AM Alloy 718 was comparable to that of WR alloy. The researchers observed that the growth of secondary cracks near the main crack path was hindered by the presence of unbroken particles of Laves and δ phases. Based on this observation, they suggested that the presence of Laves and δ phases may have contributed to the HCF strength of AM Alloy 718. Nonetheless, systematic investigations regarding the correlation between microstructural features and fatigue performance of AM Alloy 718, especially in relation to small fatigue-crack behavior near the threshold regime, are still limited. Furthermore, the synergistic effect of multiple factors in AM microstructures might render it more difficult to evaluate the individual effect of each factor, thus leaving a research space that remains unexplored.

1.4 Objective and outline of the thesis

This study aims to evaluate the fatigue limit of additively-manufactured Ni-based superalloy 718, with a significant emphasis on the influence of small defects and microstructural features in AM materials. Considering that the remarkable impact of small defects has been well documented in numerous literatures, the initial phase of this study is to quantify the influence of the defects on the fatigue limit from the perspective of a small crack problem. Subsequently, the study proceeds to systematically explore the impact of microstructural factors on the fatigue strength. To accomplish this goal, the study is structured into five chapters including the current introduction, and each chapter is outlined as follows:

In Chapter 2, fully-reversed, push-pull and torsional fatigue tests are performed using specimens with machined surfaces onto which an artificial defect is introduced or with machined surfaces having no artificial defects (*i.e.*, smooth condition). Based on the observation of small, fatigue crack-growth behavior at the fatigue limit, the determining condition of the fatigue limit is identified. Subsequently, shear-mode, fatigue crack-growth threshold in each test is estimated in order to quantitatively deal with the effects of small defects.

In Chapter 3, an AM sample with different microstructure is prepared to investigate the impacts of precipitates (*i.e.*, γ'', Laves and δ phases), grain size and residual stress on the fatigue threshold. Fatigue specimens possess different surface and defect conditions, *i.e.*, an as-built surface with rough surface and a machined surface with an artificial defect. In a similar fashion to the preceding chapter, push-pull fatigue tests are conducted, and the fatigue limit determining condition is examined. Finally, shear-mode fatigue threshold is comparably discussed with that of previous chapter.

In Chapter 4, the influence of crystallographic texture and annealing twin boundaries on fatigue resistance of the alloy is explored. A push-pull fatigue test using an WR specimen and a torsional fatigue test using an AM specimen are conducted to investigate the small-crack behaviors in both AM and WR materials at/near the fatigue limit. With the aids of electron microscopic techniques, the role of grain boundaries and annealing twin boundaries in crystallographic fatigue crack resistance is elucidated, based on geometric relationship between crack-planes of adjacent grains in the matrix or the twin.

In Chapter 5, the achievements in this study are summarized.

References

[1] Slama C, Abdellaoui M. Structural characterization of the aged Inconel 718. J Alloys Compd 2000;306:277–84. https://doi.org/10.1016/S0925-8388(00)00789-1.

[2] Qi H, Azer M, Ritter A. Studies of standard heat treatment effects on microstructure and mechanical properties of laser net shape manufactured INCONEL 718. Metall Mater Trans A Phys Metall Mater Sci 2009;40:2410–22. https://doi.org/10.1007/s11661-009-9949-3.

[3] Johnson AS, Shao S, Shamsaei N, Thompson SM, Bian L. Microstructure, Fatigue Behavior, and Failure Mechanisms of Direct Laser-Deposited Inconel 718. Jom 2017;69:597–603. https://doi.org/10.1007/s11837-016-2225-2.

[4] Davis JR and others. Nickel, cobalt, and their alloys. ASM international; 2000.

[5] Ding RG, Huang ZW, Li HY, Mitchell I, Baxter G, Bowen P. Electron microscopy study of direct laser deposited IN718. Mater Charact 2015;106:324–37. https://doi.org/10.1016/j.matchar.2015.06.017.

[6] Sundararaman M, Mukhopadhyay P, Banerjee S. Some aspects of the precipitation of metastable intermetallic phases in INCONEL 718. Metall Trans A 1992;23:2015–28. https://doi.org/10.1007/BF02647549.

[7] Oblak JM, Paulonis DF, Duvall DS. Coherency strengthening in Ni base alloys hardened by DO22 γ′ precipitates. Metall Trans 1974;5:143–53. https://doi.org/10.1007/BF02642938.

[8] Cao GH, Sun TY, Wang CH, Li X, Liu M, Zhang ZX, et al. Investigations of γ′ γ″ and δ precipitates in heat-treated Inconel 718 alloy fabricated by selective laser melting. Mater Charact 2018;136:398–406. https://doi.org/10.1016/j.matchar.2018.01.006.

[9] Gong X, Xu WW, Cui C, Yu Q, Wang W, Gang T, et al. Exploring alloying effect on phase stability and mechanical properties ofγ″-Ni3Nb precipitates with first-principles calculations. Mater Des 2020;196:109174. https://doi.org/10.1016/j.matdes.2020.109174.

[10] Azadian S, Wei LY, Warren R. Delta phase precipitation in inconel 718. Mater Charact 2004;53:7–16. https://doi.org/10.1016/j.matchar.2004.07.004.

[11] Lacaze J, Dehmas M, Niang A, Viguier B. TEM study of high-temperature precipitation of delta phase in inconel 718 alloy. Adv Mater Sci Eng 2011;2011. https://doi.org/10.1155/2011/940634.

[12] Chen MS, Zou ZH, Lin YC, Li H Bin, Wang GQ, Ma YY. Microstructural evolution and grain refinement mechanisms of a Ni-based superalloy during a two-stage annealing treatment. Mater Charact 2019;151:445–56. https://doi.org/10.1016/j.matchar.2019.03.037.

[13] Kuo YL, Horikawa S, Kakehi K. The effect of interdendritic δ phase on the mechanical properties of Alloy 718 built up by additive manufacturing. Mater Des 2017;116:411–8. https://doi.org/10.1016/j.matdes.2016.12.026.

[14] Kevinsanny. Effect of defects and hydrogen on the fatigue limit properties of forged and additive manufactured Ni-based superalloy 718. Master Thesis, Kyushu University, 2019.

[15] Smith TM, Gabb TP, Kantzos CA, Thompson AC, Sudbrack CK, West B, et al. The effect of composition on microstructure and properties for additively manufactured superalloy 718. J Alloys Compd 2021;873:159789. https://doi.org/10.1016/j.jallcom.2021.159789.

[16] Soller S, Barata A, Beyer S, Dahlhaus A, Guichard D, Humbert E, et al. Selective laser melting (SLM) of Inconel 718 and stainless steel injectors for liquid rocket engines. Proc. Sp. Propuls., 2016.

[17] Soller S, Behr R, Beyer S, Laithier F, Lehmann M, Preuss A, et al. Design and Testing of Liquid Propellant Injectors for Additive Manufacturing. 7TH Eur. Conf. Aerosp. Sci. (EUCASS 2017), 2017.

[18] Reed RC. The superalloys: fundamentals and applications. Cambridge university press; 2008.

[19] Ezugwu EO, Bonney J, Yamane Y. An overview of the machinability of aeroengine alloys. J Mater Process Technol 2003;134:233–53. https://doi.org/10.1016/S0924-0136(02)01042-7.

[20] Ha D, Roh TS, Huh H, Lee HJ. Development Trend of Liquid Hydrogen-Fueled Rocket Engines (Part 1: Performance and Operation). Int J Aeronaut Sp Sci 2023;24:131–45. https://doi.org/10.1007/s42405-022-00519-7.

[21] Kawashima H, Funakoshi Y, Kurosu A, Kobayashi T, Okita K. Development status of le-9 engine for h3 launch vehicle. AIAA Propuls Energy Forum Expo 2019 2019:1–10. https://doi.org/10.2514/6.2019-4024.

[22] Nara T, Onga T, Niitsu M, Takida J, Sato A, Negoro N. Development Status of H3 Launch Vehicle-To compete and survive in the global commercial market-. Mitsubishi Heavy Ind Tech Rev 2017;54:32–9.

[23] Azuma N, Kojima M, Kobayashi T, Okita K, Motomura T, Niiyama K. The development status of le-9 engine turbopumps for h3 launch vehicle. AIAA Propuls Energy Forum Expo 2019 2019:1–9. https://doi.org/10.2514/6.2019-4430.

[24] Findlay SJ, Harrison ND. Why aircraft fail. Mater Today 2002;5:18–25. https://doi.org/10.1016/S1369-7021(02)01138-0.

[25] Sadeghi E, Karimi P, Esmaeilizadeh R, Berto F, Shao S, Moverare J, et al. A state-of-the-art review on fatigue performance of powder bed fusion-built alloy 718. Prog Mater Sci 2023;133. https://doi.org/10.1016/j.pmatsci.2022.101066.

[26] Bourell DL. Perspectives on Additive Manufacturing. Annu Rev Mater Res 2016;46:1–18. https://doi.org/10.1146/annurev-matsci-070115-031606.

[27] King WE, Anderson AT, Ferencz RM, Hodge NE, Kamath C, Khairallah SA, et al. Laser powder bed fusion additive manufacturing of metals; physics, computational, and materials challenges. Appl Phys Rev 2015;2:041304. https://doi.org/10.1063/1.4937809.

[28] Sola A, Nouri A. Microstructural porosity in additive manufacturing: The formation and detection of pores in metal parts fabricated by powder bed fusion. J Adv Manuf Process 2019;1:1–21. https://doi.org/10.1002/amp2.10021.

[29] Shi Q, Gu D, Xia M, Cao S, Rong T. Effects of laser processing parameters on thermal behavior and melting/solidification mechanism during selective laser melting of TiC/Inconel 718 composites. Opt Laser Technol 2016;84:9–22. https://doi.org/10.1016/j.optlastec.2016.04.009.

[30] Yap CY, Chua CK, Dong ZL, Liu ZH, Zhang DQ, Loh LE, et al. Review of selective laser melting: Materials and applications. Appl Phys Rev 2015;2. https://doi.org/10.1063/1.4935926.

[31] Yang H, Meng L, Luo S, Wang Z. Microstructural evolution and mechanical performances of selective laser melting Inconel 718 from low to high laser power. J Alloys Compd 2020;828:154473. https://doi.org/10.1016/j.jallcom.2020.154473.

[32] Jia Q, Gu D. Selective laser melting additive manufacturing of Inconel 718 superalloy parts: Densification, microstructure and properties. J Alloys Compd 2014;585:713–21. https://doi.org/10.1016/j.jallcom.2013.09.171.

[33] Gu DD, Meiners W, Wissenbach K, Poprawe R. Laser additive manufacturing of metallic components: Materials, processes and mechanisms. Int Mater Rev 2012;57:133–64. https://doi.org/10.1179/1743280411Y.0000000014.

[34] Li C, Guo YB, Zhao JB. Interfacial phenomena and characteristics between the deposited material and substrate in selective laser melting Inconel 625. J Mater Process Technol 2017;243:269–81. https://doi.org/10.1016/j.jmatprotec.2016.12.033.

[35] Chandrasekar S, Coble JB, Yoder S, Nandwana P, Dehoff RR, Paquit VC, et al. Investigating the effect of metal powder recycling in Electron beam Powder Bed Fusion using process log data. Addit Manuf 2020;32. https://doi.org/10.1016/j.addma.2019.100994.

[36] Meid C, Dennstedt A, Ramsperger M, Pistor J, Ruttert B, Lopez-Galilea I, et al. Effect of heat treatment on the high temperature fatigue life of single crystalline nickel base superalloy additively manufactured by means of selective electron beam melting. Scr Mater 2019;168:124–8. https://doi.org/10.1016/j.scriptamat.2019.05.002.

[37] Blakey-Milner B, Gradl P, Snedden G, Brooks M, Pitot J, Lopez E, et al. Metal additive manufacturing in aerospace: A review. Mater Des 2021;209:110008. https://doi.org/10.1016/j.matdes.2021.110008.

[38] DebRoy T, Wei HL, Zuback JS, Mukherjee T, Elmer JW, Milewski JO, et al. Additive manufacturing of metallic components – Process, structure and properties. Prog Mater Sci 2018;92:112–224. https://doi.org/10.1016/j.pmatsci.2017.10.001.

[39] DebRoy T, Wei HL, Zuback JS, Mukherjee T, Elmer JW, Milewski JO, et al. Additive manufacturing of metallic components – Process, structure and properties. Prog Mater Sci 2018;92:112–224. https://doi.org/10.1016/j.pmatsci.2017.10.001.

[40] Wang C, Zhang J, Liu L, Fu H. Effect of Melt Superheating Treatment on Directional Solidification Interface Morphology of Multi-component Alloy. J Mater Sci Technol 2011;27:668–72. https://doi.org/10.1016/S1005-0302(11)60123-0.

[41] Gäumann M, Henry S, Cléton F, Wagnière JD, Kurz W. Epitaxial laser metal forming: Analysis of microstructure formation. Mater Sci Eng A 1999;271:232–41. https://doi.org/10.1016/s0921-5093(99)00202-6.

[42] Kou S. Welding metallurgy. John Wiley \& Sons; 2020.

[43] Cam G, Mistikoglu S. Recent developments in friction stir welding of Al-alloys. J Mater Eng Perform 2014;23:1936–53.

[44] Zhang J, Song B, Wei Q, Bourell D, Shi Y. A review of selective laser melting of aluminum alloys: Processing, microstructure, property and developing trends. J Mater Sci Technol 2019;35:270–84. https://doi.org/10.1016/j.jmst.2018.09.004.

[45] Calandri M, Yin S, Aldwell B, Calignano F, Lupoi R, Ugues D. Texture and microstructural features at different length scales in Inconel 718 produced by selective laser melting. Materials (Basel) 2019;12. https://doi.org/10.3390/ma12081293.

[46] Lee JS, Gu JH, Jung HM, Kim EH, Jung YG, Lee JH. Directional solidification microstructure control in CM247LC superalloy. Mater Today Proc 2014;1:3–10. https://doi.org/10.1016/j.matpr.2014.09.002.

[47] Wei HL, Mazumder J, DebRoy T. Evolution of solidification texture during additive manufacturing. Sci Rep 2015;5:1–7. https://doi.org/10.1038/srep16446.

[48] Zhang Q, Xue H, Tang Q, Pan S, Rettenmayr M, Zhu M. Microstructural evolution during temperature gradient zone melting: Cellular automaton simulation and experiment. Comput Mater Sci 2018;146:204–12. https://doi.org/10.1016/j.commatsci.2018.01.032.

[49] Nie P, Ojo OA, Li Z. Numerical modeling of microstructure evolution during laser additive manufacturing of a nickel-based superalloy. Acta Mater

2014;77:85–95. https://doi.org/10.1016/j.actamat.2014.05.039.

[50] Liu F, Lin X, Leng H, Cao J, Liu Q, Huang C, et al. Microstructural changes in a laser solid forming Inconel 718 superalloy thin wall in the deposition direction. Opt Laser Technol 2013;45:330–5. https://doi.org/10.1016/j.optlastec.2012.06.028.

[51] Tian Y, McAllister D, Colijn H, Mills M, Farson D, Nordin M, et al. Rationalization of microstructure heterogeneity in INCONEL 718 builds made by the direct laser additive manufacturing process. Metall Mater Trans A Phys Metall Mater Sci 2014;45:4470–83. https://doi.org/10.1007/s11661-014-2370-6.

[52] Janaki Ram GD, Venugopal Reddy A, Prasad Rao K, Madhusudhan Reddy G. Control of Laves phase in Inconel 718 GTA welds with current pulsing. Sci Technol Weld Join 2004;9:390–8.

[53] Schirra JJ, Caless RH, Hatala RW. The Effect of Laves Phase on the Mechanical Properties of Wrought and Cast + HIP Inconel 718 2012:375–88. https://doi.org/10.7449/1991/superalloys_1991_375_388.

[54] Li X, Shi JJ, Wang CH, Cao GH, Russell AM, Zhou ZJ, et al. Effect of heat treatment on microstructure evolution of Inconel 718 alloy fabricated by selective laser melting. J Alloys Compd 2018;764:639–49. https://doi.org/10.1016/j.jallcom.2018.06.112.

[55] Guo C, Li G, Li S, Hu X, Lu H, Li X, et al. Additive manufacturing of Ni-based superalloys: Residual stress, mechanisms of crack formation and strategies for crack inhibition. Nano Mater Sci 2022. https://doi.org/10.1016/j.nanoms.2022.08.001.

[56] Mercelis P, Kruth J-P. Residual stresses in selective laser sintering and selective laser melting. Rapid Prototyp J 2006;12:254–65. https://doi.org/10.1108/13552540610707013.

[57] Bartlett JL, Li X. An overview of residual stresses in metal powder bed fusion. Addit Manuf 2019;27:131–49. https://doi.org/10.1016/j.addma.2019.02.020.

[58] Li C, Fu CH, Guo YB, Fang FZ. A multiscale modeling approach for fast prediction of part distortion in selective laser melting. J Mater Process Technol 2015;229:703–12. https://doi.org/10.1016/j.jmatprotec.2015.10.022.

[59] Hussein A, Hao L, Yan C, Everson R. Finite element simulation of the temperature and stress fields in single layers built without-support in selective laser melting. Mater Des 2013;52:638–47. https://doi.org/10.1016/j.matdes.2013.05.070.

[60] Wang X, Chou K. The effects of stress relieving heat treatment on the microstructure and residual stress of Inconel 718 fabricated by laser metal powder bed fusion additive manufacturing process. J Manuf Process 2019;48:154–63. https://doi.org/10.1016/j.jmapro.2019.10.027.

[61] Xia M, Gu D, Yu G, Dai D, Chen H, Shi Q. Porosity evolution and its thermodynamic mechanism of randomly packed powder-bed during selective laser melting of Inconel 718 alloy. Int J Mach Tools Manuf 2017;116:96–106. https://doi.org/10.1016/j.ijmachtools.2017.01.005.

[62] Sames WJ, List FA, Pannala S, Dehoff RR, Babu SS. The metallurgy and processing science of metal additive manufacturing. Int Mater Rev 2016;61:315–60. https://doi.org/10.1080/09506608.2015.1116649.

[63] Balachandramurthi AR, Moverare J, Dixit N, Pederson R. Influence of defects and as-built surface roughness on fatigue properties of additively manufactured Alloy 718. Mater Sci Eng A 2018;735:463–74. https://doi.org/10.1016/j.msea.2018.08.072.

[64] Xiao R, Zhang X. Problems and issues in laser beam welding of aluminum-lithium alloys. J Manuf Process 2014;16:166–75. https://doi.org/10.1016/j.jmapro.2013.10.005.

[65] Olakanmi EO, Cochrane RF, Dalgarno KW. Densification mechanism and microstructural evolution in selective laser sintering of Al-12Si powders. J Mater Process Technol 2011;211:113–21. https://doi.org/10.1016/j.jmatprotec.2010.09.003.

[66] Kruth JP, Froyen L, Van Vaerenbergh J, Mercelis P, Rombouts M, Lauwers B. Selective laser melting of iron-based powder. J Mater Process Technol 2004;149:616–22. https://doi.org/10.1016/j.jmatprotec.2003.11.051.

[67] Zerbst U, Madia M, Bruno G, Hilgenberg K. Towards a methodology for component design of metallic am parts subjected to cyclic loading. Metals (Basel) 2021;11:1–17. https://doi.org/10.3390/met11050709.

[68] Shi Q, Gu D, Xia M, Cao S, Rong T. Effects of laser processing parameters on thermal behavior and melting/solidification mechanism during selective laser melting of TiC/Inconel 718 composites. Opt Laser Technol 2016;84:9–22. https://doi.org/10.1016/j.optlastec.2016.04.009.

[69] Muhammad M, Frye P, Simsiriwong J, Shao S, Shamsaei N. An investigation into the effects of cyclic strain rate on the high cycle and very high cycle fatigue behaviors of wrought and additively manufactured Inconel 718. Int J Fatigue 2021;144:106038. https://doi.org/10.1016/j.ijfatigue.2020.106038.

[70] Murakami Y. Metal fatigue: effects of small defects and nonmetallic inclusions. Academic Press; 2019.

[71] Pegues J, Roach M, Scott Williamson R, Shamsaei N. Surface roughness effects on the fatigue strength of additively manufactured Ti-6Al-4V. Int J Fatigue 2018;116:543–52. https://doi.org/10.1016/j.ijfatigue.2018.07.013.

[72] Gorelik M. Additive manufacturing in the context of structural integrity. Int J Fatigue 2017;94:168–77. https://doi.org/10.1016/j.ijfatigue.2016.07.005.

[73] Sanaei N, Fatemi A. Defects in additive manufactured metals and their effect on fatigue performance: A state-of-the-art review. Prog Mater Sci 2021;117:100724. https://doi.org/10.1016/j.pmatsci.2020.100724.

[74] Carter A, Saigal A, Kelley PF. Fatigue behaviour of direct metal laser sintered Inconel 718. Int J Precis Technol 2016;6:277. https://doi.org/10.1504/ijptech.2016.10000853.

[75] Witkin DB, Patel DN, Bean GE. Notched fatigue testing of Inconel 718 prepared by selective laser melting. Fatigue Fract Eng Mater Struct 2019;42:166–77. https://doi.org/10.1111/ffe.12880.

[76] Pei C, Shi D, Yuan H, Li H. Assessment of mechanical properties and fatigue performance of a selective laser melted nickel-base superalloy Inconel 718. Mater Sci Eng A 2019;759:278–87. https://doi.org/10.1016/j.msea.2019.05.007.

[77] Masuo H, Tanaka Y, Morokoshi S, Yagura H, Uchida T, Yamamoto Y, et al. Influence of defects, surface roughness and HIP on the fatigue strength of Ti-6Al-4V manufactured by additive manufacturing. Int J Fatigue 2018;117:163–79. https://doi.org/10.1016/j.ijfatigue.2018.07.020.

[78] Hosseini E, Popovich VA. A review of mechanical properties of additively manufactured Inconel 718. Addit Manuf 2019;30:100877. https://doi.org/10.1016/j.addma.2019.100877.

[79] Murakami Y, Endo M. Effects of defects, inclusions and inhomogeneities on fatigue strength. Int J Fatigue 1994;16:163–82. https://doi.org/10.1016/0142-1123(94)90001-9.

[80] Kevinsanny, Okazaki S, Takakuwa O, Ogawa Y, Okita K, Funakoshi Y, et al. Effect of defects on the fatigue limit of Ni-based superalloy 718 with different grain sizes. Fatigue Fract Eng Mater Struct 2019;42:1203–13. https://doi.org/10.1111/ffe.12989.

[81] Yamashita Y, Murakami T, Mihara R, Okada M, Murakami Y. Defect analysis and fatigue design basis for Ni-based superalloy 718 manufactured by selective laser melting. Int J Fatigue 2018;117:485–95. https://doi.org/10.1016/j.ijfatigue.2018.08.002.

[82] Okazaki S, Okuma S, Kevinsanny, Ogawa Y, Kawashima H, Funakoshi Y, et al. Unforeseen, negative interaction-effect of adjacent circumferential notches on the fatigue limit of Ni-based superalloy 718. Eng Fract Mech 2021;257:108015. https://doi.org/10.1016/j.engfracmech.2021.108015.

[83] Tanaka Y, Okazaki S, Ogawa Y, Endo M, Matsunaga H. Fatigue limit of Ni-based superalloy 718 relative to the shear-mode crack-growth threshold: A quantitative evaluation considering the influence of crack-opening and -closing stresses. Int J Fatigue 2021;148:106228. https://doi.org/10.1016/j.ijfatigue.2021.106228.

[84] Nishikawa H, Furuya Y, Kitano H, Nakamura T, Kuwabara K, Kanegae Y, et al. In-situ observation of microstructurally small fatigue crack initiation and growth behaviors of additively-manufactured alloy 718. Mater Sci Eng A 2022;835:142682. https://doi.org/10.1016/j.msea.2022.142682.

[85] Ghorbanpour S, Sahu S, Deshmukh K, Borisov E, Riemslag T, Reinton E, et al. Effect of microstructure induced anisotropy on fatigue behaviour of functionally graded Inconel 718 fabricated by additive manufacturing. Mater Charact 2021;179:111350. https://doi.org/10.1016/j.matchar.2021.111350.

[86] Konečná R, Kunz L, Nicoletto G, Bača A. Long fatigue crack growth in Inconel 718 produced by selective laser melting. Int J Fatigue 2016;92:499–506. https://doi.org/10.1016/j.ijfatigue.2016.03.012.

[87] Gribbin S, Ghorbanpour S, Ferreri NC, Bicknell J, Tsukrov I, Knezevic M. Role of grain structure, grain boundaries, crystallographic texture, precipitates, and porosity on fatigue behavior of Inconel 718 at room and elevated temperatures. Mater Charact 2019;149:184–97. https://doi.org/10.1016/j.matchar.2019.01.028.

[88] Sivaprasad K, Raman SGS. Influence of magnetic arc oscillation and current pulsing on fatigue behavior of alloy 718 TIG weldments. Mater Sci Eng A 2007;448:120–7. https://doi.org/10.1016/j.msea.2006.10.048.

[89] Sui S, Chen J, Fan E, Yang H, Lin X, Huang W. The influence of Laves phases on the high-cycle fatigue behavior of laser additive manufactured Inconel 718. Mater Sci Eng A 2017;695:6–13. https://doi.org/10.1016/j.msea.2017.03.098.

2. Quantitative evaluation of the effect of defects on the fatigue limit of AM Alloy 718 *via* shear-mode threshold

2.1 Introduction

The fatigue crack-growth threshold, ΔK_{th}, also known as the fatigue threshold, is a critical parameter in fatigue analysis such as fatigue limit evaluation of materials containing defects. It corresponds to the lower bound of stress intensity factor (SIF) range below which the crack-growth rate is extremely low or negligible [1]. It is well known that the threshold for "large crack" with an order of a few millimeters in common structural steels is independent of crack size under a constant stress ratio [2]. However, it should be noted that threshold for "small crack" becomes smaller than that for large crack and is decreased with a decrease in crack size (*i.e.*, the crack-size dependence of ΔK_{th}). This unique phenomenon for small cracks is closely related to the significant difference in the mechanical severity (*e.g.*, stress and strain distributions) near the crack tip between large crack and small crack even under a same stress intensity [3]. In the long history of the research on metal fatigue, the growth and threshold behaviors of the latter have been dealt with as "small crack problem" [4], and there have been considerable efforts to develop methods for predicting the ΔK_{th} values of materials with small defects [5].

With the above situation as background, Murakami and Endo [6] proposed a simple and useful method to predict the threshold SIF range for Mode I fatigue cracks, ΔK_{Ith}, and accordingly the fatigue limit, which is called $\sqrt{area}$ parameter model. It is based on the experimental findings as follows: i) fatigue limit is the threshold condition for non-propagation of cracks emanating from defects, ii) the cracks propagate in a direction almost perpendicular to the direction of the principal stress (*i.e.*, Mode I cracks) at the fatigue limit. According to this model, the crack-size dependence of ΔK_{Ith} of various ferrous alloys in small crack regime can be formulated as follows (*cf.* Fig. 2.1) [5]:

$$\Delta K_{Ith} = 3.3\times10^{-3}(HV + 120)(\sqrt{area})^{1/3} \tag{2.1}$$

where *area* is defined as the area of a small defect or crack projected onto a plane perpendicular to the principal stress, as illustrated in Fig. 2.2. In the small-crack regime, the fatigue limit of materials containing surface defects at a stress ratio of −1 can be predicted using the formula as follows:

$$\sigma_w = 1.43(HV + 120)/(\sqrt{area})^{1/6} \tag{2.2}$$

Over the years, numerous studies have extensively demonstrated the applicability of this model, covering a wide range of materials [7–9].

However, the comprehensive evaluation method of fatigue limit still lacks clarity with regard to Alloy 718. First of all, the determining condition of the fatigue limit, *i.e.*, whether it is governed by the threshold condition of Mode I cracks (ΔK_{Ith}) or shear-mode cracks ($\Delta K_{\tau\mathrm{th}}$), remains a subject of debate. Although Kevinsanny *et al.* [10] suggested the $\sqrt{area}$ parameter model is applicable to WR Alloy 718 (*cf.* Fig. 2.3), Okazaki *et al.* [11] observed an arrested crack lying along the maximum shear-stress plane at the bottom of a circumferential notch during the tension-compression fatigue test of WR Alloy 718. In their experiment, the criterion based on the opening-mode threshold provided an overestimated prediction of the fatigue limit. Moreover, Tanaka *et al.* [12] recently conducted fatigue tests using two WR Alloy 718 samples under different loading conditions (*i.e.*, tension-compression, pure-torsion and torsion with superposed static tension). They demonstrated that the fatigue limit of all WR samples was dominated by the non-propagation of small, shear-mode fatigue cracks, *i.e.*, $\Delta K_{\tau\mathrm{th}}$, irrespective of loading conditions, exhibiting a crack-size dependence similar to that of ΔK_{Ith}. The similar results were obtained in the push-pull fatigue tests of a coarse-grained WR alloy (WR-CG) in which some non-propagating cracks along the maximum shear-stress direction were also observed [13]. Notwithstanding the efforts of several researchers to date, since the reported results vary substantially amongst researchers and there is a lack of observation on the crack-arresting mode, a thorough understanding of the determining condition of the fatigue limit of the alloy remains elusive and incomplete, hindering the establishment of fatigue limit prediction model for AM Alloy 718.

In addition, AM material has a significantly different microstructure compared to WR material, as addressed in the previous chapter. This could lead to a disparity in fatigue thresholds between AM and WR materials. Indeed, Yamashita *et al.* [14] have assessed the fatigue limit of two AM Alloy 718 materials with different microstructures in terms of the opening-mode threshold. The results revealed that estimated values of ΔK_{Ith} for all AM alloys were apparently lower than those of WR alloys [10] (*cf*. Fig. 2.3 and Fig. 2.4). While the validity of the ΔK_{Ith}-based evaluation for AM materials is still uncertain, the aforementioned experimental results imply that AM alloys may exhibit poor fatigue resistance compared to WR alloys. This difference in fatigue resistance can be attributed to various microstructural factors of AM materials. It is noteworthy that the quantification of the effect of defects *via* fatigue threshold is a prerequisite for gaining a comprehensive understanding of the influence of other factors on fatigue resistance, which ultimately provides insights for improving the fatigue performance of AM materials. Nevertheless, a systematic investigation of the small, fatigue crack-growth threshold of AM Alloy 718 has not yet been conducted.

In this context, the initial objective in this chapter is to elucidate the determining condition of the fatigue limit in the AM alloy based on analyses on the crack-arresting mode at or near the fatigue limit. Following this, an attempt will be made to assess the fatigue-crack growth-threshold in order to quantify the effect of defects on fatigue limit of AM Alloy 718. Finally, the chapter will compare and discuss the results of the fatigue threshold estimation for AM alloy with those of WR alloys.

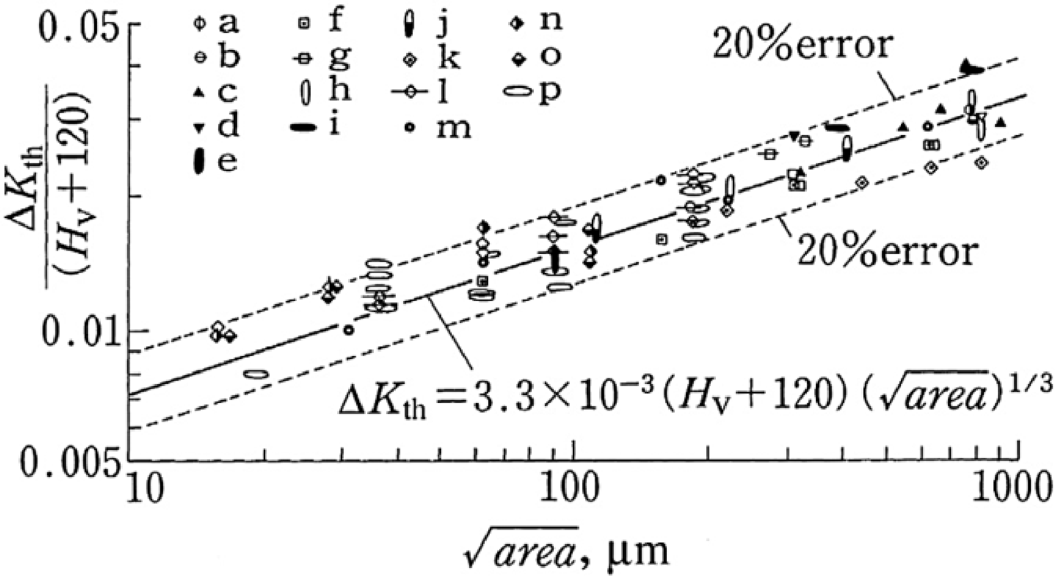

Materials	Defects
a: 0.12%C steel	Fatigue crack
b: 0.53%C steel	Fatigue crack
c: SF60	Artificial crack, Hole
d: Mild steel	Fatigue crack
e: S10C	Drilled hole
f: S20C	Circumferential notch
g: S20C	Drilled hole
h: S25C	Fatigue crack
i: S35C	Fatigue crack
j: S45C	Fatigue crack
k: Eutectic steel	Circumferential crack
l: Eutectic steel	Drilled hole
m: 2.25Cr/ 1Mo steel	Circumferential crack
n: SAE 1552 steel	Electro discharged hole
o: SAE 9254 steel	Electro discharged hole
p: Maraging steel	Hole, Notch, Vickers indentation

Fig. 2.1. Crack size dependence of the threshold SIF range for Mode I fatigue cracks, ΔK_{Ith}, of various ferrous alloys in small crack regime [5].

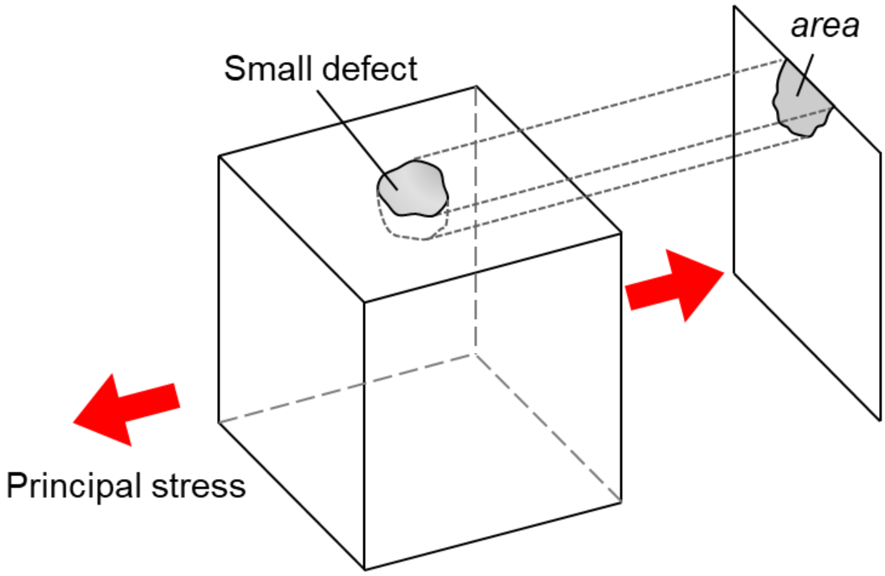

Fig. 2.2. Definition of the projected area of small defect onto the principal stress plane, *area*.

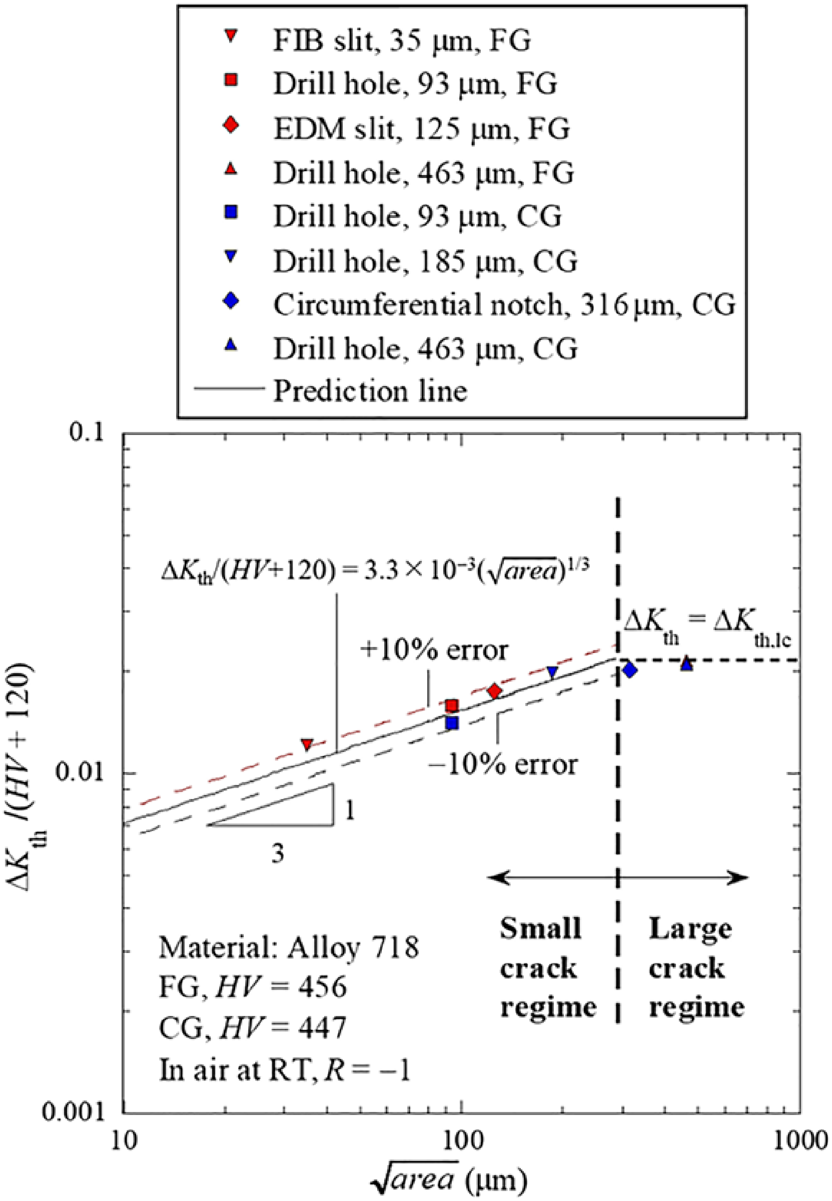

Fig. 2.3. Relationship between the threshold SIF range for Mode I fatigue cracks, ΔK_{Ith}, and the defect size, $\sqrt{area}$, in WR Alloy 718. CG stands for coarse-grained, EDM for electron discharge machining, FG for fine-grained, and FIB for focused ion beam [10].

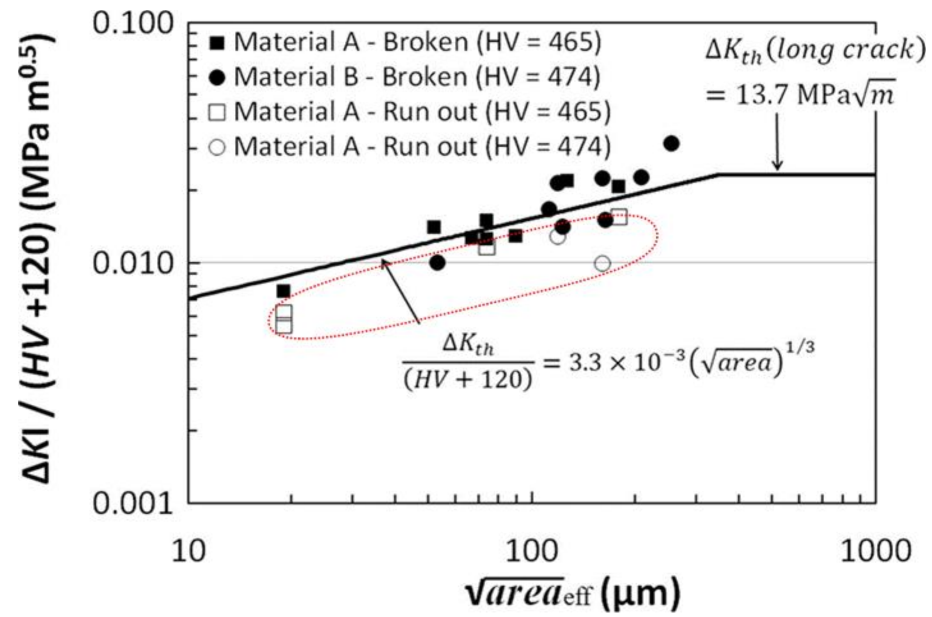

Fig. 2.4. Relationship between the threshold SIF range for Mode I fatigue cracks, ΔK_{Ith}, and the defect size, $\sqrt{area}$, in two different AM Alloy 718 samples. The datum of ΔK_{Ith} is indicated by a dotted red line [14].

2.2 Experimental methods

2.2.1 Materials

Round bars of Alloy 718 measuring 19 mm in diameter and 100 mm in length were fabricated by L-BPF process with a laser power of 960 W and a build rate of 20 mm^3/s. The as-built bar was subjected to solution treatment and aging (STA), solution-treated at 955 °C for 0.5 h and subsequently, double-aged for 8 h at 720 °C and 620 °C, respectively. In addition to the AM material, WR Alloy 718 rod with diameters of 30 mm was referenced so as to comparably assess the fatigue crack-growth resistance. The WR alloy was solution-treated at 955 °C for 1 h and double-aged at 718 °C and at 621 °C for 8 h, respectively. The chemical compositions of the AM powders and the WR material are listed in Table 2.1. Experimental data for WR can be found in the previous studies of Tanaka *et al.* [12] and Kevinsanny *et al.* [15].

Fig. 2.5 presents the initial microstructures of all the samples observed *via* electron backscatter diffraction (EBSD), backscatter electron (BSE) imaging and energy-dispersive X-ray (EDX) techniques in a scanning electron microscope (SEM). The AM sample exhibited elongated grains extending to several deposit layers, with preferential orientation along the [001] crystal direction with respect to BD, as shown in inverse pole figure (IPF) maps of Fig. 2.5(a), the result of the epitaxial and directional solidification. Conversely, the WR material displayed equiaxed and randomly-oriented grains, with no significant crystallographic texture with respect to the axial direction of the base material, as seen in Fig. 2.5(d). It is noted that similar features were observed on the surface of a fatigue test specimen of the WR material in a direction perpendicular to the axial direction (*cf.* Fig. 4.3(b)). The SEM-BSE image reveals that Laves phases and δ phases were dispersed both within grain interior (*i.e.*, intragranular) and along grain boundaries (GBs) (*i.e.*, intergranular) in AM sample, resulting from the micro-segregation of elements such as Nb and Mo during solidification in the AM process, as shown in Fig. 2.5(c) and Table 2.2, obtained by EDX technique. On the other hand, the presence of δ phases was solely observed along GBs in WR with no Laves phases identified (*cf.* Fig. 2.5(e)). The mechanical properties (0.2 % proof stress, $\sigma_{0.2}$, tensile strength, σ_B, and Vickers hardness, *HV*, with the standard deviation (SD)) measured in ambient air at room temperature are documented in Table 2.3. The Vickers hardness, *HV*, was an average value of 20-point data measured with a load of 9.8 N and a holding time of 30 s.

2.2.2 Test procedures

Fig. 2.6 illustrates the shapes and dimensions of the specimens. Some of the AM round bars were fabricated into torsional fatigue specimens with no artificial defects, *i.e.*, smooth condition, as shown in Fig. 2.6(a). This condition was chosen to facilitate the comparison of fatigue data between the present study and the literature, specifically a study by Tanaka *et al.* [12]. On the other hand, the other AM bars were machined into push-pull fatigue specimens (*cf.* Fig. 2.6(b)) onto which small, semicircular notch was introduced *via* electrical discharge machining (EDM) (*cf.* Fig. 2.6(c)). The size of the notch was determined based on the average grain size of 105 μm, calculated from the initial microstructure (*cf.* Fig. 2.5(a)). The introduction of an artificial notch not only eases the observation of crack-growth behavior by confining the crack initiation site, but also enables an accurate evaluation of the stress intensity factor. All of the specimen axes were parallel to BD. All specimen surfaces were polished with emery papers, followed by buffing with a diamond paste. In the case of the EDM-notch specimen, the surface was polished prior to the introduction of the notch.

Torsional fatigue tests were conducted with a resonance fatigue-testing machine, developed by Endo *et al.* [16], operated at a stress ratio, R, of −1 and a test frequency, f, of 50 Hz. Push-pull fatigue tests were executed using a servo-hydraulic fatigue-testing machine at R of −1, and f of 10 Hz. The test frequency of each test was selected within the allowable range to ensure stable control of each testing machine. Prior to the tests, the alignment between the specimen and the loading axes was carefully adjusted to ensure that no bending stress was exerted on the test section. The torsional fatigue limit, τ_w, was determined by the maximum level of shear-stress amplitude, τ_a, at which a specimen did not fail after loading at 10^8 cycles. On the other hand, in push-pull fatigue tests, the fatigue limit, σ_w, was determined by the maximum level of normal-stress amplitude, σ_a, at which a specimen did not fail during 10^7 cycles due to the limitation of loading frequency at 10 Hz. All tests were carried out in ambient air at room temperature. The tests were periodically halted to examine the propagation of fatigue cracks using the plastic replica method. When a crack did not proliferate during two million cycles under push-pull loading or during twenty million cycles under torsional cyclic loading, taking into account the total loading cycles in each case, the crack was considered to be a non-propagating crack.

Table 2.1 Chemical compositions of AM powders and WR material (mass %).

Material	C	Si	Mn	P	S	Ni	Cr	Mo	Co	Cu	Al	Ti	Nb	B	Ta	Fe
AM						52.18	19.24	3.08	0.03		0.61	0.91	5.17			Bal.
WR	0.04	0.06	0.09	0.01	0.005	53.93	17.89	2.96	0.25	0.07	0.55	0.98	5.41	0.005	0.01	17.50

Table 2.2 EDX analysis on chemical composition of matrix and Laves phase (mass %).

Point (phase)	Ni	Fe	Cr	Nb	Mo	Ti
1 (Matrix)	52.5	18.4	18.8	5.3	4.0	0.9
2 (Laves phase)	46.5	15.5	16.7	12.6	7.6	1.6

Table 2.3 Mechanical properties of AM and WR materials.

Materials	$\sigma_{0.2}$ [MPa]	σ_B [MPa]	*HV* (SD)
AM	1134	1351	470 (± 12)
WR	1207	1420	456 (± 10)

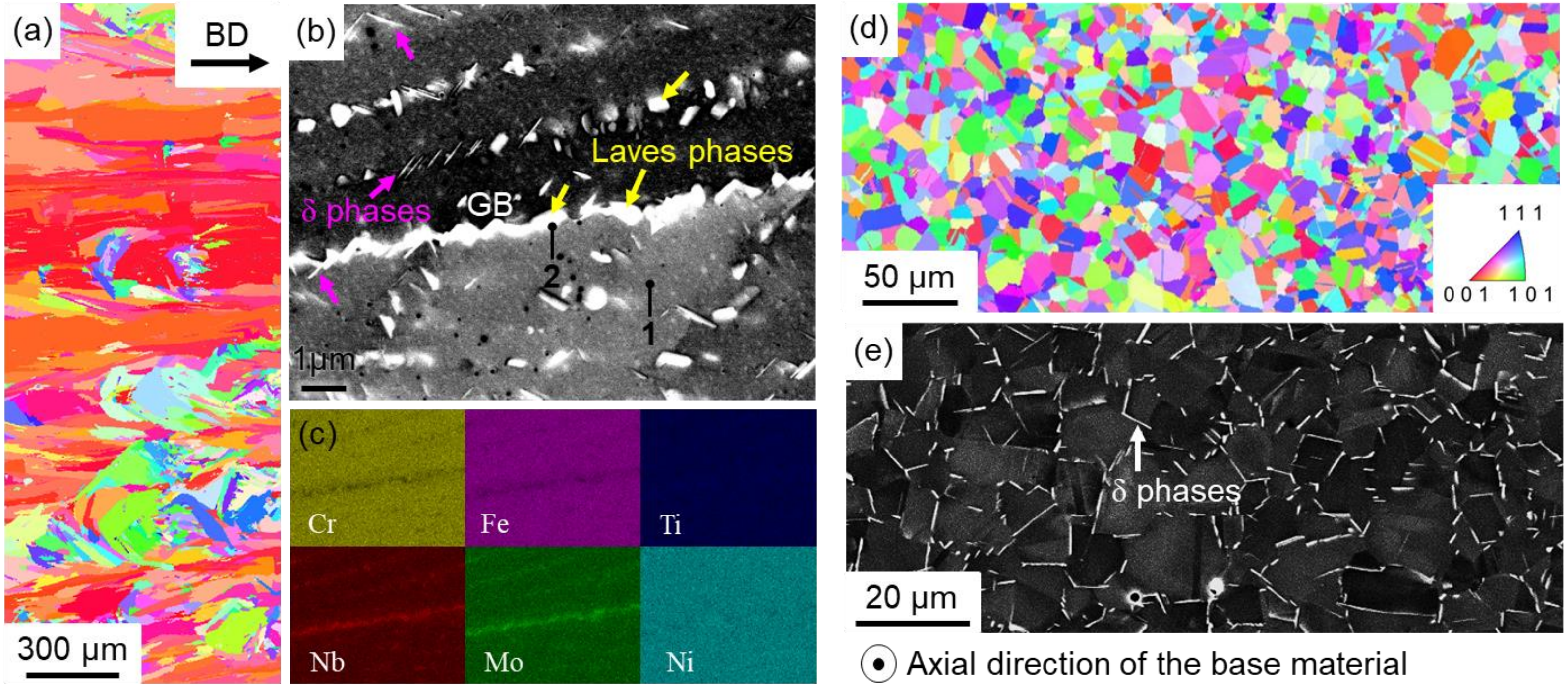

Fig. 2.5. Initial microstructures of Alloy 718 used in this study: (a) IPF map and (b) BSE image of AM with reference to BD; (c) EDX mapping corresponding to BSE image of (b); (d) IPF map and (e) BSE image of WR with reference to the axial direction of the base material. (Numbers in BSE image represent points for EDX analysis shown in Table 2.2.)

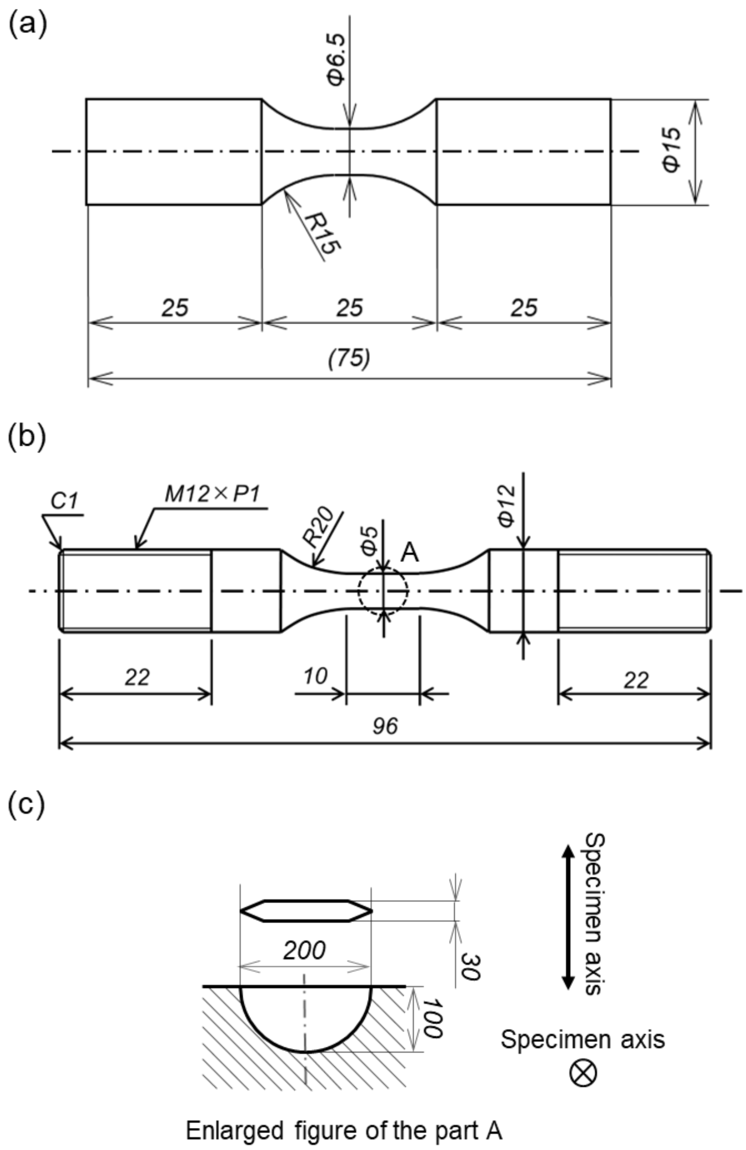

Fig. 2.6. Shapes and dimensions of: (a) torsional fatigue test specimen (in mm); (b) EDM-notch specimen for the push-pull fatigue tests (in mm); (c) small, semicircular EDM notch (in μm).

2.3 Results and discussion

2.3.1 Torsional fatigue test results

The *S-N* data for AM, obtained by the torsional fatigue testing of smooth specimens, are featured in Fig. 2.7. For the sake of comparison, the torsional fatigue data are also plotted for the WR specimen with the same surface condition, conducted at an identical stress ratio and frequency [12]. It should be noted that the fatigue limit of AM was nearly 45 % lower than that of WR. Moreover, in run-out AM specimens, some small, grain-sized fatigue cracks which initiated from either the matrix or the defect were observed on the surface, almost parallel to the maximum shear-stress direction (*cf.* Fig. 2.8(a) and (b)). Through periodic crack-propagation observations using the plastic replica method, as shown in Fig. 2.8, these shear-mode cracks were deemed to either stop growing or to propagate at an extremely slow rate. Hence, the presence of these shear-mode arrested cracks suggests that the fatigue limit of the AM materials can be determined by the threshold SIF range for shear-mode fatigue cracks, $\Delta K_{\tau th}$, under cyclic torsional loading, analogous to the results of the torsional fatigue tests of WR materials reported by Tanaka *et al.* [12]. Furthermore, when the $\Delta K_{\tau th}$ values of the two materials were assessed to quantify the effects of small defects, a dramatic degradation of the fatigue strength of AM was also revealed, as compared to that of WR, as will be later demonstrated.

2.3.2 Push-pull fatigue test results

Fig. 2.9 presents the *S-N* data for AM as obtained from push-pull fatigue tests using the EDM-notch specimen. The fatigue test results for WR specimens with EDM-notches [10] are also presented in the figure. Despite the same defect size ($\sqrt{area}$ = 125 μm for EDM-notch), the fatigue limit of AM (*i.e.*, 240 MPa) was significantly inferior to that of WR (*i.e.*, 390 MPa), a phenomenon that cannot be explained solely by the effect of defects. Rather, it suggests the presence of intrinsic factors dominating the fatigue strength in these materials, to be further examined in later chapters.

Fig 2.10 showcases BSE images of an arrested crack at the fatigue limit observed in notched AM specimens of the push-pull fatigue tests, marked by a white rectangle in Fig.

2.10(a). In the figure, the arrest crack seems to be a Mode I crack. However, a higher magnification view at the notch-tip revealed that crack was arrested in the vicinity of GBs, indicated by dotted yellow lines, after propagating and branching along the {111} slip planes, as indicated by solid white lines (*cf.* Fig. 2.10(b)). This experimental finding implies that the local shear stress ahead of the crack-tip is the primary crack driving-force at the fatigue limit. Therefore, it was presumed that the fatigue limit under fully-reversed, uniaxial cyclic-loading was governed by the shear-mode crack-growth threshold, $\Delta K_{\tau\mathrm{th}}$.

On the other hand, the crack that propagated along a direction that closely aligned with the maximum shear-stress direction, with a slight deviation due to the grain orientation, as evidenced in Fig. 2.10(a), was obtained by a subsequent test of the run-out AM specimen at a stress amplitude some 20 MPa higher than the fatigue limit (*cf.* Fig. 2.10(a)). The test was conducted to examine the behavior of small fatigue cracks near the threshold stress, which will be discussed further in Chapter 4. It is noted that the crack arrested at the fatigue limit did not propagate further, even after the stress amplitude was increased to 260 MPa. In contrast, the crack that was initiated at 260 MPa continued to propagate. These results may be attributed to multiple factors, including the interaction between adjacent cracks (between branched cracks or between non-propagating and propagating cracks), the influence of local microstructures on each crack, and the potential effect of the loading history, such as the coaxing effect. However, the specific underlying reason for these observations has not been clarified in this study.

2.3.3 Evaluation of the shear-mode, fatigue crack-growth threshold

According to the results of the previous subsection, it is deemed that the fatigue limit of AM Alloy 718 is the threshold condition of a shear-mode crack, irrespective of loading conditions (*i.e.*, torsion and push-pull). In the case of torsional fatigue testing of the smooth specimen, the non-propagating crack was found to be lying on the maximum shear-stress plane (*cf.* Fig. 2.8). In contrast, regarding the push-pull fatigue test of the notched specimen, the arrested crack did not macroscopically lie on the maximum shear-stress plane, although the primary driving force for the crack at the fatigue limit is the local shear stress ahead of the crack tip. Such a shear-mode threshold under the two conditions will be quantified in the ensuing sections.

For shear-mode cracking under cyclic torsion, Okazaki *et al.* [18] proposed the following formula to evaluate threshold SIF ranges on the basis of the $\sqrt{area}$ parameter model:

$$\Delta K_{\tau\mathrm{th}} = 2 \times 0.69 \tau_{\mathrm{w}} \sqrt{\pi \sqrt{area_{\tau}}} \tag{2.3}$$

where $\sqrt{area_{\tau}}$ is the square root of the area of the crack or defect projected onto the maximum shear-stress plane. Since an accurate crack-shape with respect to depth direction was not identified in this study, the crack generated from the defect was assumed to arrest in a hemispherical surface grain, thus possessing a semicircular shape (*i.e.*, $\sqrt{area_{\tau}} = \sqrt{\pi/2}\,a$, where a is the half-length of the surface crack) (*cf.* Fig. 2.11). Consequently, $\Delta K_{\tau\mathrm{th}} = 1.5$ MPa·m$^{1/2}$ was derived by inserting $\tau_{\mathrm{w}} = 130$ MPa and $\sqrt{area_{\tau}} = 22$ μm into Eq. (2.3).

On the other hand, thin EDM-notch including the arrested crack (Fig. 2.6(b)) under push-pull loading can almost be mechanically equivalent to a planar crack normal to the loading axis. The SEM observation (*cf.* Fig. 2.10) revealed that the crack emanating from the notch grew along the {111} slip plane by the driving force associated with local shear stress at the notch-tip. Hence, the present study examined the normal and shear stress distributions in the vicinity of the tip of a Mode I crack in an infinite plane under remote tension, σ_0, illustrated in Fig. 2.12(a). The elasticity solutions for the distribution of normal stress in θ direction, σ_θ, and shear stress, $\tau_{r\theta}$, in the vicinity of the tip are provided with the polar coordinates (r, θ) as follows [3]:

$$\sigma_\theta = \frac{K_{\mathrm{I}}}{\sqrt{2\pi r}}\left(\frac{3}{4}\cos\frac{\theta}{2} + \frac{1}{4}\cos\frac{3\theta}{2}\right) \tag{2.4}$$

$$\tau_{r\theta} = \frac{K_{\mathrm{I}}}{\sqrt{2\pi r}}\left(\frac{1}{4}\sin\frac{\theta}{2} + \frac{1}{4}\sin\frac{3\theta}{2}\right) \tag{2.5}$$

where K_{I} is Mode I SIF. Referring to Eqs. (2.4) and (2.5), the normalized stresses near the tip as functions of an angle θ are depicted in Fig. 2.12(b). It should be noted that the magnitude of each stress component varies depending on the angle. The maximum normal stress, $\sigma_{\theta\max}$, and the maximum shear stress, $\tau_{r\theta\max}$, occurred along the direction of $\theta = 0°$ and $\pm70.5°$, respectively.

The maximum Mode I SIF range, $\Delta K_{I\theta\max}$, and the maximum shear-mode SIF range, $\Delta K_{\tau\theta\max}$, are thus defined as follows, respectively:

$$K_{I\theta\max} = \sigma_{\theta\max}\sqrt{2\pi r} \tag{2.6}$$

$$K_{\tau\theta\max} = \tau_{r\theta\max}\sqrt{2\pi r} \tag{2.7}$$

Based on Fig. 2.12(b) and Eqs. (2.6) and (2.7), the ensuing relationship is derived between the maximum Mode I SIF range and the maximum shear-mode SIF range under fully-reversed, push-pull loading:

$$\Delta K_{I\theta\max} = 2.598\Delta K_{\tau\theta\max} \tag{2.8}$$

Equation (2.8) indicates that even when only remote uniaxial stress is applied (*i.e.*, Mode II SIF, $K_{II} = 0$, macroscopically), the local shear-stress field is formed in the vicinity of the crack-tip so that the crack can propagate in shear mode. $\Delta K_{I\theta\max}$ can be calculated by using the formula proposed by Murakami [19]:

$$\Delta K_{I\theta\max} = 2\times0.65\sigma_0\sqrt{\pi\sqrt{area_P}} \tag{2.9}$$

where $\sqrt{area_P}$ is the square root of the area of a crack or defect projected onto the principal stress plane. Using Eqs. (2.8) and (2.9) for AM, the $\Delta K_{I\theta\max} = 6.2$ MPa·m$^{1/2}$ was obtained from $\sigma_w = 240$ MPa and $\sqrt{area_P}$ = 125 μm, yielding $\Delta K_{\tau th} = 2.4$ MPa·m$^{1/2}$.

The $\Delta K_{\tau th}$ values gathered as a function of $\sqrt{area}$ (*i.e.*, $\sqrt{area_\tau}$ or $\sqrt{area_P}$) are provided in Fig. 2.13. For comparison purposes, also plotted in the figure are the results of torsion and push-pull fatigue tests using smooth specimens of two WR alloys [12], including WR and solution-treated samples without aging, duly labelled WR-ST, and the result of push-pull fatigue tests using smooth specimens of a coarse-grained WR alloy (WR-CG) [13]. It is noteworthy to mention that threshold values of the AM material exhibit a crack-size dependence, *i.e.*, $\Delta K_{\tau th} \propto (\sqrt{area})^{1/3}$, similar to the result gained from WR materials [12,13].

With respect to the crack-size dependence of $\Delta K_{\tau th}$ in the small-crack regime, Tanaka *et al.* [12] proposed the following relationship for WR Alloy 718 as demonstrated in Fig. 2.13:

$$\Delta K_{\tau th} = 1.01(\sqrt{area})^{1/3} \tag{2.10}$$

All the experimental results for WR Alloy 718 are in accordance with the aforementioned crack-size dependence in the regime of 10 μm < $\sqrt{area}$ < 300 μm [12,13].

Based on the above results, it was assumed that the crack-size dependence of $\Delta K_{\tau th}$ in the small-crack regime for the AM material can also be formulated by the least squares fitting in the regime of 10 μm < $\sqrt{area}$ < 300 μm as follows:

$$\Delta K_{\tau th} = 0.50(\sqrt{area})^{1/3} \tag{2.11}$$

It must be noted that the preceding results highlight the inferior small-crack resistance of the AM material compared to that of WR materials, in spite of their similar mechanical properties outlined in Table 2.3. Since the influence of defects on the fatigue strength of these alloys was quantitatively expressed by the crack-size dependence of $\Delta K_{\tau th}$, the reduced $\Delta K_{\tau th}$ value of the AM alloy for the same defect size (*cf.* Eqs. (2.10) and (2.11)) should be attributed to any factors other than defects. Therefore, in the next chapters, some possible dominant factors for $\Delta K_{\tau th}$ will be examined by focusing on notable features of AM microstructures as compared to WR ones.

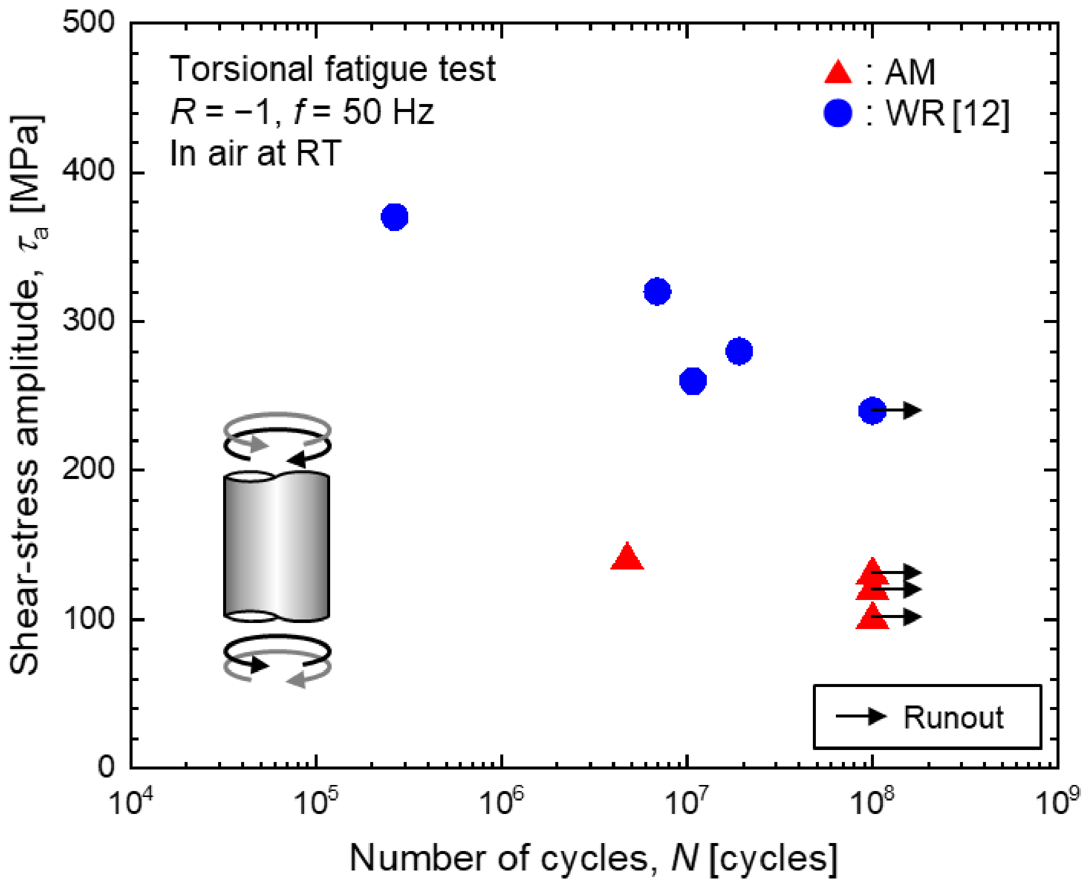

Fig. 2.7. *S-N* data obtained *via* torsional fatigue tests.

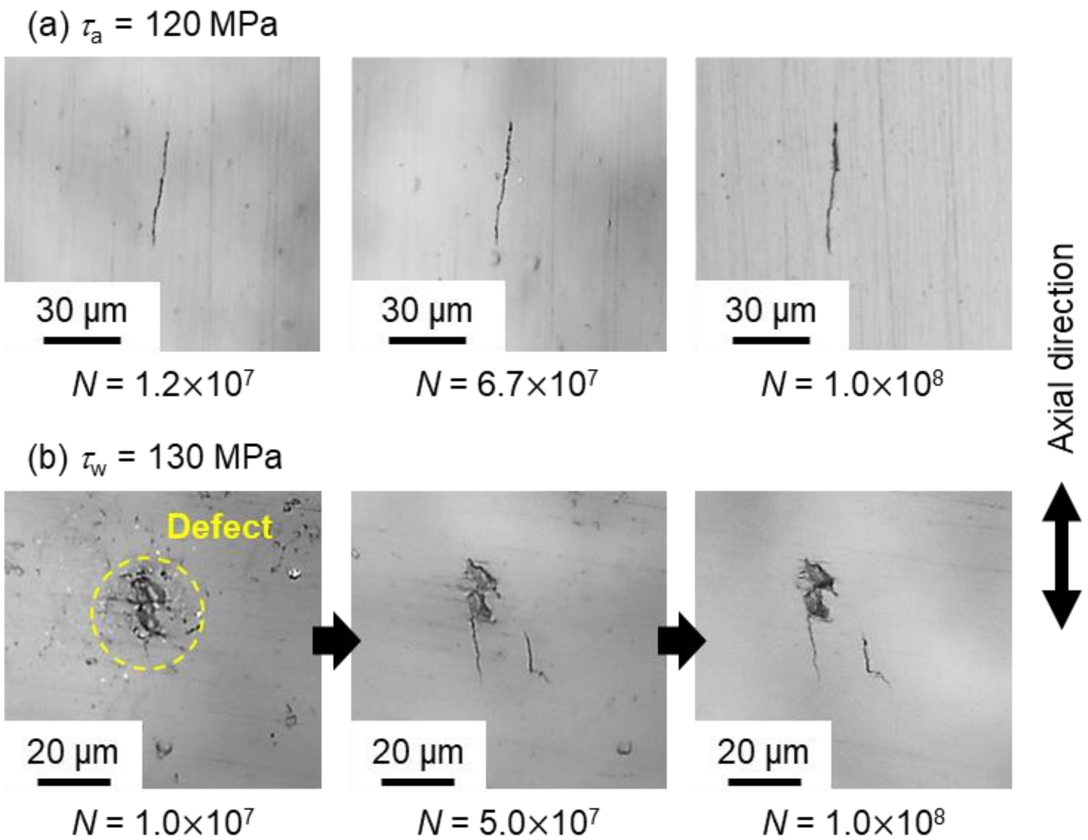

Fig. 2.8. Plastic replica observation of non-propagating cracks in AM run-out specimens tested at (a) τ_a = 120 MPa; (b) τ_w = 130 MPa.

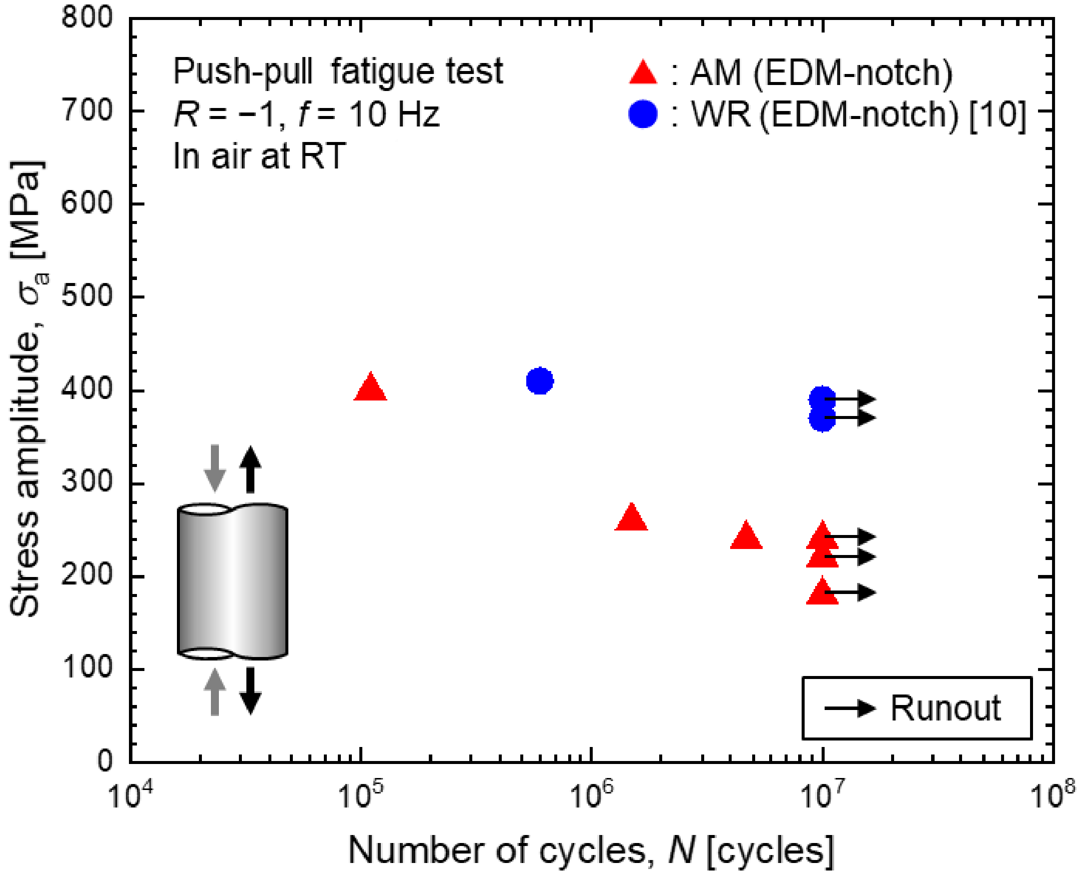

Fig. 2.9. *S-N* data obtained *via* push-pull fatigue tests.

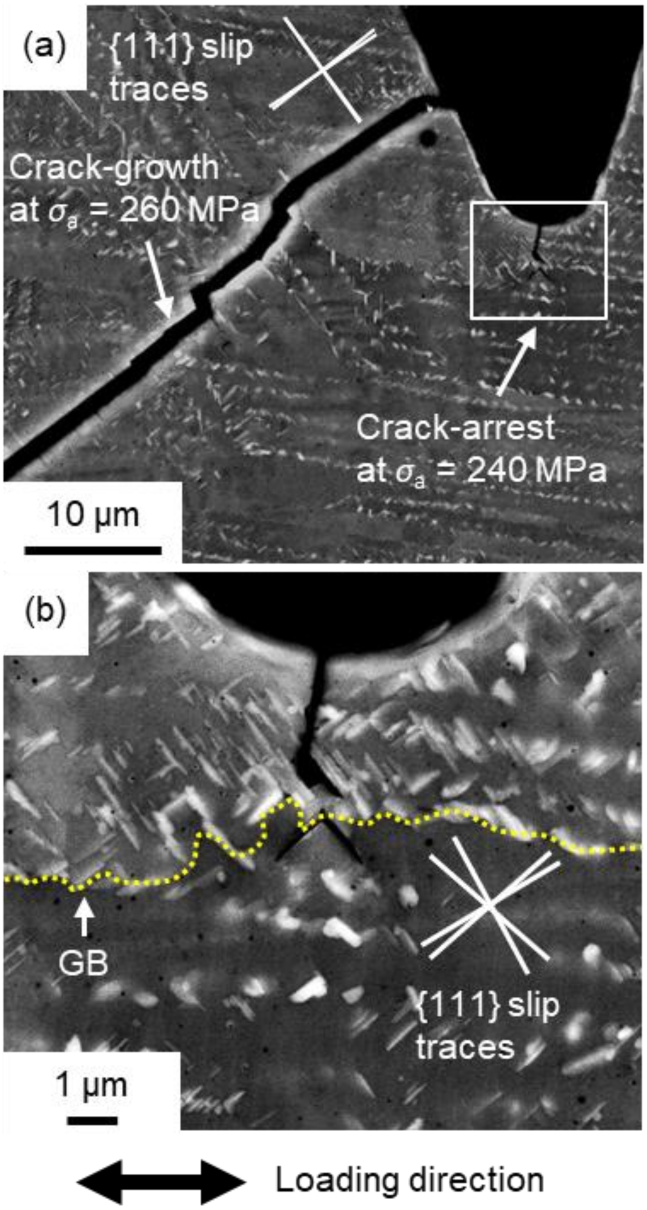

Fig. 2.10. (a) BSE image of fatigue crack emanating from EDM-notch under push-pull loading; (b) correspond to the region marked by white rectangle in (a).

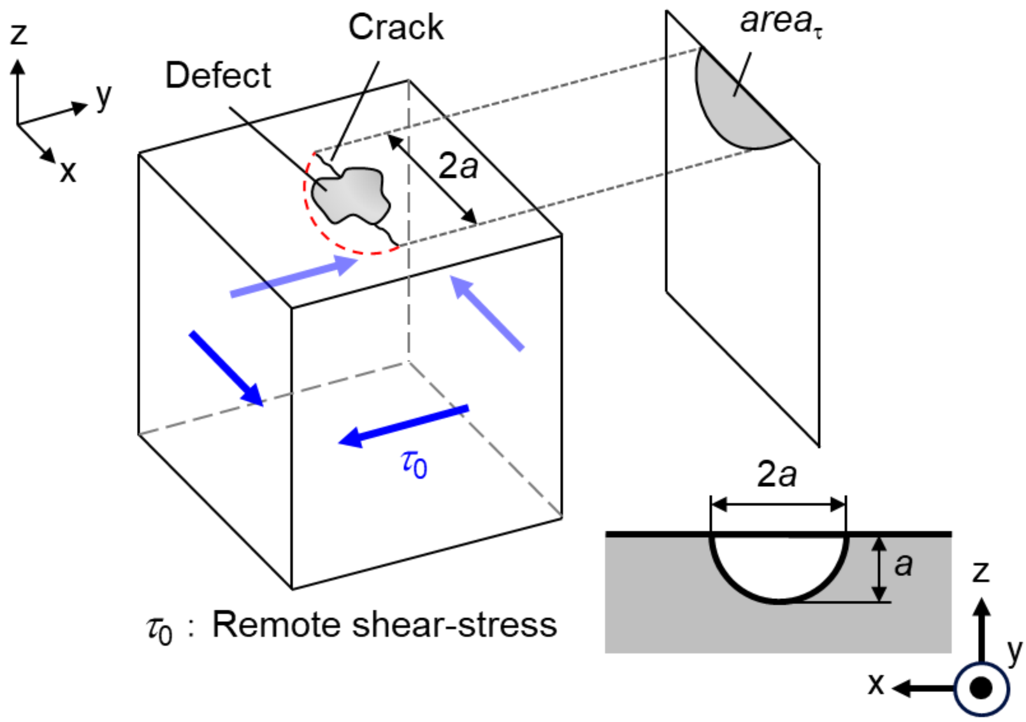

Fig. 2.11. Estimation of the area of defect plus crack projected onto the maximum shear-stress plane, $area_{\tau}$, for torsional fatigue test. The crack-shape with respect to depth direction was assumed to be semicircular, as indicated by a dashed red line.

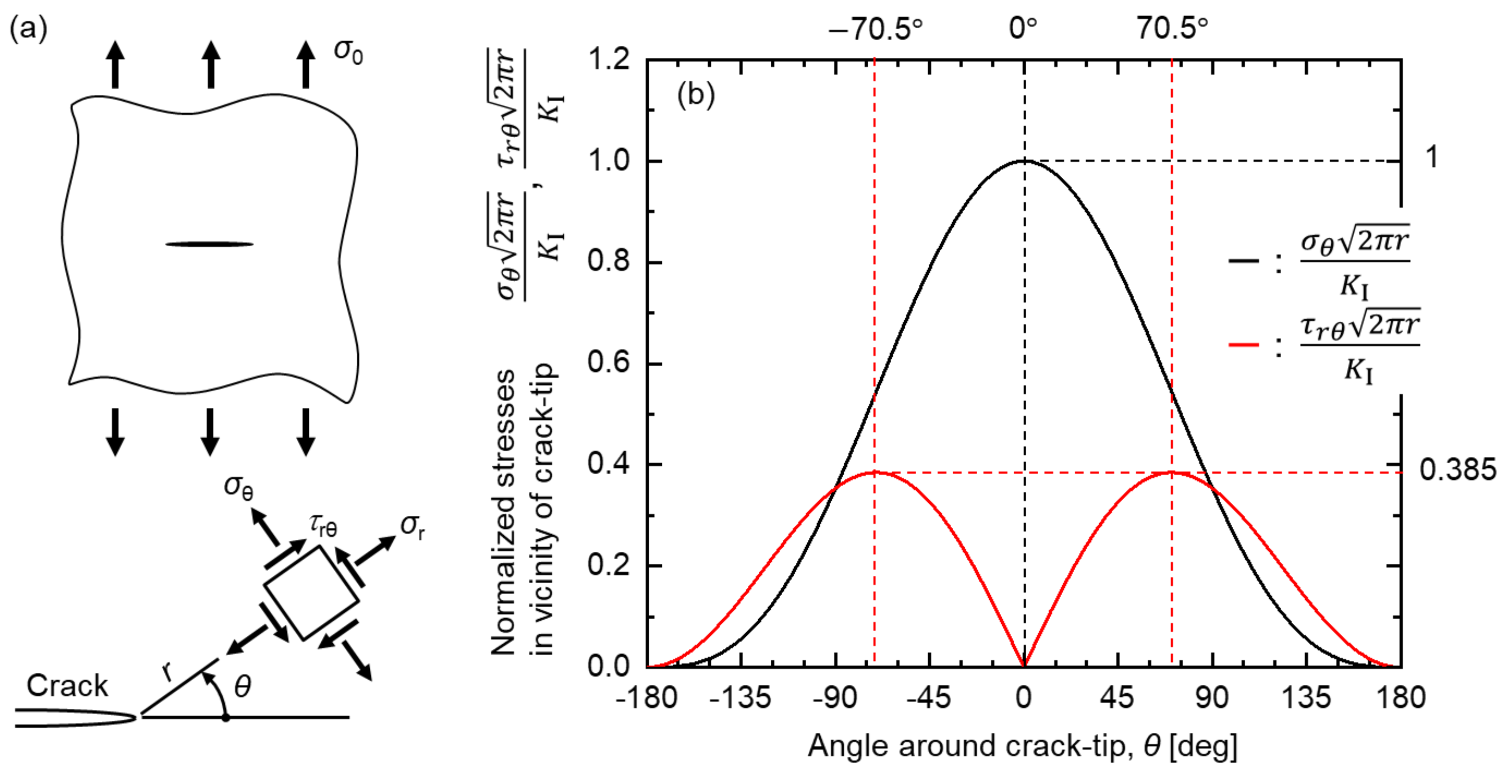

Fig. 2.12. (a) Definition of the stresses near the tip of a Mode I crack under remote tension; (b) normalized stresses as a function of an angle around crack-tip.

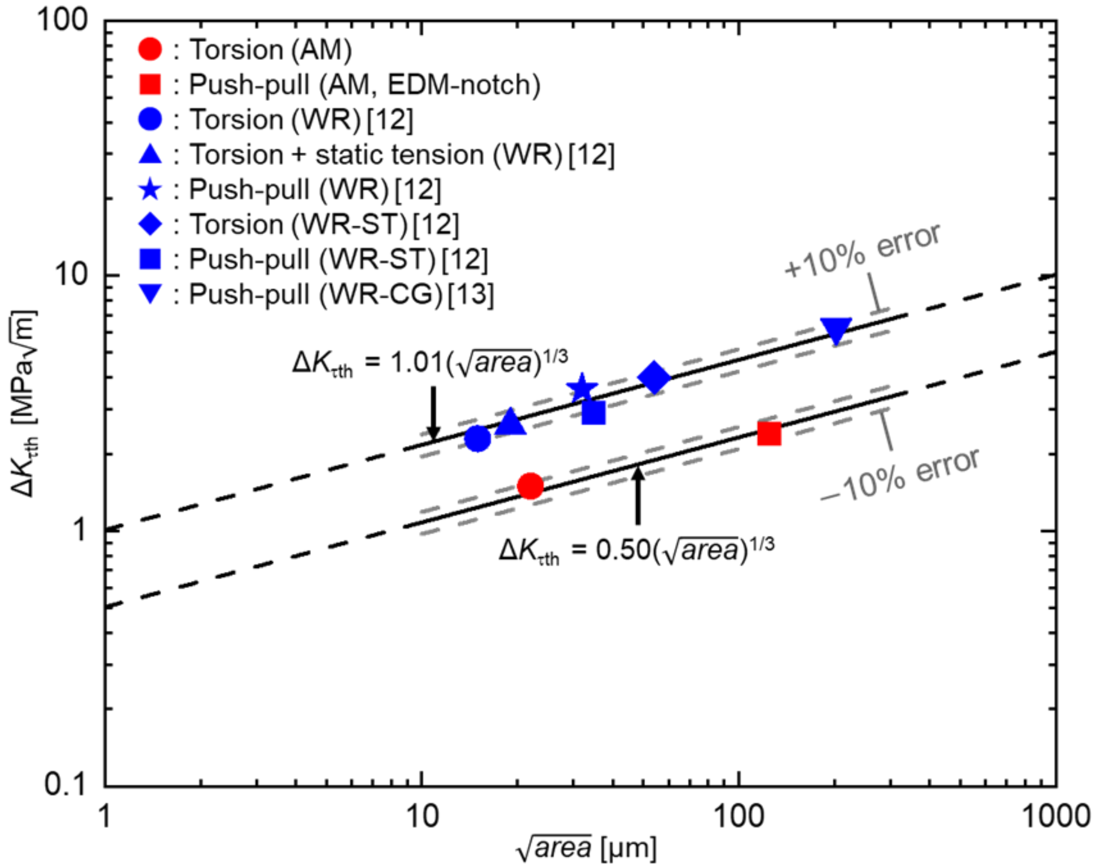

Fig. 2.13. $\Delta K_{\tau\mathrm{th}}$ of AM and WR Alloy 718 as a function of $\sqrt{area}$. The regression line (solid black line) is defined using the least squares fitting for all experimental data.

2.4 Conclusion

In this chapter, the fatigue limit of an additively-manufactured, Ni-based superalloy 718 was evaluated in terms of the fatigue crack-growth threshold. Based on the macro- and microscopic analyses, the determining mechanism of the fatigue limit and the effects of small defects were all thoroughly explored. The principal conclusions are summarized as follows:

1. AM sample possessed elongated grains extending to several deposit layers, with a strong crystallographic texture along the [001] crystal direction relative to the build direction. Moreover, Laves and δ phases were observed both within grain interiors and along grain boundaries.

2. Fatigue tests revealed that small-crack behavior at the fatigue limit was governed by maximum shear stress under both cyclic torsional loading and push-pull loading. This implied that the fatigue limit of all the samples was the threshold condition of a shear-mode, small fatigue-crack propagation, similar to the findings related to wrought materials.

3. In each case, the shear-mode, fatigue-crack growth-threshold, $\Delta K_{\tau\mathrm{th}}$, was estimated to quantify the effects of small defects. As a result, the relationship between the $\Delta K_{\tau\mathrm{th}}$ and defect size could be formulated in an expression of $\Delta K_{\tau\mathrm{th}} = 0.50(\sqrt{area})^{1/3}$.

4. The aforementioned experimental results demonstrate not only a crack-size dependence consistent with the results of wrought materials, but also a substantially low fatigue resistance of additively-manufactured materials. The dominant factors contributing to this reduced fatigue resistance should be systematically elucidated, a topic of the following chapters.

References

[1] FORTH S, NEWMAN J, FORMAN R. On generating fatigue crack growth thresholds. Int J Fatigue 2003;25:9–15. https://doi.org/10.1016/S0142-1123(02)00066-X.

[2] Kitagawa H, Takahashi S. Fracture mechanical approach to very small fatigue cracks and to the threshold. Trans Jpn Soc Mech Eng 1979;45:1289–303.

[3] Murakami Y. Theory of elasticity and stress concentration. John Wiley & Sons; 2016.

[4] Ravichandran KS, Murakami Y, Ritchie RO. Small Fatigue Cracks: Mechanics, Mechanisms and Applications. Elsevier Science; 1999.

[5] Murakami Y. Metal fatigue: effects of small defects and nonmetallic inclusions. Academic Press; 2019.

[6] Murakami Y, Endo M. Effects of defects, inclusions and inhomogeneities on fatigue strength. Int J Fatigue 1994;16:163–82. https://doi.org/10.1016/0142-1123(94)90001-9.

[7] Schönbauer BM, Yanase K, Endo M. The influence of various types of small defects on the fatigue limit of precipitation-hardened 17-4PH stainless steel. Theor Appl Fract Mech 2017;87:35–49. https://doi.org/10.1016/j.tafmec.2016.10.003.

[8] Åman M, Wada K, Matsunaga H, Remes H, Marquis G. The influence of interacting small defects on the fatigue limits of a pure iron and a bearing steel. Int J Fatigue 2020;135. https://doi.org/10.1016/j.ijfatigue.2020.105560.

[9] Beretta S, Romano S. A comparison of fatigue strength sensitivity to defects for materials manufactured by AM or traditional processes. Int J Fatigue 2017;94:178–91. https://doi.org/10.1016/j.ijfatigue.2016.06.020.

[10] Kevinsanny, Okazaki S, Takakuwa O, Ogawa Y, Okita K, Funakoshi Y, et al. Effect of defects on the fatigue limit of Ni-based superalloy 718 with different grain sizes. Fatigue Fract Eng Mater Struct 2019;42:1203–13. https://doi.org/10.1111/ffe.12989.

[11] Okazaki S, Okuma S, Kevinsanny, Ogawa Y, Kawashima H, Funakoshi Y, et al. Unforeseen, negative interaction-effect of adjacent circumferential notches on the fatigue limit of Ni-based superalloy 718. Eng Fract Mech 2021;257:108015. https://doi.org/10.1016/j.engfracmech.2021.108015.

[12] Tanaka Y, Okazaki S, Ogawa Y, Endo M, Matsunaga H. Fatigue limit of Ni-based superalloy 718 relative to the shear-mode crack-growth threshold: A quantitative evaluation considering the influence of crack-opening and -closing stresses. Int J Fatigue 2021;148:106228. https://doi.org/10.1016/j.ijfatigue.2021.106228.

[13] Kevinsanny. Effect of defects and hydrogen on the fatigue limit properties of forged and additive manufactured Ni-based superalloy 718. Master Thesis, Kyushu University, 2019.

[14] Yamashita Y, Murakami T, Mihara R, Okada M, Murakami Y. Defect analysis and fatigue design basis for Ni-based superalloy 718 manufactured by selective laser melting. Int J Fatigue 2018;117:485–95. https://doi.org/10.1016/j.ijfatigue.2018.08.002.

[15] Kevinsanny, Okazaki S, Takakuwa O, Ogawa Y, Okita K, Funakoshi Y, et al. Effect of defects and hydrogen on the fatigue limit of Ni-based superalloy 718. Procedia Struct Integr 2019;19:312–9. https://doi.org/10.1016/j.prostr.2019.12.034.

[16] Endo M, Okazaki S, Matsunaga H, Moriyama S, Munaoka K, Yanase K. A New Fatigue Testing Machine for Investigating the Behavior of Small Shear-Mode Fatigue Cracks. Exp Tech 2016;40:1065–73. https://doi.org/10.1007/s40799-016-0102-0.

[17] Zeng L, Shikama T, Takahashi Y, Yoshihara S, Aiura T, Noguchi H. Fatigue limit of new precipitation-hardened aluminium alloy with distinct fatigue crack propagation limit. Int J Fatigue 2012;44:32–40. https://doi.org/10.1016/j.ijfatigue.2012.06.001.

[18] Okazaki S, Matsunaga H, Ueda T, Komata H, Endo M. A practical expression for evaluating the small shear-mode fatigue crack threshold in bearing steel. Theor Appl Fract Mech 2014;73:161–9. https://doi.org/10.1016/j.tafmec.2014.07.016.

[19] Murakami Y. Analysis of stress intensity factors of modes I, II and III for inclined surface cracks of arbitrary shape. Eng Fract Mech 1985;22:101–14. https://doi.org/10.1016/0013-7944(85)90163-8.

3. Dominant factors for inferior fatigue resistance of AM Alloy 718−Part 1: Influence of precipitates, grain size and residual stress

3.1 Introduction

In Chapter 2, it was revealed that the fatigue limit of AM Alloy 718 is 50% lower than that of WR alloys, with respect to the same defect size. This suggests the presence of a dominant factor, in addition to defects, that contributes to the inferior fatigue crack-growth resistance observed in the examined AM samples. Based on extensive literature review [1–13] and the comparison of microstructural features between AM and WR alloys demonstrated in the previous chapter, potential factors that can influence the fatigue resistance of Ni-based superalloys, irrespective of crack size, *i.e.*, small crack and large crack, are summarized in Fig. 3.1. It is noted that, in addition to the inherent microstructural characteristics mentioned in Section 1.2, factors such as boron content, grain size, hardening precipitates, and annealing twin boundaries (ATBs) are also considered. A brief review on their effects on fatigue resistance is provided as follows.

With regard to the boron, Xiao *et al*. [13] demonstrated that the increase of boron content can improve the long fatigue crack-growth threshold of WR Alloy 718. The authors suggested that, since boron atoms in solution act as obstacles to the dislocation movement by hindering the dislocation slip, they can enhance the FCG resistance. However, at room temperature, the effect of boron content within the range of 10 to 60 ppm on the fatigue threshold was negligible, whereas the content of 120 ppm notably enhanced the fatigue threshold. It should be highlighted that all AM and WR Alloy 718 materials examined in this study were found to possess a similar boron concentration in the ranges of 30 – 50 ppm. Therefore, it is deemed that the boron concentration is not dominant factor for the difference in fatigue resistance between AM and WR materials. For the effect of solution hardening by precipitates (*i.e.*, γ'' phases), Deng *et al*.[5] suggested that the coarsened γ'' phases lowered fatigue thresholds of WR Alloy 718, probably due to the decrease of shear-stress increments, which is based on the fact that when dislocations pass through precipitates by bypassing them, the shear-stress increments decrease as the precipitate size increases. In addition, a fine-grained microstructure is known to be beneficial to fatigue resistance because it provides a larger fraction of GBs, obstacles to dislocation motion [14]. On the other hand, a coarse-grained microstructure can also have advantages in terms of fatigue resistance by reducing the effective crack-growth driving force through the formation of tortuous crack paths (*i.e.*, crack tip shielding effects or roughness induced crack closure) [15,16]. In the case of ATBs, an enhancement of the fatigue resistance is generally expected from the higher volume of ATBs which can block dislocations like GBs [2], as seen for example in fatigue crack-growth testing of an austenitic stainless steel [1]. Nevertheless, impacts of these factors on small fatigue crack-growth resistance of this alloy remains still unclear since former research was associated with long fatigue cracks of which mechanism is essentially different from the small crack behavior near the threshold regime [17–19].

In this chapter, the effects of precipitates (*i.e.*, γ'' phases, δ phases and Laves phases), grain size and residual stress are explored. For this purpose, new AM Alloy 718 sample was prepared under different process condition to control the grain size. The sample was then subjected to HIP to not only remove the defects but also dissolve δ phases and Laves phases present in as-built AM sample. In addition, it is expected that this process can release any residual stress that might exist. Push-pull fatigue testing was conducted on specimens having as-machined surface with artificial notches and as-built surfaces. Based on the observation results of arrest cracks, the determining condition of fatigue limit and fatigue threshold were examined.

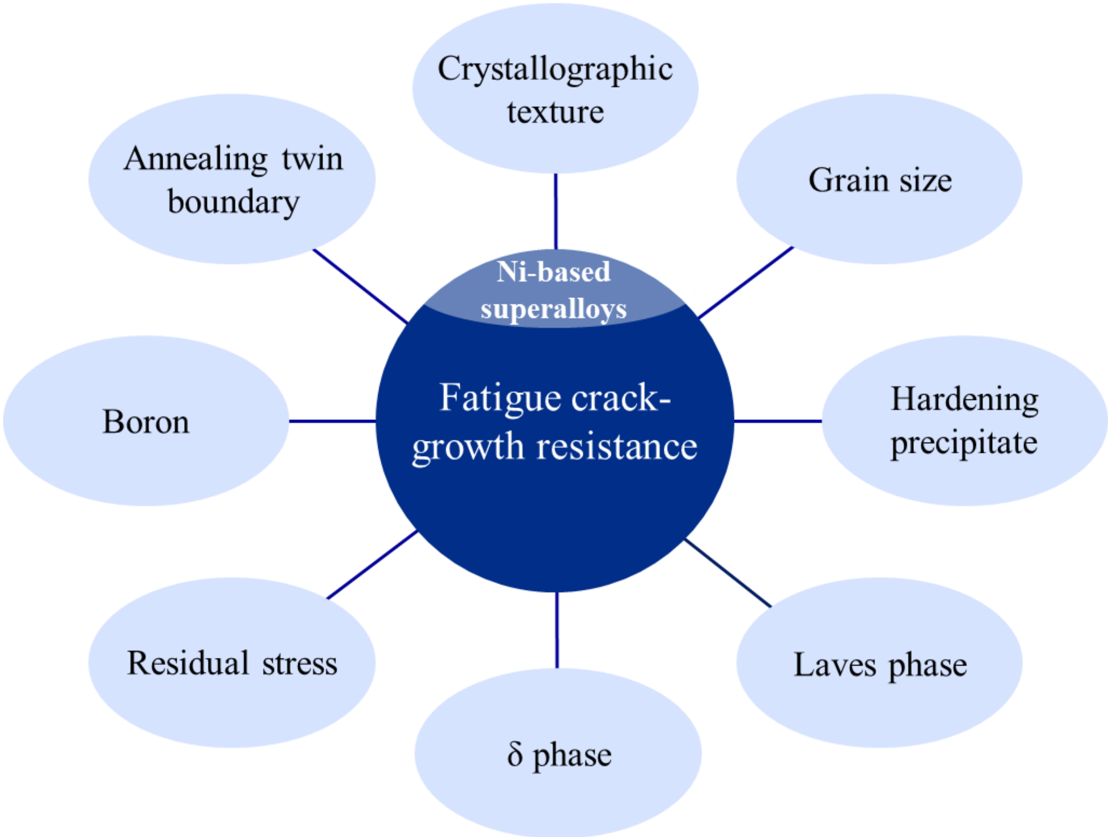

Fig. 3.1. Potential factors influencing fatigue crack-growth resistance of Ni-based superalloys.

3.2 Experimental methods

3.2.1 Materials

Round bars of Alloy 718 were fabricated by L-BPF process with a laser power of 350 W and a build rate of 5 mm^3/s, yielding the energy density (*i.e.*, the ratio of laser power to build rate) of 70 J/mm^3. The as-built bar was subjected to HIP at 1050°C and 150 MPa for 4 h prior to STA heat treatment. STA condition was the same as that of the AM material in Chapter 2. It should be noted that the process condition of the previous sample was a laser power of 960 W and a build rate of 20 mm^3/s, which yields the energy density of 48 J/mm^3. Hereafter, according to the energy density and the heat-treatment route, two AM materials in the previous and the current chapter were correspondingly identified as AM-L and AM-H-HIP. In addition, apart from the first WR alloy investigated in Chapter 2, the second WR Alloy 718 rod with diameters of 20 mm was prepared as a reference WR material. The second WR sample was solution-treated at 980°C for 1.5 h, while the first was solution-treated at 955°C for 1 h. Double-aging conditions were identical for both samples. Depending on their solution treatment temperatures, the first and second materials were labelled WR-L and WR-H, respectively. The chemical compositions of the WR-H are listed in Table 3.1.

Fig. 3.2 presents the initial microstructures of all the samples observed *via* EBSD, BSE imaging and EDX techniques. For comparison, observation results of AM-L (Fig. 3.2(a), (b) and (c)) and WR-L (Fig. 3.2(g) and (h)) are also displayed. Similar to AM-L, AM-H-HIP also exhibited columnar grain morphology with a preferred [001] crystallographic grain orientation along the BD, as shown in IPF maps of Fig. 3.2(d). Although detailed process parameters for both AM materials were not disclosed by the manufacturer, the resulting microstructure of AM-H-HIP was relatively fine-grained, *i.e.*, the average grain size is 105 μm for AM-L and 71 μm for AM-H-HIP. This can be potentially attributed to the higher energy density during the process of AM-H-HIP [20,21]. WR-H showed the microstructure similar to WR-L, *i.e.*, equiaxed grains with a weak crystallographic texture (*cf*. Fig. 3.2(g) and (i). The SEM-BSE image of AM-H-HIP reveals that δ phases and carbide particles were detected along the GB (*cf*. Fig. 3.2(e) and Table 3.2) while no Laves phases were identified, a fact attributed to the HIP temperature that was sufficiently high to dissolve prior Laves phases and δ phases into the matrix. Moreover, Fig. 3.3 showcases the distributions of misorientation angle for all experimental materials in this study, indicating that AM sample possesses a relatively high fraction of low angle grain boundaries (LAGBs) due to the strong texture with negligible content of annealing twin boundaries (ATBs), *i.e.*, misorientation angle of 60°, whereas WR sample has a relatively high portion of high angle grain boundaries (HAGBs) and ATBs. The average grain sizes were calculated from the initial microstructures. The heat treatment conditions, the microstructure characteristics and the mechanical properties measured in ambient air at room temperature are documented in Table 3.3.

3.2.2 Test procedures

Fig. 3.4 illustrates the shapes and dimensions of the specimens. It is noted that different types of specimens were fabricated for each test due to the different sizes of the initial round bars. Some of the AM-H-HIP round bars were fabricated into push-pull fatigue specimens, in which gauge sections of ≈ 7 mm in diameter remained with as-built conditions with rough surface and unfused powders, as shown in Fig. 3.4(a). In addition, one specimen of AM-H-HIP of 5 mm in diameter with a semicircular EDM-notch was manufactured for push-pull fatigue test (*cf.* Fig. 3.4(b) and (c)) due to the limited number of the initial materials. All of the specimen axes were parallel to BD. On the other hand, WR-H bar was machined into push-pull fatigue specimens, onto which a small semicircular EDM-notch with crack-like thin slits produced by the focused ion beam (FIB) at both ends, inclined at 45° with respect to the specimen axis, was introduced (*cf.* Fig. 3.4(d) and (e)). The introduction of FIB slits was aimed at sharpening the crack tip to facilitate the generation of non-propagating cracks along the direction of the maximum shear-stress plane. It was presumed that the effect of defect shape and orientation on fatigue limit of this alloy is not significant, based on the studies by Kevinsanny *et al.* [22] and Lorenzino *et al.* [23]. For all of the notched specimens, prior to the notch introduction, the surfaces were polished with emery papers, followed by buffing with a diamond paste.

Push-pull fatigue tests were executed using a servo-hydraulic fatigue-testing machine at R of −1, and f of 10 Hz. The fatigue limit, σ_w, was determined by the maximum level of normal-stress amplitude, σ_a, at which a specimen did not fail during 10^7 cycles. Note that, due to the limited number of the specimen, the EDM-notch specimen of AM-H-HIP was tested by increasing the stress amplitude (σ_a-increasing test) in steps of 20 MPa from the initial value which was predicted to be lower than the fatigue limit. When a crack generated from the notch did not propagate during an additional 2×10^6 cycles after an increase in stress amplitude, the crack was considered to be a non-propagating crack, and the fatigue limit was defined as the corresponding maximum stress amplitude. All the tests were conducted in ambient air at room temperature. Prior to the tests, the alignment between the specimen and the loading axes was carefully adjusted to ensure that no bending stress was exerted on the test section. Special attention was given to as-built specimens for which achieving a perfect axisymmetric shape during specimen fabrication can be challenging. The tests were periodically halted to examine the propagation of fatigue cracks using the plastic replica method.

Table 3.1 Chemical compositions of WR-H material (mass %).

Material	C	Si	Mn	P	S	Ni	Cr	Mo	Co	Cu	Al	Ti	Nb	B	Ta	Fe
WR-H	0.02	0.05	0.04	0.006	<0.001	52.74	18.53	3.04	0.13	0.04	0.55	0.89	5.28	0.004	0.01	18.56

Table 3.2 EDX analysis on chemical composition of matrix and precipitates (mass %).

Point (phase)	Ni	Fe	Cr	Nb	Mo	Ti
1 (Matrix)	52.5	18.4	18.8	5.3	4.0	0.9
2 (Laves phase)	46.5	15.5	16.7	12.6	7.6	1.6
3 (δ phase)	64.3	10.0	10.6	11.1	2.7	1.3
4 (Carbide)	5.0	1.4	1.8	78.4	5.5	7.9

Table 3.3 Heat treatment conditions, microstructure characteristics, and mechanical properties of materials.

Materials	Heat treatment conditions	Average grain size [μm]	Distribution of Laves and δ phases	Fraction of ATBs [%]	$\sigma_{0.2}$ [MPa]	σ_{B} [MPa]	*HV* (SD)
AM-L	Solution treatment: 955°C, 0.5 h → WQ Aging: 720°C, 8 h → FC, 620°C, 8 h → AC	105	Intragranular and intergranular Laves and δ phases	<1	1134	1351	470 (± 12)
AM-H-HIP	Hot isostatic pressing: 1050°C, 150MPa, 4 h → FC Solution treatment: 955°C, 0.5 h → WQ Aging: 720°C, 8 h → FC, 620°C, 8 h → AC	71	Intergranular δ phases	<1	1200	1381	486 (± 12)
WR-L	Solution treatment: 955°C, 1 h → WQ Aging: 718°C, 8 h → FC, 621°C, 8 h → AC	18		32	1207	1420	456 (± 10)
WR-H	Solution treatment: 980°C, 1.5 h → WQ Aging: 718°C, 8 h → FC, 621°C, 8 h → AC	8		40	1225	1460	463 (± 4)

"WQ" stands for water quenching, "FC" for furnace cooling and "AC" for air cooling.

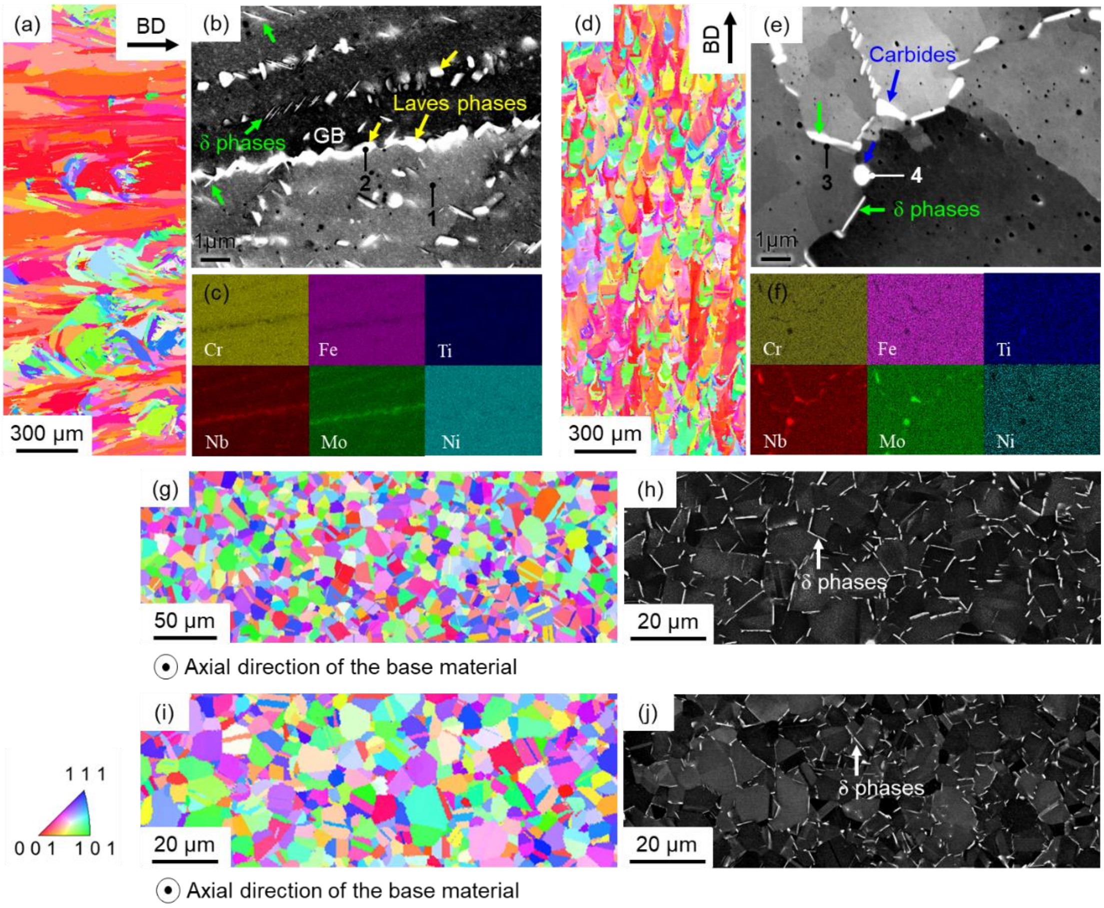

Fig. 3.2. Initial microstructures of Alloy 718 used in this study: (a)(d) IPF maps and (b)(e) BSE images of AM-L and AM-H-HIP with reference to BD; (c)(f) EDX mapping corresponding to BSE images of (b) and (e); (g)(i) IPF maps and (h)(j) BSE images of WR-L and WR-H with reference to the axial direction of the base material. (Numbers in BSE images represent points for EDX analysis shown in Table 3.2.)

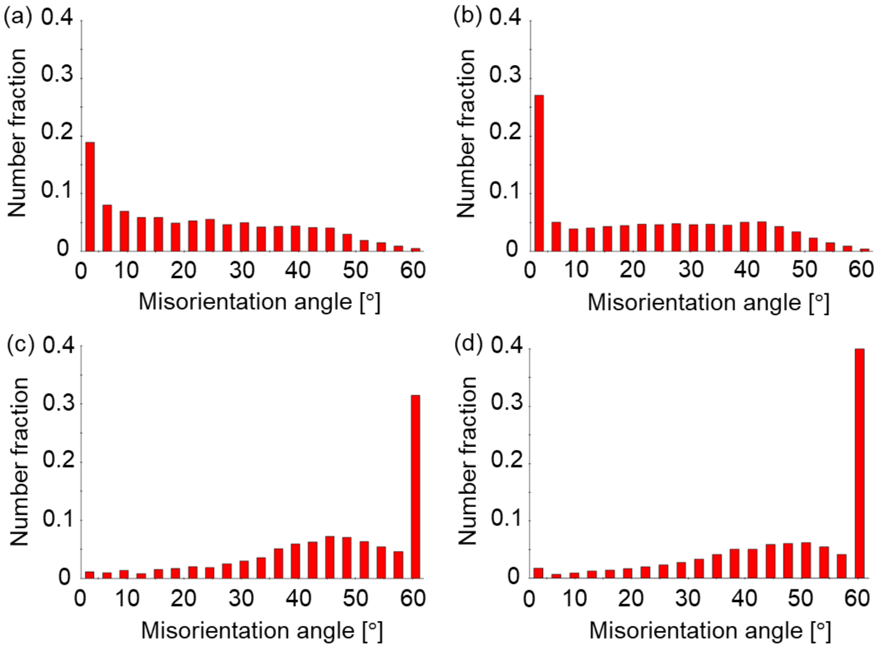

Fig. 3.3. Misorientation angle distribution for: (a) AM-L; (b) AM-H-HIP; (c) WR-L; (d) WR-H.

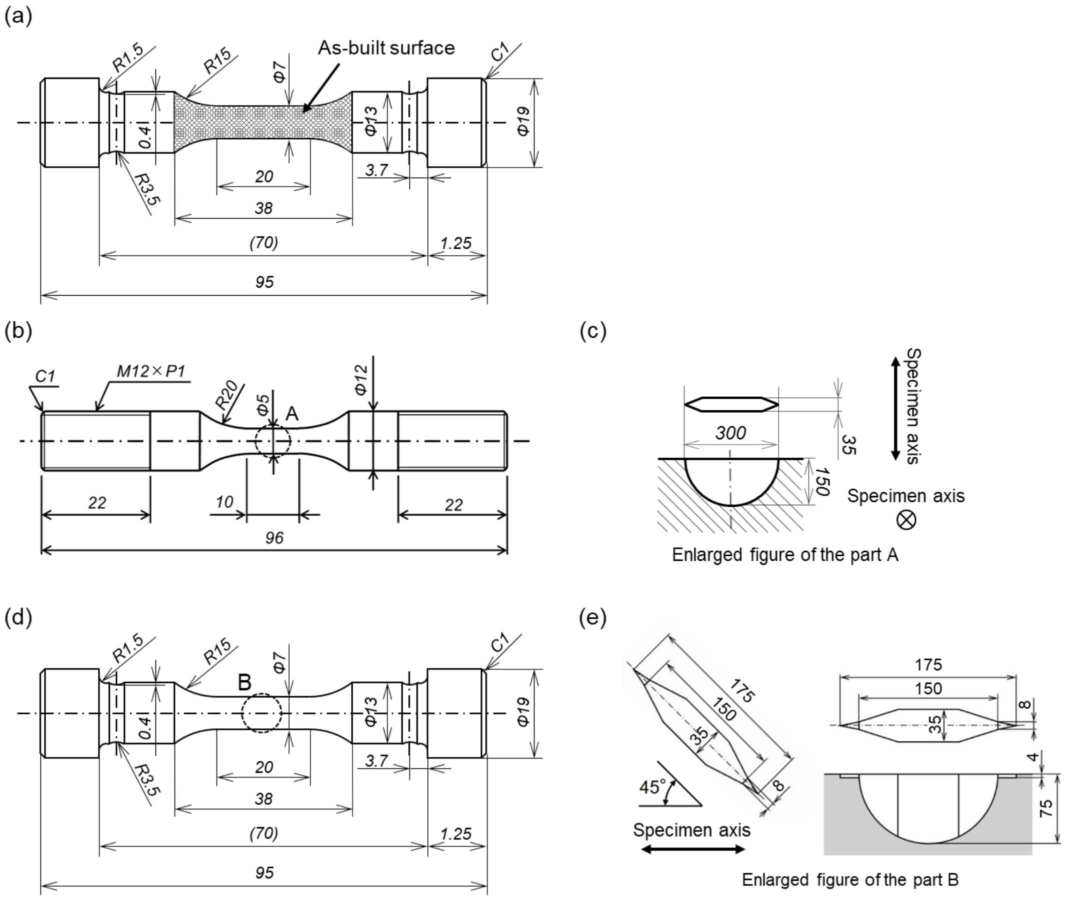

Fig. 3.4. Shapes and dimensions of: (a) as-built specimen for the push-pull fatigue tests (in mm); (b) EDM-notch specimen for the σ_a-increasing test (in mm); (c) small, semicircular EDM-notch (in μm); (d) EDM+FIB notch specimen for the push-pull fatigue tests (in mm); (e) small, semicircular EDM-notch with FIB slits inclined at 45° with respect to the specimen axis (in μm).

3.3 Results and discussion

3.3.1 Push-pull fatigue test results

Fig. 3.5 presents the *S-N* data for AM-H-HIP as obtained from push-pull fatigue tests using the as-built specimen. The fatigue test results for WR-H with EDM+FIB notches and WR-L with drill-holes are also presented in the figure. Despite the nearly identical defect size ($\sqrt{area}$ = 94 μm for defect in as-built specimen (*cf.* Fig. 3.8(a)), $\sqrt{area}$ = 84 μm for EDM+FIB notch, and $\sqrt{area}$ = 93 μm for drill-hole [22]), the fatigue limit of AM-H-HIP (*i.e.*, 220 MPa) was significantly inferior to those of WR-H (*i.e.*, 420 MPa) and WR-L (*i.e.*, 410 MPa), a similar phenomenon observed in the precedent chapter, suggesting the presence of intrinsic factors dominating the fatigue strength in this AM material other than defects, to be examined in the present and subsequent chapters. Fig. 3.6(a) shows the crack-length, $2a$, as a function of the number of cycles, N, in the σ_a-increasing test using an EDM-notch specimen of AM-H-HIP, where $2a$ is the total length of the crack including the notch-length, as illustrated in the figure. Crack-growth rate, $d(2a)/dN$, was extremely slow (less than 2×10^{-10} m/cycle) until σ_a reached 240 MPa, at which point $2a$ started increasing dramatically. Therefore, the fatigue limit of this specimen was determined to be 220 MPa. On the other hand, Fig. 3.6(b) shows the plastic replica observation of fatigue cracks generated from the notch-tip during the test. It should be mentioned that a small crack was initiated at 200 MPa and was finally arrested, even with the subsequent increase in stress amplitude up to 240 MPa. Moreover, another fatigue crack was generated and continued to propagate at a stress amplitude of 240 MPa. Similar to the experimental finding in Section 2.3.2 (*cf.* Fig. 2.10(a)), there might be various complex factors contributing to these results, including the interaction between adjacent cracks, the influence of local microstructures, and the potential presence of a coaxing effect. It is important to highlight that since the influence of each individual factor on the fatigue limit could not be elucidated in the present study, the determined fatigue limit in this test should be considered as an approximation.

Fig 3.7 showcases BSE images of the arrested crack at the fatigue limit and the propagating crack near the fatigue limit, observed in notched AM specimen of the σ_a-increasing test. The higher magnification view near the notch-tip revealed that the arrested crack propagated along the {111} slip plane, as indicated by solid white lines, and was finally arrested in the vicinity of GBs at the fatigue limit, indicated by dotted yellow lines (*cf*. Fig. 3.7(b)). This infers that the local shear stress ahead of the crack-tip is the primary crack driving-force in this material under fully-reversed, uniaxial cyclic-loading, identical to the results of AM-L. Accordingly, the fatigue limit of AM-H-HIP under push-pull loading was also presumed to be governed by the shear-mode crack-growth threshold, $\Delta K_{\tau th}$. In addition, the propagating fatigue crack emanating from the EDM-notch in AM-H-HIP proliferated along a direction close to the maximum shear-stress direction, with a slight deviation due to the grain orientations, as evidenced in Fig. 3.7(a), until it deflected the paths to the macroscopic Mode I direction.

On the other hand, in the case of AM-H-HIP, cracks were hardly observable on the specimen surface due to the rough surface and remnant powders. Therefore, the run-out specimen was tested again at a higher stress ratio, $R = 0.1$, to identify a fatal defect in the specimen. Fig. 3.8(a) displays the fracture surface of the specimen and Fig. 3.8(b) showcases the fracture initiation site with the effective defect size at the fracture origin as considering the interaction of un-melted powder and surface roughness [24] (*cf*., broken lines in Fig. 3.8(b)). When two small defects are adjacent within a critical length corresponding to the smaller defect size, fatigue crack coallescense would preferentially occur in the region between those defects due to the SIF elevation [25]. Therefore, effective defect size in the as-built specimen was measured by enveloping adjacent defects and the area between the defects [26,27]. Furthermore, in order to identify the crack arresting mode in this specimen, secondary cracks in a broken specimen were investigated. Fig. 3.9 presents a BSE image of an example of secondary cracks observed near the surface in the cross-section cut parallel to the axial direction of an as-built specimen, which was broken at a stress amplitude of 540 MPa. A small crack generated from the valley of the rough surface propagated obliquely with respect to the loading direction through a few grains along the {111} slip plane, indicating that the crack-growth was mainly driven by maximum shear stress. Given the similarity of the crack-growth behavior to that of small fatigue cracks observed in this study, it can be presumed that the secondary crack is a small fatigue crack generated during fatigue loading. Consequently, it was inferred that the fatigue limit of the as-built specimen is determined by the threshold condition of shear-mode crack growth.

3.3.2 Evaluation of the shear-mode, fatigue crack-growth threshold

The previous section revealed that the fatigue limit of AM-H-HIP is also the threshold condition of a shear-mode crack. Therefore, shear-mode fatigue crack-growth threshold in each test was estimated in a manner similar to the evaluation method for AM-L.

In the case of push-pull fatigue testing of the as-built specimen, the non-propagating crack was assumed to be lying on the maximum shear-stress plane based on the observation results of secondary cracks (*e.g.*, Fig. 3.9). Therefore, for the evaluation of shear-mode threshold SIF ranges, the following model proposed by Okazaki *et al.* [28] was applied.

$$\Delta K_{\tau\mathrm{th}} = 2\times 0.69(\sigma_\mathrm{w}/2)\sqrt{\pi\sqrt{area_\tau}} \tag{3.1}$$

where σ_w is the fatigue limit of push-pull fatigue tests and $\sqrt{area_\tau}$ is the square root of the area of the crack or defect projected onto the maximum shear-stress plane. The effective defect size at the fracture origin of the run-out as-built specimen (*cf.* Fig. 3.8(b)) was used for the estimation of threshold SIF ranges. Since an accurate shape of the defect enveloped by dotted yellow line is not unknown, it was assumed that the projected area of the defect onto the maximum shear-stress plane is the same as the effective defect size at the fracture origin due to the spherical shape of the un-melted powder. Consequently, $\Delta K_{\tau\mathrm{th}}$ = 2.6 MPa·m$^{1/2}$ was derived by inserting σ_w = 220 MPa (*cf.* Fig. 3.5) and $\sqrt{area_\tau}$ = 94 μm (*cf.* Fig. 3.8(b)) into Eq. (3.1).

On the other hand, regarding the push-pull fatigue test of the notched specimen (*i.e.*, the σ_a-increasing test), the arrested crack did not macroscopically lie on the maximum shear-stress plane, although it stopped propagating in shear-mode. As mentioned in the previous chapter, thin EDM-notch including the arrested crack under push-pull loading can almost be mechanically equivalent to a planar crack normal to the loading axis. Based on the elasticity solutions for the distribution of normal stress and shear stress in the vicinity of the crack-tip, the following relationship is obtained between the maximum Mode I SIF range and the maximum shear-mode SIF range under fully-reversed, push-pull loading:

$$\Delta K_{\mathrm{I}\theta\max} = 2.598\Delta K_{\tau\theta\max} \tag{2.8}$$

Here, $\Delta K_{\mathrm{I}\theta\max}$ can be calculated by using the formula proposed by Murakami [29]:

$$\Delta K_{\mathrm{I}\theta\max} = 2\times0.65\sigma_0\sqrt{\pi\sqrt{area}_{\mathrm{P}}} \tag{2.9}$$

where $\sqrt{area}_{\mathrm{P}}$ is the square root of the area of a crack or defect projected onto the principal stress plane. Using Eqs. (2.8) and (2.9) for AM-H-HIP, the $\Delta K_{\mathrm{I}\theta\max}$ = 7.0 MPa·m$^{1/2}$ was obtained from σ_{w} = 220 MPa and $\sqrt{area}_{\mathrm{P}}$ = 188 μm, yielding $\Delta K_{\tau\mathrm{th}}$ = 2.7 MPa·m$^{1/2}$.

The $\Delta K_{\tau\mathrm{th}}$ values gathered as a function of $\sqrt{area}$ (*i.e.*, $\sqrt{area}_{\tau}$ or $\sqrt{area}_{\mathrm{P}}$) are provided in Fig. 3.10. For comparison, the results of torsion and push-pull fatigue tests using AM and WR alloys [30,31] demonstrated in Chapter 2 are also plotted in the figure. It is noteworthy to mention that threshold values of all the AM materials obey the rule of $\Delta K_{\tau\mathrm{th}} \propto (\sqrt{area})^{1/3}$. Moreover, through the least squares fitting, the following relationship is gained within an almost 10% error band, which is consistent with the results of Chapter 2.

$$\Delta K_{\tau\mathrm{th}} = 0.50(\sqrt{area})^{1/3} \tag{2.11}$$

Given that two AM alloys examined in this study show nearly identical fatigue strength regardless of different process conditions and heat treatment routes, the influence of potential factors targeted in this chapter, *i.e.*, precipitates, grain size and residual stress seems to be minimal. In the subsequent section, the discussion will be made on the reason.

3.3.3 Influence of precipitates, grain size and residual stress on fatigue resistance

Firstly, with regard to hardening precipitates, fatigue crack-thresholds of Alloy 718 are reported to be closely related to the resistance of the precipitates against the dislocation motion which changes with the coarsening of the precipitates [5]. Moreover, micro-segregation of Nb elements along the interdendritic region (stemming from rapid solidification during the AM process) is supposed to inhibit the evolution of the precipitates, specifically γ'' phases, during solution and aging treatments since it promotes the formation of undesirable particles such as Nb-rich Laves phases and δ phases. Hence, it was expected that HIP treatment could improve the fatigue threshold of the AM alloy by homogenizing the microstructure. Nevertheless, no dramatic enhancement of the fatigue resistance of AM-H-HIP was observed as evidenced in Fig. 3.10. Therefore, to identify the link between precipitates (*i.e.*, γ'' phases) and poor, shear-mode, small fatigue-crack resistance in AM alloys, size and dispersion state of the precipitates in AM and WR samples were comparably investigated using the transmission electron microscope (TEM) technique.

TEM micrographs of AM-L and WR-H samples are respectively exhibited in Fig. 3.11(a) and (d). The local γ'' precipitate-free zones (PFZs) are prevalent in both samples along the boundaries of coarse particles. It is believed that these particles are Laves phases and δ phases, which led to the formation of PFZs by the depletion of Nb. For more precise observation of the γ'' phase morphology, TEM bright-field (BF) images for each sample are presented in Fig. 3.11(b), (c) and (e), revealing fine particles dispersed in the γ matrix. Contrary to our expectations, there was a minor difference in the dispersion state and size of γ'' phases, approximately 30 nm or less in size for all samples. Strictly speaking, the precipitate was coarse in the order of AM-H-HIP, WR-H and AM-L with average sizes of 26 nm, 23 nm and 21 nm, respectively. Hence, the TEM observation results infer no obvious correlation between the precipitation of the γ'' phase and the shear-mode crack-threshold.

Even though the comparative evaluation of the effect of precipitate sizes was not feasible in this study due to the close similarity in size of the materials, small fatigue crack-growth resistance is deemed to be minimally influenced by the different precipitate states for the following reason. It is acknowledged that the successive shearing of coherent hardening precipitates by moving dislocation pairs under cycling loading is the primary characteristic of slip deformation in this alloy. As depicted in Fig. 3.12 [32], such a dislocation-precipitate interaction would bring about the formation of precipitates-depleted zone and consequently, facilitate crack initiation within the region owing to diminished resistance to dislocation gliding [33–35]. After all, the depletion of shearable precipitates would be triggered in the crack-tip vicinity at an earlier stage of cyclic loading, resulting in equivalent shear-mode, small fatigue crack-growth resistance in these materials, regardless of the state of precipitate evolution. Indeed, the shear-mode thresholds of two types of WR Alloy 718 samples, *i.e.*, solution-treated with aging (WR-L) and without aging (WR-ST), were found to be nearly identical despite the different states of precipitates [3] as shown in Fig. 3.10, supporting the premise above.

Secondly, regarding the effects of δ phases and Laves phases on the fatigue strength of the alloy, a few researchers reported two opposing views as follows: (i) degradation of fatigue strength by the depletion of γ'' phases [7,8]; (ii) retardation of fatigue crack-propagation [6]. The impact of the former is thought to be trivial, due to the inability of hardening precipitates to resist fatigue, as mentioned earlier. Above all, if fatigue strength was influenced by δ phases and Laves phases, there should be a noticeable disparity in fatigue thresholds between AM-L and AM-H-HIP. On the other hand, the positive impact of the δ phases and Laves phases, *i.e.*, the retardation of fatigue cracks, could not be confirmed in the present study. This was due to the fact that, at the fatigue limit, most cracks were arrested in the vicinity of GBs, preferential sites for δ phases and Laves phases, thus rendering it impossible to evaluate their roles separately. Nevertheless, when compared to that of WR materials, the substantially inferior fatigue strength of AM-L with both δ phases and Laves phases within grain interiors, as well as along GBs, implies that these precipitates might play a minor role in the fatigue crack-arresting mechanism of this alloy.

Thirdly, the reason why the effect of grain size on the small fatigue crack-growth threshold was not observed in this study can be explained by a recent study conducted by Kevinsanny *et al*. [22], who performed the push-pull fatigue tests of WR alloys with fine-grained (WR-FG) and coarse-grained (WR-CG) microstructures. They demonstrated that fatigue strength evaluated by small, opening-mode fatigue threshold was nearly equivalent between WR-FG and WR-CG materials. Instead, grain size determines the initial defect size since a crack initiated in a grain can be regarded as an initial defect [36]. In other words, the larger grains, the larger the crack initiation size, which effect is expressed by the crack-size dependence of fatigue threshold. Furthermore, grain size determines the tolerable defect size of the alloy, *i.e.*, the fatigue limit of the alloy with coarser grains is less susceptible to defects, since defects smaller than the crack initiation size would be harmless to the fatigue limit. For example, from push-pull fatigue testing on coarse-grained AM Alloy 718, Kevinsanny *et al*. [37] revealed that the effect of surface roughness and porosities on the fatigue limit of the alloy was negligible, which was attributed to the relatively larger grain size than the process-induced defects. Accordingly, grain size is believed to contribute to both the initial defect size and the tolerable defect size.

Finally, a brief mention must be made on the influence of residual stress since as-built AM parts essentially involve local residual stresses due to non-uniform solidification rates and large thermal gradients [38,39]. This is known to be unfavorable to the fatigue strength by altering the mean stresses and effective load ratio during cyclic loading [40,41]. Indeed, numerous studies have demonstrated the significant impacts of residual stress on fatigue strength of various as-built AM materials such as Al alloy [42], Ti alloy [43], and stainless steel [44]. Notwithstanding, since our experimental materials underwent HIP or STA treatments after printing, the effect of residual stress was thought to have been sufficiently minimized. For example, Barros *et al*. [45] investigated the distribution of residual stresses in as-built and heat-treated AM Alloy 718 samples. The latter was solution-treated at 1065°C for 1 h, followed by a double aging process with identical conditions applied to our samples. Using the hole-drilling strain-gage method to measure the magnitude of residual stress, they discovered that the as-built specimen exhibited tensile residual stress ranging from half the yield strength to near the yield strength. However, the residual stress was significantly reduced after the STA heat treatment. Based on the results of the literature, the HIP condition of AM-H-HIP is supposed to be enough to eliminate the residual stress. Nevertheless, the fact that the threshold values of AM-H-HIP are apparently identical to those of AM-L implies that residual stress is not the dominating factor for the inferior fatigue resistance of both AM alloys in the present study.

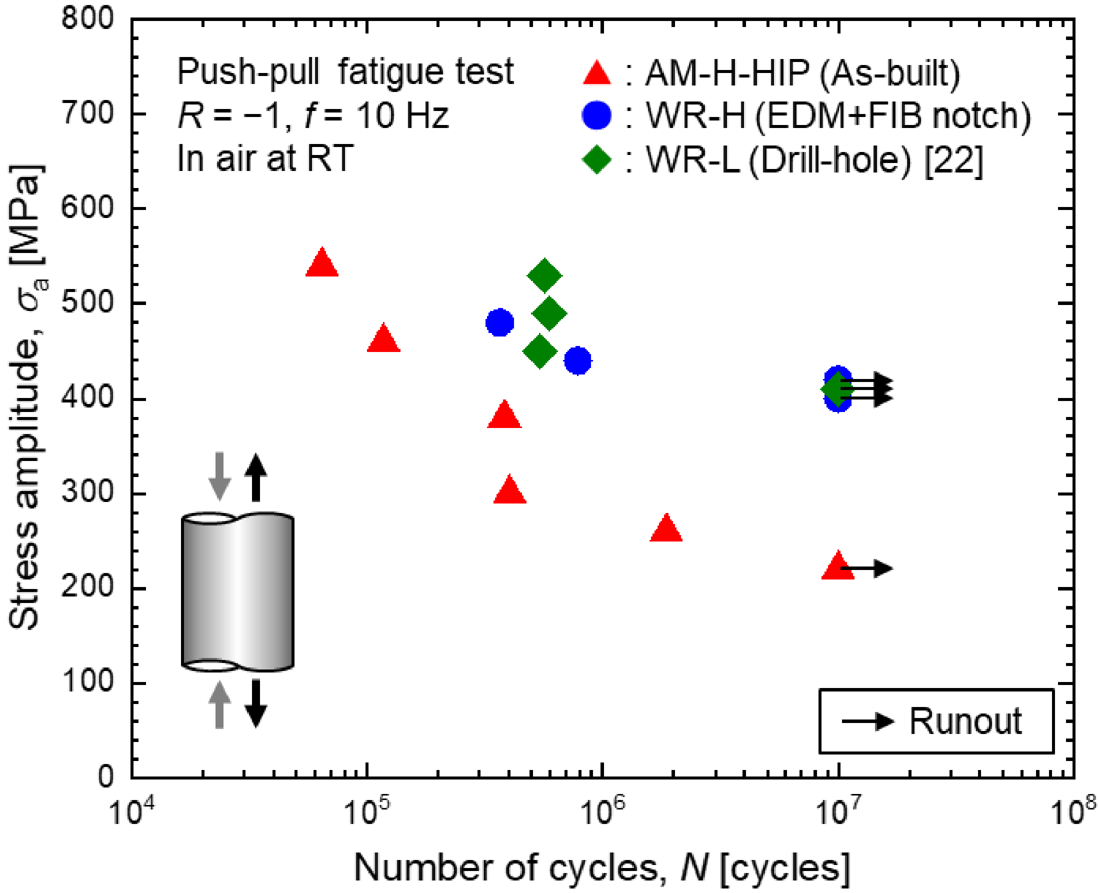

Fig. 3.5. *S-N* data obtained *via* push-pull fatigue tests.

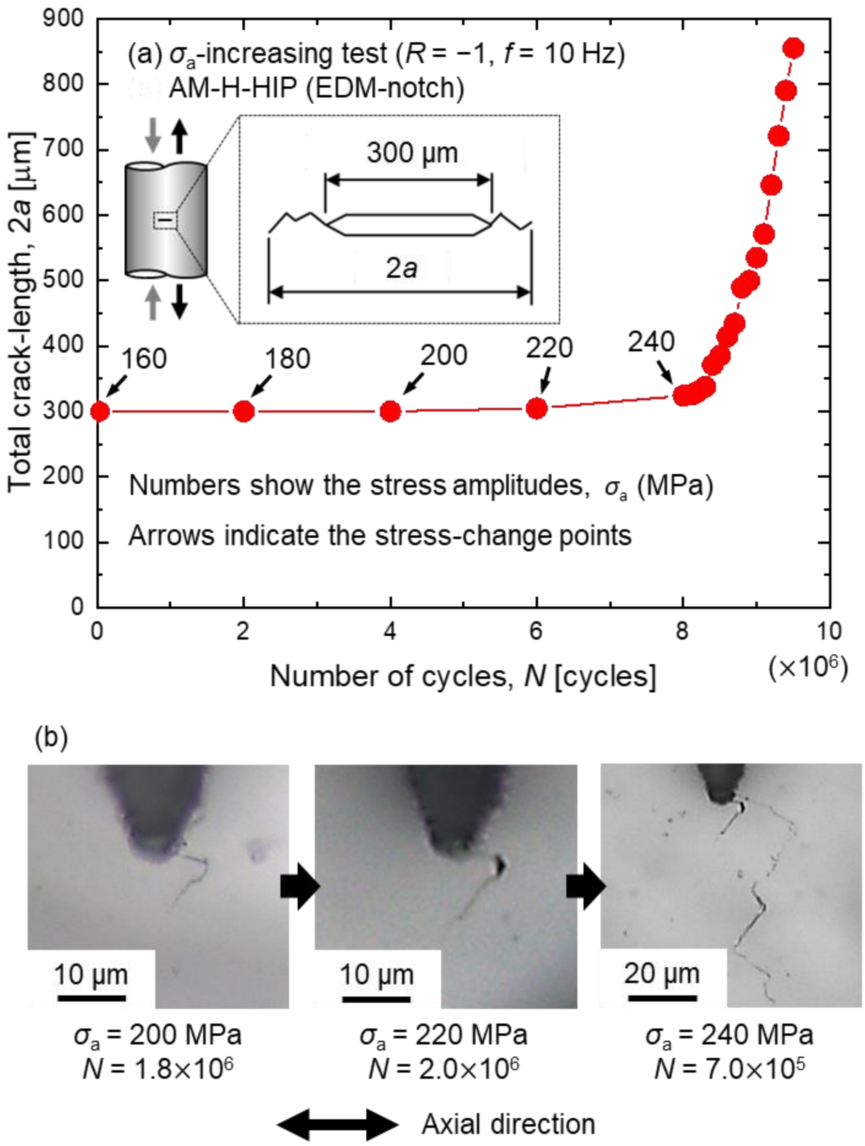

Fig. 3.6. (a) Crack-growth curve in the σ_a-increasing test using an EDM-notch specimen of AM-H-HIP; (b) plastic replica observation of non-propagating crack and propagating crack at the notch tip.

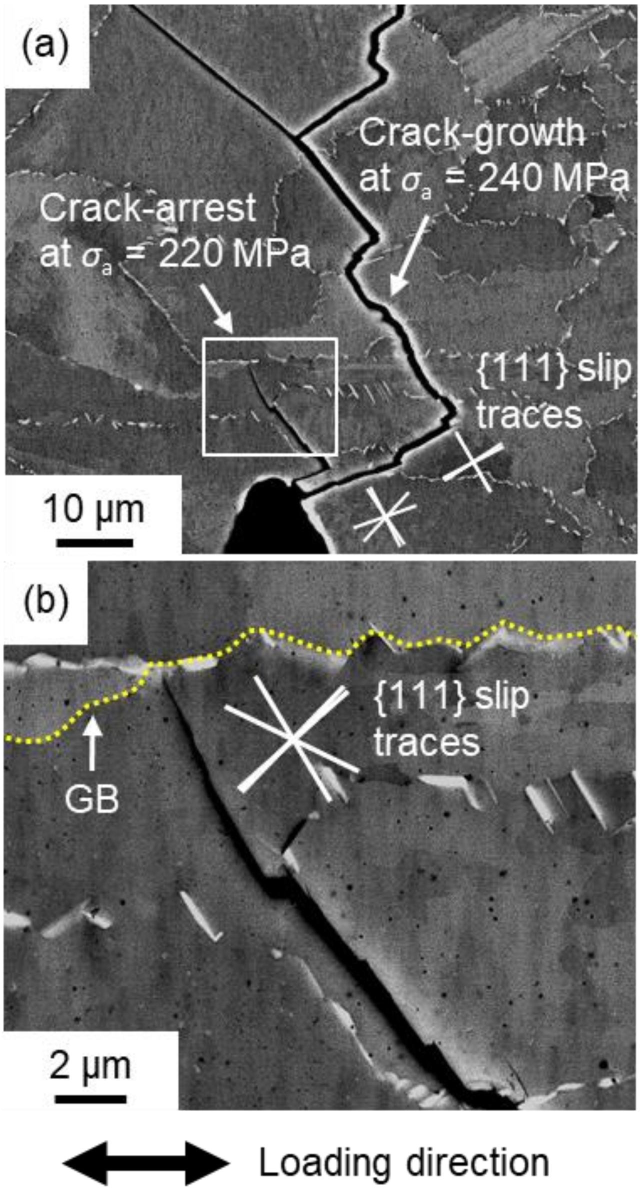

Fig. 3.7. (a) BSE image of fatigue crack emanating from EDM-notch under push-pull loading; (b) correspond to the region marked by white rectangle in (a).

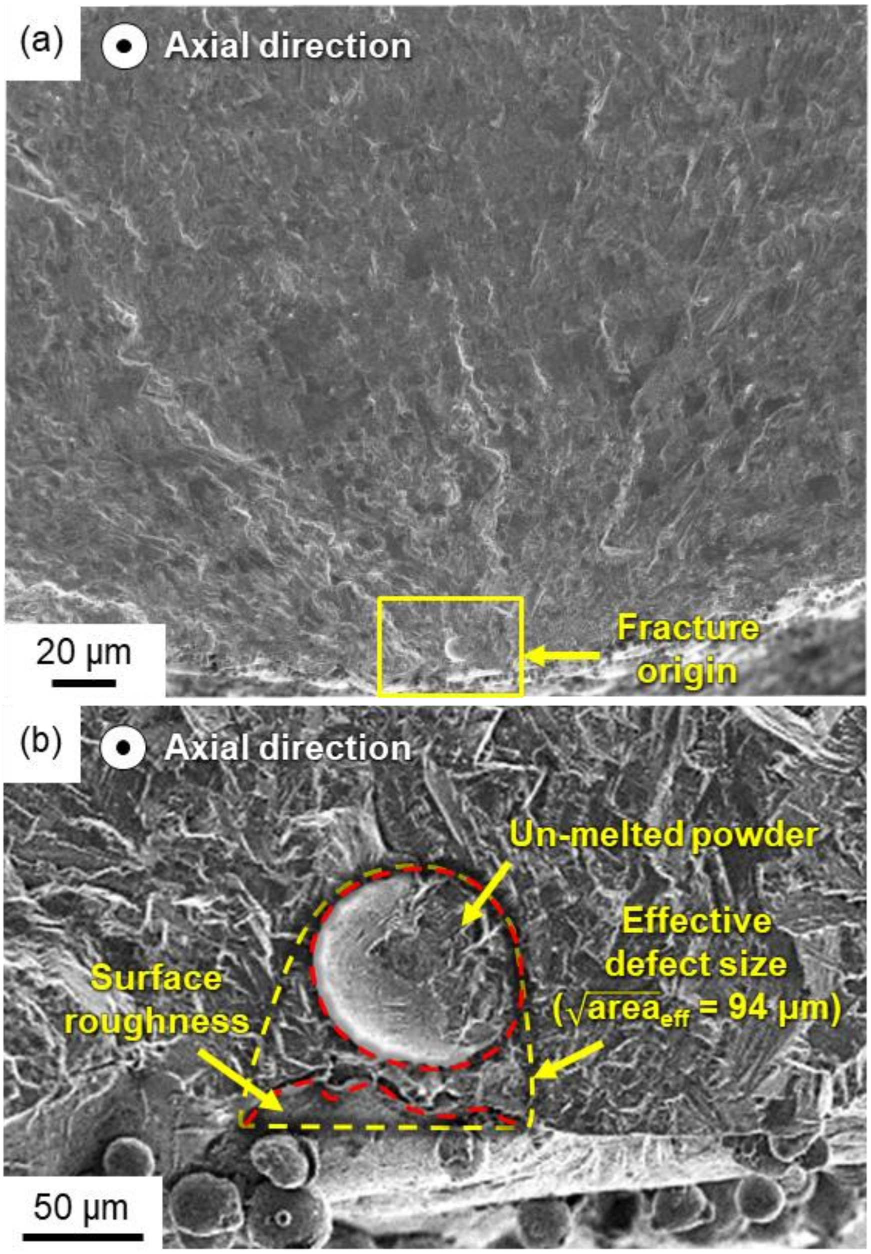

Fig. 3.8. (a) SEM image of the fracture surface of AM-H-HIP as-built run-out specimen with as-built condition tested at *R* of 0.1; (b) SEM image of the fracture origin in (a).

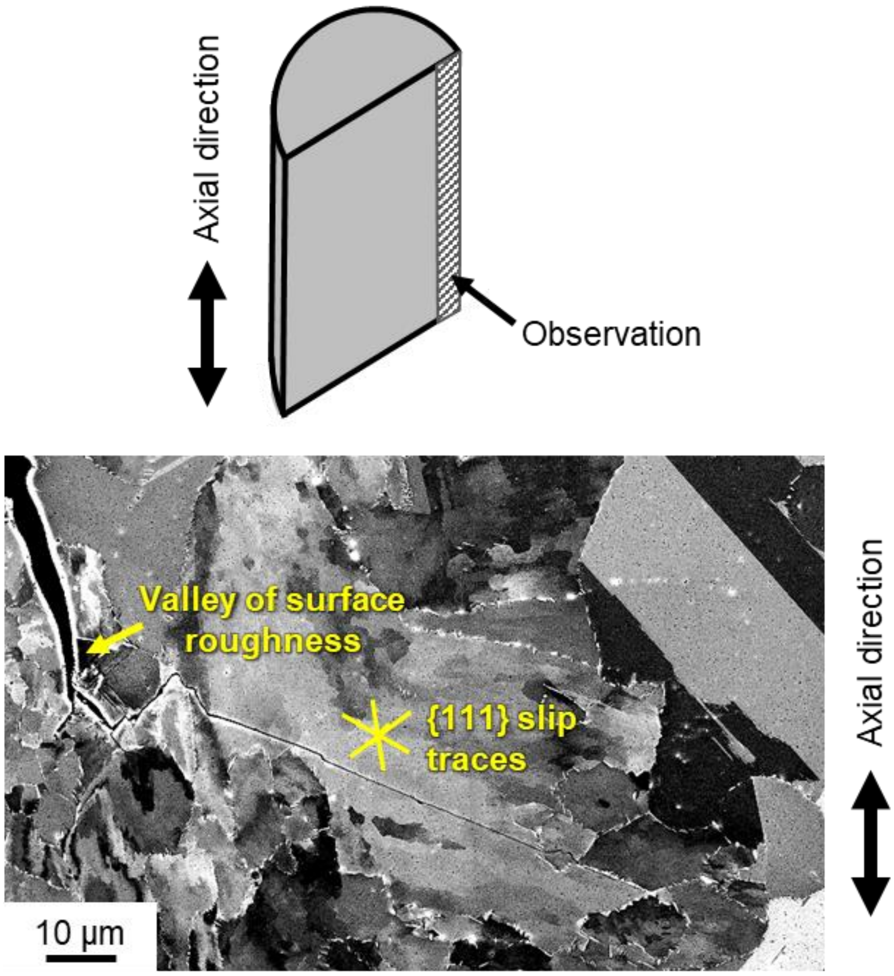

Fig. 3.9.BSE image of a secondary crack observed in AM-H-HIP as-built specimen broken at σ_a = 540 MPa.

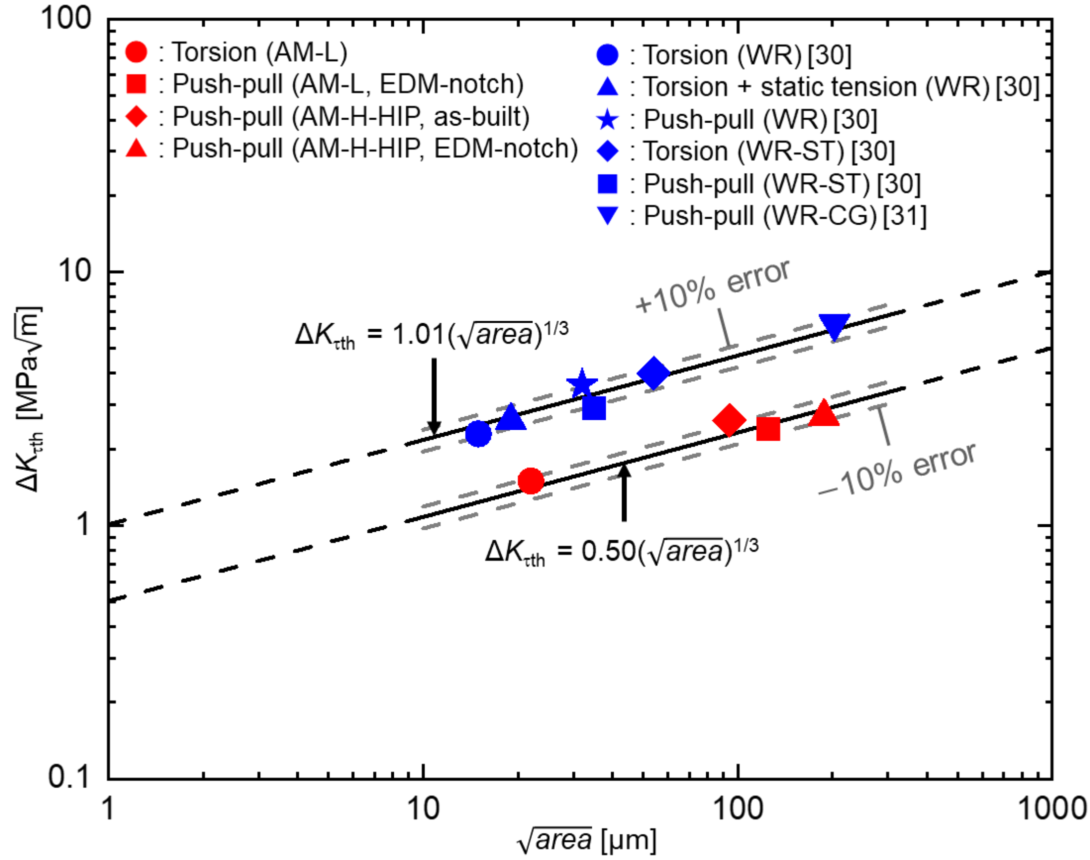

Fig. 3.10. $\Delta K_{\tau th}$ of AM and WR Alloy 718 as a function of $\sqrt{area}$. The regression line (solid black line) is defined using the least squares fitting for all experimental data.

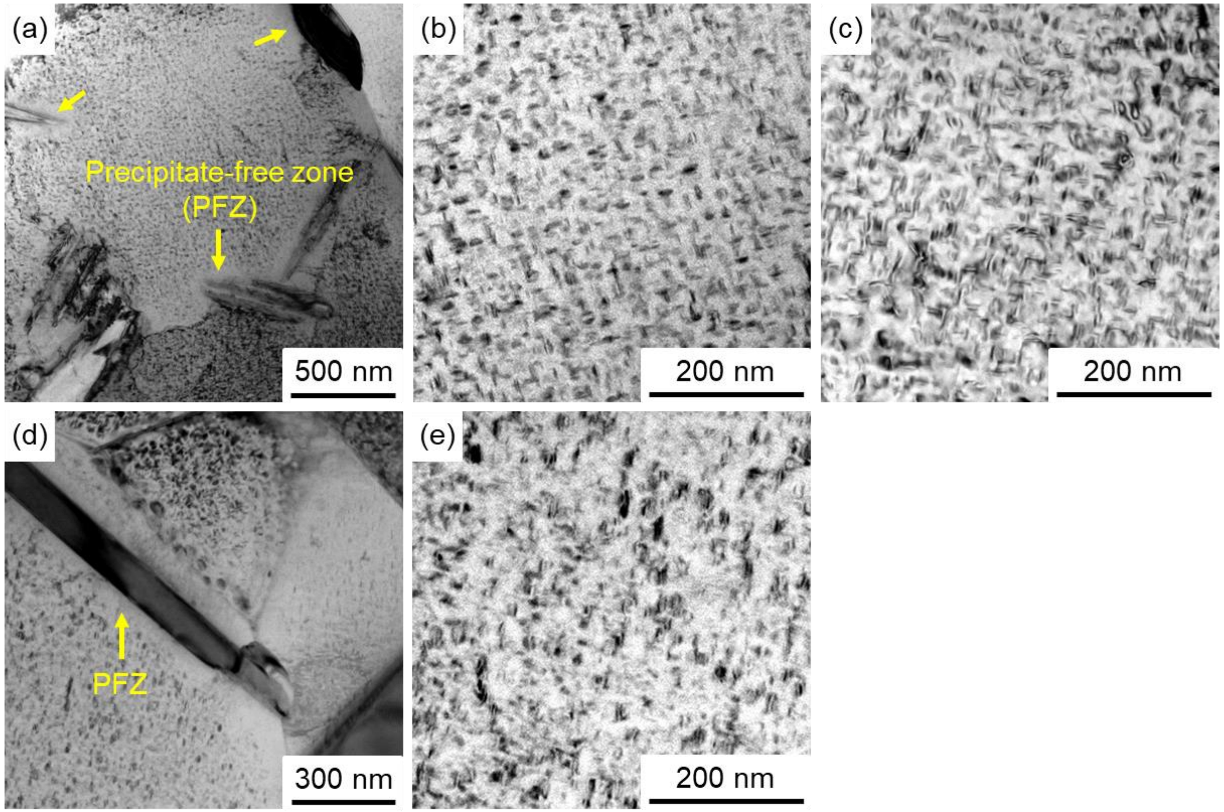

Fig. 3.11. γ'' phase observations *via* TEM: (a)(d) TEM micrographs of AM-L and WR-H; (b)(c)(e) BF images of AM-L, AM-H-HIP and WR-H.

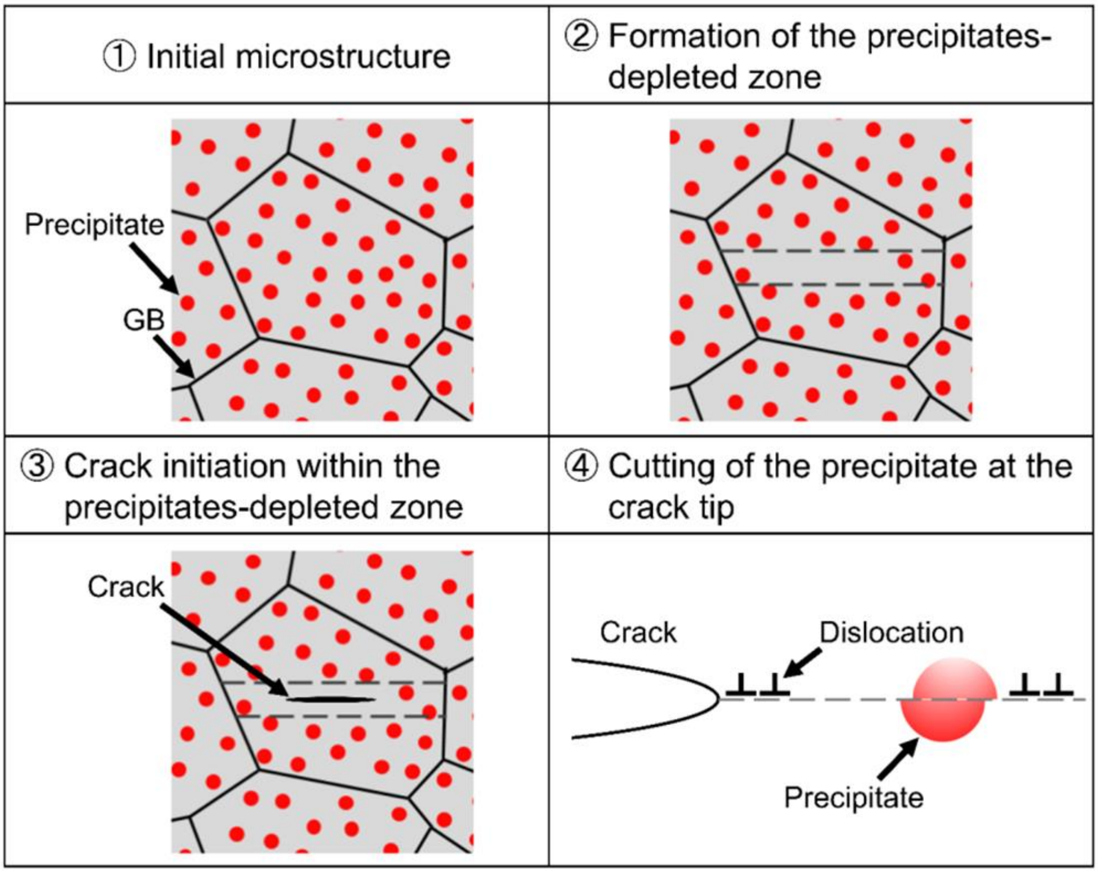

Fig. 3.12. A schematic illustration of the crack initiation within precipitate-depleted zone and successive shearing of precipitates at the crack tip under cyclic loading [32].

3.4 Conclusion

In this chapter, the determining factors for the inferior fatigue resistance of an additively-manufactured, Ni-based superalloy 718 (AM Alloy 718) were investigated with focus on the effects of precipitates, grain size and residual stress. To this end, AM Alloy 718 sample was manufactured by different processing condition (*i.e.*, higher energy density) and heat treatment route (*i.e.*, hot isostatic pressing before solution treatment and aging), as compared to those of the AM alloy investigated in Chapter 2. By performing push-pull fatigue tests, the fatigue threshold was evaluated, and the effects of the factors were discussed. The main conclusions are summarized as follows:

1. The AM sample produced in this chapter exhibited a relatively fine-grained microstructure in which intragranular Laves and δ phases were dissolved. However, a strong texture still remained, with only a negligible fraction of annealing twin boundaries.

2. Push-pull fatigue tests using specimens with as-built surface and a notched specimen with polished surface revealed that the fatigue limit of all the samples was the threshold condition of a shear-mode, small fatigue-crack propagation, similar to the findings in the previous chapter.

3. The shear-mode, fatigue-crack growth-threshold, $\Delta K_{\tau\mathrm{th}}$, was estimated in each case. As a result, the newly obtained relationship between the $\Delta K_{\tau\mathrm{th}}$ and defect size was also in accordance with the identical crack-size dependence expressed by $\Delta K_{\tau\mathrm{th}} = 0.50(\sqrt{area})^{1/3}$, despite different microstructures in AM materials.

4. The aforementioned experimental results imply that precipitates, grain size and residual stress are not dominating factors resulting in inferior fatigue resistance of AM alloys in this study. This premise was supported by further investigation on the size and dispersion state of hardening precipitates *via* transmission electron microscope, as well as a review of relevant literature.

References

[1] Kobayashi S, Hirata M, Tsurekawa S, Watanabe T. Grain boundary engineering for control of fatigue crack propagation in austenitic stainless steel. Procedia Eng 2011;10:112–7. https://doi.org/10.1016/j.proeng.2011.04.021.

[2] Schneider M, George EP, Manescau TJ, Záležák T, Hunfeld J, Dlouhý A, et al. Analysis of strengthening due to grain boundaries and annealing twin boundaries in the CrCoNi medium-entropy alloy. Int J Plast 2020;124:155–69. https://doi.org/10.1016/j.ijplas.2019.08.009.

[3] Tanaka Y, Okazaki S, Ogawa Y, Endo M, Matsunaga H. Inability of precipitation-hardening to improve the fatigue limit of Ni-based superalloy 718 through a perspective of shear-mode cracking threshold. Mater Lett 2020;277:128377. https://doi.org/10.1016/j.matlet.2020.128377.

[4] Nishikawa H, Furuya Y, Kitano H, Nakamura T, Kuwabara K, Kanegae Y, et al. In-situ observation of microstructurally small fatigue crack initiation and growth behaviors of additively-manufactured alloy 718. Mater Sci Eng A 2022;835:142682. https://doi.org/10.1016/j.msea.2022.142682.

[5] Deng H, Wang L, Liu Y, Song X, Meng F, Yu T. Fatigue crack propagation behavior of IN718 superalloy aged with temperature/stress coupled field. Int J Fatigue 2021;153. https://doi.org/10.1016/j.ijfatigue.2021.106514.

[6] Sui S, Chen J, Fan E, Yang H, Lin X, Huang W. The influence of Laves phases on the high-cycle fatigue behavior of laser additive manufactured Inconel 718. Mater Sci Eng A 2017;695:6–13. https://doi.org/10.1016/j.msea.2017.03.098.

[7] Gribbin S, Ghorbanpour S, Ferreri NC, Bicknell J, Tsukrov I, Knezevic M. Role of grain structure, grain boundaries, crystallographic texture, precipitates, and porosity on fatigue behavior of Inconel 718 at room and elevated temperatures. Mater Charact 2019;149:184–97. https://doi.org/10.1016/j.matchar.2019.01.028.

[8] Sivaprasad K, Raman SGS. Influence of magnetic arc oscillation and current pulsing on fatigue behavior of alloy 718 TIG weldments. Mater Sci Eng A 2007;448:120–7. https://doi.org/10.1016/j.msea.2006.10.048.

[9] Ghorbanpour S, Sahu S, Deshmukh K, Borisov E, Riemslag T, Reinton E, et al. Effect of microstructure induced anisotropy on fatigue behaviour of functionally graded Inconel 718 fabricated by additive manufacturing. Mater Charact 2021;179:111350. https://doi.org/10.1016/j.matchar.2021.111350.

[10] Boyd-Lee AD. Fatigue crack growth resistant microstructures in polycrystalline Ni-base superalloys for aeroengines. Int J Fatigue 1999;21:393–405. https://doi.org/10.1016/S0142-1123(98)00087-5.

[11] Konečná R, Kunz L, Nicoletto G, Bača A. Long fatigue crack growth in Inconel 718 produced by selective laser melting. Int J Fatigue 2016;92:499–506. https://doi.org/10.1016/j.ijfatigue.2016.03.012.

[12] Xiao L, Chen DL, Chaturvedi MC. Effect of boron on the low-cycle fatigue behavior and deformation structure of INCONEL 718 at 650 °C. Metall Mater Trans A Phys Metall Mater Sci 2004;35 A:3477–87. https://doi.org/10.1007/s11661-004-0185-6.

[13] Xiao L, Chen DL, Chaturvedi MC. Effect of boron on fatigue crack growth behavior in superalloy IN 718 at RT and 650 °C. Mater Sci Eng A 2006;428:1–11. https://doi.org/10.1016/j.msea.2005.08.206.

[14] Pang HT, Reed PAS. Fatigue crack initiation and short crack growth in nickel-base turbine disc alloys - The effects of microstructure and operating parameters. Int J Fatigue 2003;25:1089–99. https://doi.org/10.1016/S0142-1123(03)00146-4.

[15] Gray GT, Williams JC, Thompson AW. Roughness-Induced Crack Closure: An Explanation for Microstructurally Sensitive Fatigue Crack Growth. Metall Trans A 1983;14:421–33. https://doi.org/10.1007/BF02644220.

[16] Padula SA, Shyam A, Ritchie RO, Milligan WW. High frequency fatigue crack propagation behavior of a nickel-base turbine disk alloy. Int J Fatigue 1999;21:725–31. https://doi.org/10.1016/S0142-1123(99)00036-5.

[17] Boyd-Lee A, King JE. SHORT FATIGUE CRACK PATH DETERMINANTS IN POLYCRYSTALLINE Ni-BASE SUPERALLOYS. Fatigue Fract Eng Mater Struct 1994;17:1–14. https://doi.org/10.1111/j.1460-2695.1994.tb00768.x.

[18] Antolovich SD. Microstructural aspects of fatigue in Ni-base superalloys. Philos Trans R Soc A Math Phys Eng Sci 2015;373. https://doi.org/10.1098/rsta.2014.0128.

[19] Suresh S, Ritchie RO. Propagation of short fatigue cracks. Int Met Rev 1984;29:445–73. https://doi.org/10.1179/imtr.1984.29.1.445.

[20] Nguyen QB, Luu DN, Nai SML, Zhu Z, Chen Z, Wei J. The role of powder layer thickness on the quality of SLM printed parts. Arch Civ Mech Eng 2018;18:948–55. https://doi.org/10.1016/j.acme.2018.01.015.

[21] Ma M, Wang Z, Zeng X. Effect of energy input on microstructural evolution of direct laser fabricated IN718 alloy. Mater Charact 2015;106:420–7. https://doi.org/10.1016/j.matchar.2015.06.027.

[22] Kevinsanny, Okazaki S, Takakuwa O, Ogawa Y, Okita K, Funakoshi Y, et al. Effect of defects on the fatigue limit of Ni-based superalloy 718 with different grain sizes. Fatigue Fract Eng Mater Struct 2019;42:1203–13. https://doi.org/10.1111/ffe.12989.

[23] Lorenzino P, Okazaki S, Matsunaga H, Murakami Y. Effect of small defect orientation on fatigue limit of carbon steels. Fatigue Fract Eng Mater Struct 2015;38:1076–86. https://doi.org/10.1111/ffe.12321.

[24] Murakami Y, Nemat-Nasser S. Growth and stability of interacting surface flaws of arbitrary shape. Eng Fract Mech 1983;17:193–210.

https://doi.org/10.1016/0013-7944(83)90027-9.

[25] Åman M, Wada K, Matsunaga H, Remes H, Marquis G. The influence of interacting small defects on the fatigue limits of a pure iron and a bearing steel. Int J Fatigue 2020;135. https://doi.org/10.1016/j.ijfatigue.2020.105560.

[26] Yamashita Y, Murakami T, Mihara R, Okada M, Murakami Y. Defect analysis and fatigue design basis for Ni-based superalloy 718 manufactured by selective laser melting. Int J Fatigue 2018;117:485–95. https://doi.org/10.1016/j.ijfatigue.2018.08.002.

[27] Masuo H, Tanaka Y, Morokoshi S, Yagura H, Uchida T, Yamamoto Y, et al. Influence of defects, surface roughness and HIP on the fatigue strength of Ti-6Al-4V manufactured by additive manufacturing. Int J Fatigue 2018;117:163–79. https://doi.org/10.1016/j.ijfatigue.2018.07.020.

[28] Okazaki S, Matsunaga H, Ueda T, Komata H, Endo M. A practical expression for evaluating the small shear-mode fatigue crack threshold in bearing steel. Theor Appl Fract Mech 2014;73:161–9. https://doi.org/10.1016/j.tafmec.2014.07.016.

[29] Murakami Y. Analysis of stress intensity factors of modes I, II and III for inclined surface cracks of arbitrary shape. Eng Fract Mech 1985;22:101–14. https://doi.org/10.1016/0013-7944(85)90163-8.

[30] Tanaka Y, Okazaki S, Ogawa Y, Endo M, Matsunaga H. Fatigue limit of Ni-based superalloy 718 relative to the shear-mode crack-growth threshold: A quantitative evaluation considering the influence of crack-opening and -closing stresses. Int J Fatigue 2021;148:106228. https://doi.org/10.1016/j.ijfatigue.2021.106228.

[31] Kevinsanny. Effect of defects and hydrogen on the fatigue limit properties of forged and additive manufactured Ni-based superalloy 718. Master Thesis, Kyushu University, 2019.

[32] Tanaka Y. A study on the quantitative evaluation of the effect of crack-face interference on fatigue strength and shear-mode fatigue crack-growth threshold of Ni-based superalloy 718. Doctoral Thesis, Kyushu University, 2021.

[33] Fournier D, Pineau A. Low cycle fatigue behavior of inconel 718 at 298 K and 823 K. Metall Trans A 1977;8:1095–105. https://doi.org/10.1007/BF02667395.

[34] Worthem DW, Robertson IM, Leckie FA, Socie DF, Altstetter CJ. Inhomogeneous deformation in INCONEL 718 during monotonic and cyclic loadings. Metall Trans A, Phys Metall Mater Sci 1990;21 A:3215–20. https://doi.org/10.1007/BF02647316.

[35] Xiao L, Chen DL, Chaturvedi MC. Cyclic deformation mechanisms of precipitation-hardened Inconel 718 superalloy. Mater Sci Eng A 2008;483–484:369–72. https://doi.org/10.1016/j.msea.2006.10.181.

[36] Hamada S, Sasaki D, Ueda M, Noguchi H. Fatigue limit evaluation considering

crack initiation for lamellar pearlitic steel. Procedia Eng 2011;10:1467–72. https://doi.org/10.1016/j.proeng.2011.04.245.

[37] Kevinsanny, Okazaki S, Takakuwa O, Ogawa Y, Funakoshi Y, Kawashima H, et al. Defect tolerance and hydrogen susceptibility of the fatigue limit of an additively manufactured Ni-based superalloy 718. Int J Fatigue 2020;139:105740. https://doi.org/10.1016/j.ijfatigue.2020.105740.

[38] Bartlett JL, Li X. An overview of residual stresses in metal powder bed fusion. Addit Manuf 2019;27:131–49. https://doi.org/10.1016/j.addma.2019.02.020.

[39] Guo C, Li G, Li S, Hu X, Lu H, Li X, et al. Additive manufacturing of Ni-based superalloys: Residual stress, mechanisms of crack formation and strategies for crack inhibition. Nano Mater Sci 2022. https://doi.org/10.1016/j.nanoms.2022.08.001.

[40] Schneller W, Leitner M, Pomberger S, Springer S, Beter F, Grün F. Effect of post treatment on the microstructure, surface roughness and residual stress regarding the fatigue strength of selectively laser melted AlSi10Mg structures. J Manuf Mater Process 2019;3. https://doi.org/10.3390/jmmp3040089.

[41] Beretta S, Gargourimotlagh M, Foletti S, du Plessis A, Riccio M. Fatigue strength assessment of “as built” AlSi10Mg manufactured by SLM with different build orientations. Int J Fatigue 2020;139:105737. https://doi.org/10.1016/j.ijfatigue.2020.105737.

[42] Maskery I, Aboulkhair NT, Tuck C, Wildman RD, Ashcroft IA, Everitt NM, et al. Fatigue performance enhancement of selectively laser melted aluminium alloy by heat treatment. Proc - 26th Annu Int Solid Free Fabr Symp - An Addit Manuf Conf SFF 2015 2020:1017–25.

[43] Hrabe N, Gnäupel-Herold T, Quinn T. Fatigue properties of a titanium alloy (Ti–6Al–4V) fabricated via electron beam melting (EBM): Effects of internal defects and residual stress. Int J Fatigue 2017;94:202–10. https://doi.org/10.1016/j.ijfatigue.2016.04.022.

[44] Lai W-J, Ojha A, Li Z, Engler-Pinto C, Su X. Effect of residual stress on fatigue strength of 316L stainless steel produced by laser powder bed fusion process. Prog Addit Manuf 2021:1–9.

[45] Barros R, Silva FJG, Gouveia RM, Saboori A, Marchese G, Biamino S, et al. Laser powder bed fusion of inconel 718: Residual stress analysis before and after heat treatment. Metals (Basel) 2019;9. https://doi.org/10.3390/met9121290.

4. Dominant factors for inferior fatigue resistance of AM Alloy 718−Part 2: Influence of crystallographic texture and annealing twin boundary

4.1 Introduction

In the last chapter, it was revealed that AM-H-HIP sample fabricated under process and heat treatment conditions different from those of AM-L sample also has significantly lower small, fatigue crack-growth resistance than WR materials. A comparison of the microstructural characteristics of all experimental materials investigated in this study is presented in Fig. 4.1. Given that dissimilar status of precipitates and grain size, along with residual stress were not critical factors for poor fatigue resistance of AM alloys, the subsequent focus should be on the crystallographic texture and annealing twin boundaries (ATBs), which are the most significant distinguishing factors between AM and WR materials.

The strong crystallographic texture of AM alloys results in a higher prevalence of low-angle grain boundaries (LAGBs) in their microstructures compared to WR alloys. Generally, it is believed that LAGBs have lower resistance to crack propagation across GBs while high angle grain boundaries (HAGBs) provide larger blocking effect on crack penetration through GBs, leading to the crack arresting [1]. In addition, it is observed that WR matrix has a large fraction of ATBs associated with the misorientation angle of 60°, which are also thought to enhance the resistance to slip transmission [2]. Hence, lower fatigue resistance in AM samples would be expected due to the weaker barriers that can resist fatigue cracking, being supported by the study of Nishikawa *et al*. [3] which demonstrated higher small fatigue crack-growth rates of AM Alloy 718 than WR alloy at an early crack propagation stage due to strong texture of AM microstructures. Nonetheless, the relationship between these boundaries and small, fatigue crack-growth threshold has not been fully understood yet.

In this context, the present chapter examines the effects of crystallographic texture and ATBs on small fatigue resistance, with the objective of elucidating the dominant factor for inferior fatigue threshold of AM alloys. Fatigue tests were additionally conducted to obtain cracks that propagate over a few grains in both AM and WR alloys. The small-crack behaviors at/near the threshold condition were primarily interpreted with respect to geometric relationship between crack-planes in neighboring grains.

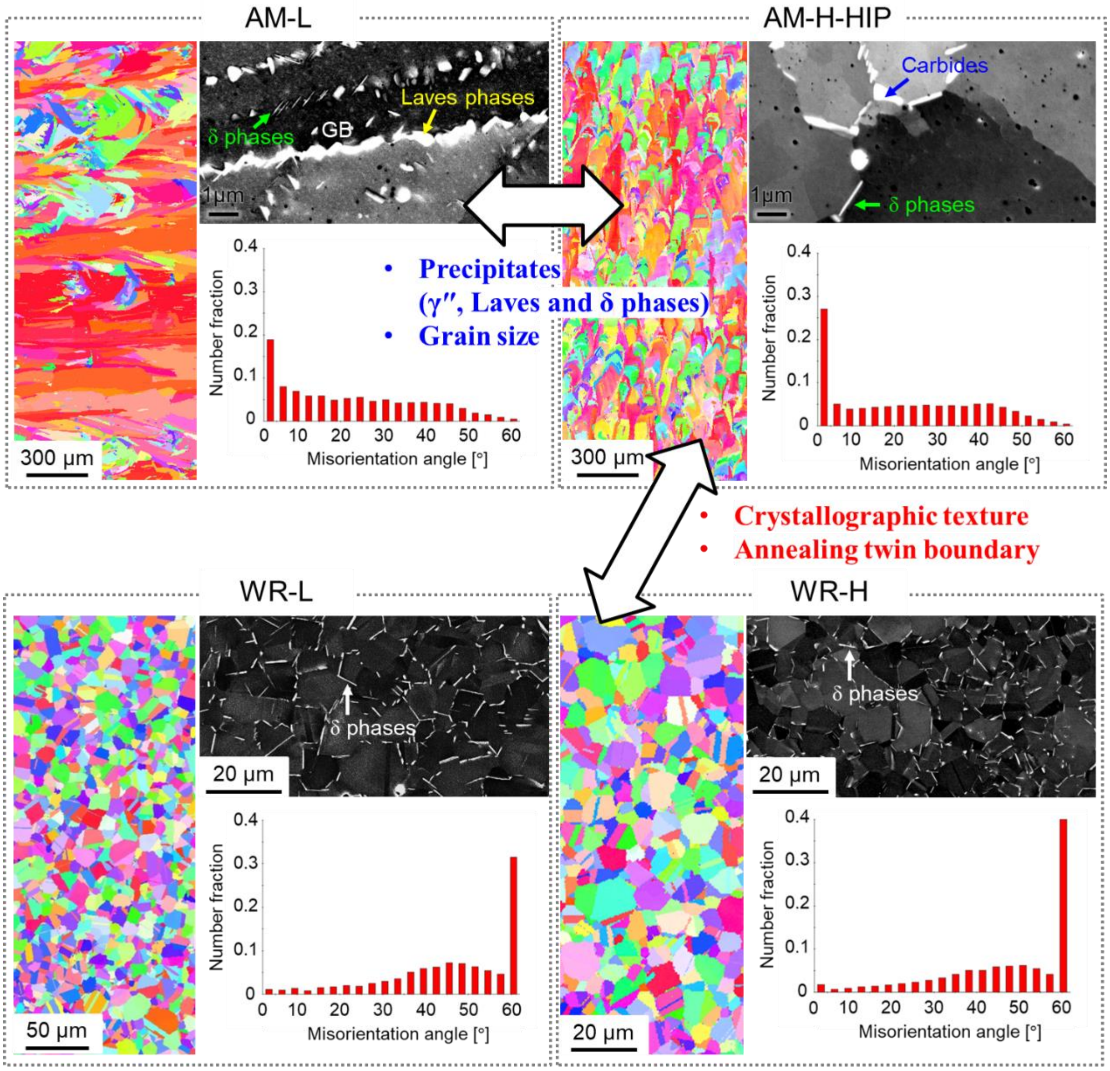

Fig. 4.1. Comparison of microstructural characteristics of all experimental materials.

4.2 Experimental methods

In order to facilitate a comparative discussion on the small fatigue-crack behavior between AM and WR alloys near the threshold stress, an additional push-pull fatigue test using the WR-L specimen with a drill-hole ($\sqrt{area}$ = 94 μm) was performed in a manner similar to the σ_a-increasing test of Chapter 3, *i.e.*, the normal-stress amplitude was gradually increased every 2×10^6 cycles in steps of 20 MPa from the predicted fatigue limit. The shapes and dimensions of the specimen and the drill-hole, shown in Fig. 4.2(a) and (b), were determined based on the study of Kevinsanny *et al.* [4], in which non-propagating cracks emanating from a drill-hole grew in a direction closely aligned with the maximum-shear-stress direction under push-pull loading before being arrested. In addition, it is noted that the propagating cracks obtained by push-pull fatigue tests of AM-L (*cf.* Fig. 2.10(a)) and AM-H-HIP (*cf.* Fig. 3.7(a)) in precedent chapters were also referenced. In addition, a specimen with a semicircular EDM-notch of AM-L was manufactured for the torsional fatigue test (*cf.* Fig. 4.2(c) and (d)). The specimen axis was parallel to the BD. Torsional fatigue testing was executed with a resonance fatigue-testing machine, operated at a stress ratio of −1 and a test frequency of 50 Hz. It should be noted that the test was also conducted by gradually increasing the shear-stress amplitude every 1×10^7 cycles in steps of 10 MPa from an initial value inferior to the fatigue limit. All of the specimen surfaces were polished with emery papers, followed by buffing with a diamond paste. The experiments were performed in ambient air at room temperature, with the tests being periodically halted to examine the fatigue crack-growth using the plastic replica method.

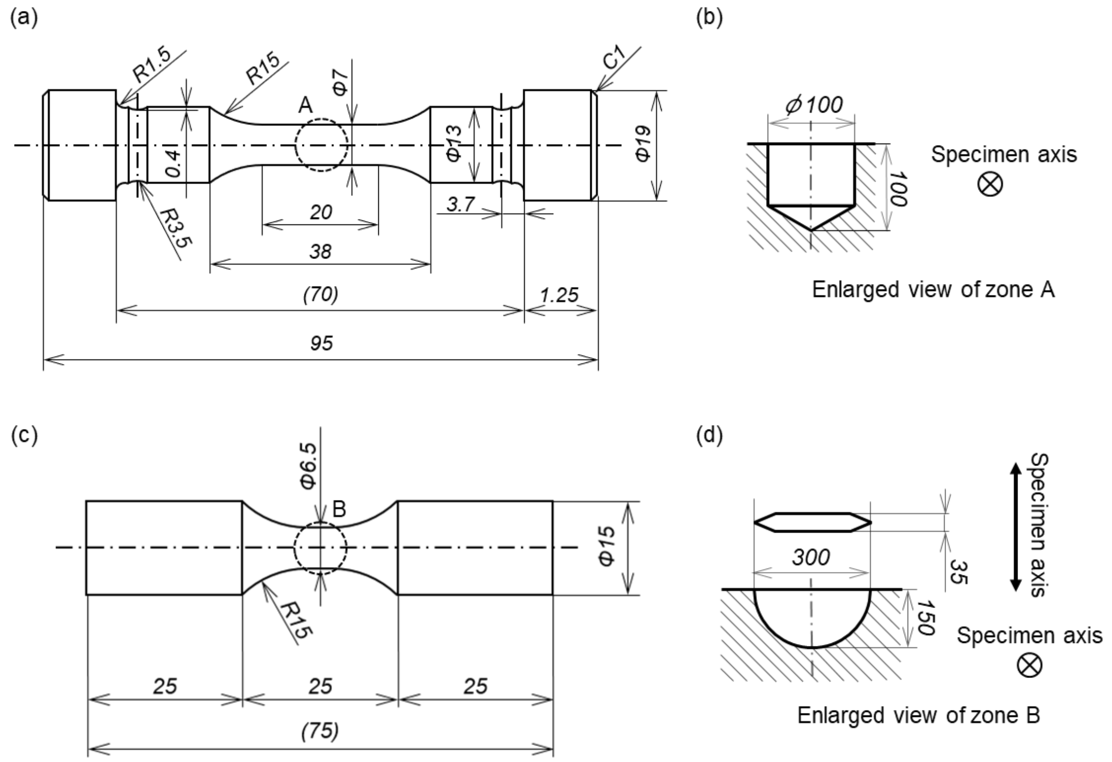

Fig. 4.2. Shapes and dimensions of: (a) drill-hole specimen for the push-pull fatigue test (in mm); (b) small, drill-hole (in μm); (c) EDM-notch specimen for the torsional fatigue test (in mm); (d) small, semicircular EDM-notch (in μm).

4.3 Results and discussion

4.3.1 Push-pull fatigue test results

Firstly, the effect of crystallographic texture on the fatigue resistance under push-pull fatigue loading was investigated due to the relatively more abundant experimental data. Fig. 4.3 shows small, crack-growth behaviors observed in EDM-notch specimen of AM-H-HIP and drill-hole specimen of WR-L near the threshold condition. Although cracks emanating from artificial defects appear to grow in Mode I macroscopically, cracks proliferated along the slip planes, as indicated by solid white lines, at an early stage of propagation within a few grains. Considering that crystallographic, small fatigue-cracking was pronounced in both materials, the influence of GB misorientation should be crucial to fatigue resistance as mentioned in the introductory section. According to Zhai *et al.* [5], two geometric parameters of crack-planes between neighboring grains, *i.e.*, the twist angle and the tilt angle, should be taken into account to evaluate GB resistance to crystallographic cracking.

As shown in Fig. 4.4, the twist angle (α) defines the intersection angle of the two crack-planes on the GB plane, with the tilt angle (β) associated with an angle between traces of crack-planes on the sample surface. The "CD" and "LD" in Fig. 4.4 indicate crack-growth direction and loading direction, respectively. Note that the GB plane was assumed to be perpendicular to the CD for simplification. When crystallographic cracks propagate across GBs, they need to change the slip plane so as to be favorable to continuous crack extension. The process requires a certain energy to fracture the hatched area in Fig. 4.4, dependent upon the twist angle. Hence, the twist angle can contribute primary resistance to the crack-growth along slip planes, while the tilt angle reduces the effective crack-growth driving force (*i.e.*, crack-tip shielding effect). Therefore, these geometric parameters were investigated along the paths of all cracks generated in the AM-L, AM-H-HIP and WR-L specimens for the push-pull fatigue tests.

Based on the grain orientation obtained from the EBSD, the twist angle and tilt angle distribution of each sample are plotted in Fig. 4.5(a) and (b), respectively. The most distinct feature in Fig. 4.5 is that the calculated values of the twist angle were significantly lower in the AM specimens than in the WR one. Twist angles in the WR specimen were randomly distributed from 15° to 78° with an average value of 43°, whereas those of the AM specimens were distributed up to 30°, with average values of 11° in AM-L and 12° in AM-H-HIP. Furthermore, with respect to the distribution of tilt angles, large scatters were observed in all of the materials without any significant material dependence. These results infer that the twist angle plays a major role in the fatigue crack-arresting mechanism in Alloy 718 and that the tilt angle is associated with a secondary role, captured in earlier experimental studies [6,7] and verified using the crystal plasticity extended finite element method [8].

Fig. 4.6 exhibits SEM images and IPF maps associated with the crack generated in the AM-H-HIP specimen (*cf.* Fig. 4.6(b) and (d)), as well as the crack that initiated from the drill-hole of the WR-L sample, at/near the threshold condition. The final stress amplitude for the AM and WR specimen was 240 MPa and 490 MPa, respectively. Both cracks propagated along the {111} slip planes in a crystallographic manner over a few grains before they stopped propagating. The featured grains are labelled, with an annealing twin (AT) in the WR sample denoted as AT1. The calculated twist angles (α) and tilt angles (β), along with the maximum Schmid factors (SFs) for each {111} slip plane are listed in Table 4.1. It must be pointed out that the active slip systems (*i.e.*, crack-planes) adjacent to GBs have been highlighted using bold font, while the primary slip systems associated with the highest SF have been underlined. Accordingly, the underlined bold font corresponds to the primary slip plane facilitated for crack propagation.

It is noteworthy that the precondition for crack-growth across GBs in AM-H-HIP was the presence of favorable slip planes, not only with high SFs, but also with strong compatibility (low twist/tilt angles) in an adjacent grain. For example, the (111) and $(\bar{1}11)$ planes in Grain 3 bore identical SF values, but the crack that propagated along the $(\bar{1}11)$ plane in Grain 3 possessed an advantageous geometrical relationship with the $(\bar{1}11)$ plane in Grain 2. Furthermore, the low twist angle between the $(\bar{1}11)$ plane in Grain 2 and the $(\bar{1}11)$ plane in Grain 1 appeared to facilitate the fatigue cracking along the $(\bar{1}11)$ slip plane in Grain 2, despite the similar tilt angle and SF values of the $(1\bar{1}1)$ and $(\bar{1}11)$ planes in Grain 2. Moreover, all of the twist angles in Grain 4 with respect to Grain 3 were relatively higher than those in other cracked grains of the AM sample, a plausible reason for crack-arrest in the vicinity of the GB between Grains 3 and 4. If the tilt angle was the most critical factor, the crack should have propagated along the $(1\bar{1}1)$ plane in Grain 4 with the highest SF and the lowest tilt angle. This suggests that the twist angle, as opposed the tilt angle, is a more vital factor in inhibiting the transmission of cracks through GBs. Additionally, for the WR-L specimen, it is difficult to individually evaluate the influence of the geometric parameters since they were outweighed by the influence of SFs. Notwithstanding, the overall lower values of twist and tilt angles in the AM-H-HIP specimen than those in the WR specimen support our hypothesis surrounding the role of the parameters in the inferior fatigue crack-growth resistance of AM alloys.

Although emphasis was placed on the influence of GB misorientation in this chapter, it is worthwhile to concisely mention the role of annealing twin boundaries, a distinct feature between AM and WR samples. Considering that ATBs are effective to impede dislocation motion like GBs [9], the extremely low portion of ATBs in AM alloys appeared to have a significant impact on their poor fatigue resistance. However, our investigation of the WR-L specimen with a drill-hole suggested that the role of ATBs is nearly similar to that of GBs. Namely, it relies on the geometrical relationship between slip/crack planes in the AT and the matrix, as illustrated in Fig. 4.7 [10]. For instance, crystallographic cracks can penetrate into an ATB if the primary slip plane in the AT has a low twist angle with the crack-plane in the matrix, as manifested in Fig. 4.6 (*cf.* the twist angle of 13° between Grain 6 and AT1). Therefore, the role of ATBs seems to be varied according to different twin-matrix configurations. However, in order to gain a better understanding of the dominant role of this boundary, further experimental data on the interaction between arrested cracks and ATBs is required.

4.3.2 Torsional fatigue test results

In this section, the role of twist and tilt angles in the small crack behavior of AM alloy subjected to torsional cyclic loading is further examined. Fig. 4.8(a) features an SEM image of two cracks emanating from the EDM-notch, denoted as C01 and C02. Higher magnification views near the crack-tips reveal that cracks grew across GBs (indicated by dashed yellow lines) by a few microns in length (*cf*. Fig. 4.8(b) and (c)). Moreover, transgranular cracks propagated obliquely with respect to the notch direction, due to the crystallographic orientation of grains evidenced in Fig. 4.8(d), where GBs with misorientations less than and superior to 10° were represented by solid green and black lines, respectively.

Fig. 4.9 exhibits the crack-length as a function of the number of cycles, based on the plastic replica observation of the cracks emanating from the notch-tip (*cf*. Fig. 4.10). The crack-length is defined as the projected length onto the plane parallel to the notch-plane. The points at which the cracks encountered GBs were demarcated by a solid line for C01 and a dashed line for C02, with their colors corresponding to those of the GBs in Fig. 4.8(d). The results signify that crack-growth rates were heavily controlled by GBs. The overall crack-growth rate was apparently faster for C01, *i.e.*, the average values were $\approx 1\times10^{-12}$ m/cycle for C01 and $\approx 2\times10^{-13}$ m/cycle for C02. Moreover, after encountering an identical GB (black arrow in Fig. 4.8(d)), a greater stress amplitude (*i.e.*, 210 MPa) was required for C02 to penetrate the boundary than for C01 (*i.e.*, 170 MPa), as shown in Fig. 4.9.

The preceding results were also interpreted with respect to GB resistance to crystallographic cracking, since the cracks proliferated along the {111} slip planes (*cf*. Fig. 4.8(d)). The featured grains are labelled as per Fig. 4.8(d), *i.e.*, Grains 1 ~ 4. The calculated twist and tilt angles, along with the SFs for each {111} slip plane, are listed in Table 4.2. The activated slip systems (*i.e.*, crack-planes) adjacent to GBs are highlighted in bold font, while the slip systems associated with the lowest twist and/or tilt angles are underlined.

It is noteworthy that the prerequisite for crack-growth across GBs was the presence of favorable slip planes, not only with high SFs, but also with strong compatibility (both low twist and tilt angles). Regarding C01, the (111) and $(1\bar{1}1)$ planes in Grain 2 bore nearly identical SF and twist angle values, yet the crack radiated along the (111) plane in Grain 2 because of the lower tilt angle with the (111) plane in Grain 1. Meanwhile, the higher twist angle of the (111) plane in Grain 3, compared to that in Grain 2, appears to have induced crack-arrest for more than ten million cycles. Furthermore, in Grain 4, it is reckoned that the even lower tilt angle of the $(11\bar{1})$ plane than the $(\bar{1}11)$ plane encouraged the crack to escalate along the $(11\bar{1})$ plane, despite the higher twist angle. As for C02, the crack initiated along the $(\bar{1}11)$ plane in Grain 2, the relatively high twist angle of which seems to have hindered the growth through the GB between Grains 1 and 2.

Considering the aforementioned discussion points, twist and tilt angles are presumably the predominant factors governing the alloy's small, fatigue-crack resistance under torsional cyclic loading. This appears to contradict a result of the previous section in which the twist angle dominated fatigue-crack resistance, while the tilt angle played a secondary role under push-pull fatigue loading. Such a discrepancy can be attributed to the difference in the number of directions with the maximum crack-growth driving force, depending on the loading mode. For the crack-tip subjected to remote shear-stress, the principal shear-stress occurs solely along the direction parallel to the crack-plane [13], as depicted in Fig. 4.11. Conversely, the crack-tip subjected to remote normal stress has principal shear-stresses occurring in two directions (*cf.* Fig. 2.13(b)), allowing them to grow along a favorable slip plane - a potential reason for the lesser sensitivity to the tilt angle.

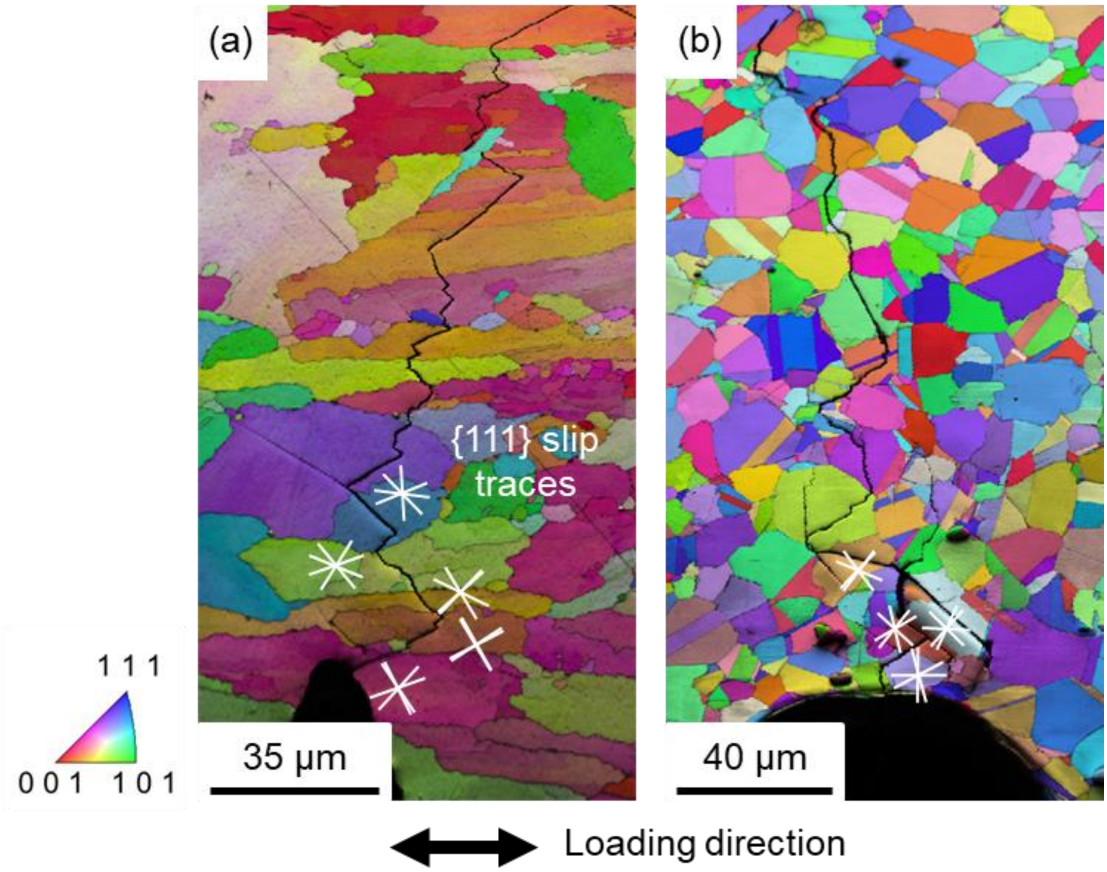

Fig. 4.3. Small, crack-growth behaviors near the threshold condition observed in: (a) EDM-notch specimen of AM-H-HIP; (b) drill-hole specimen of WR-L.

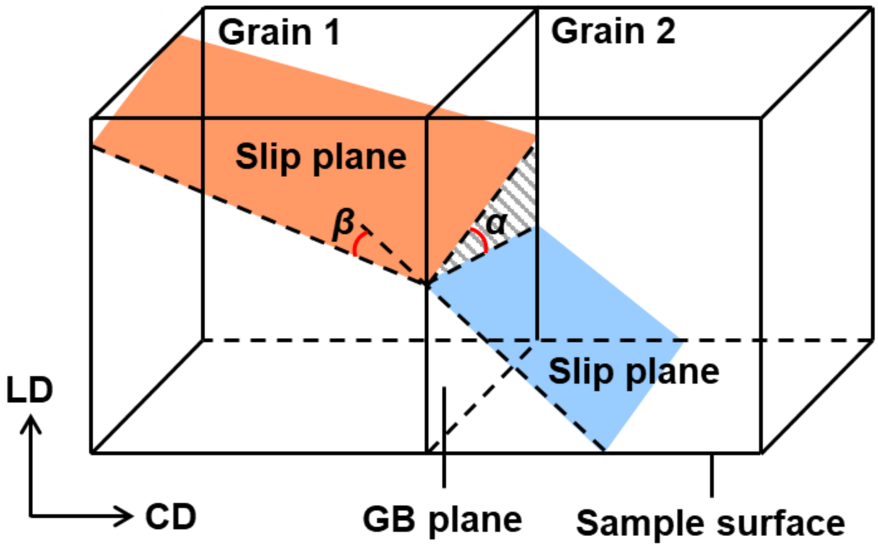

Fig. 4.4. Schematic of crystallographic crack-growth mechanism along slip planes between adjacent grains.

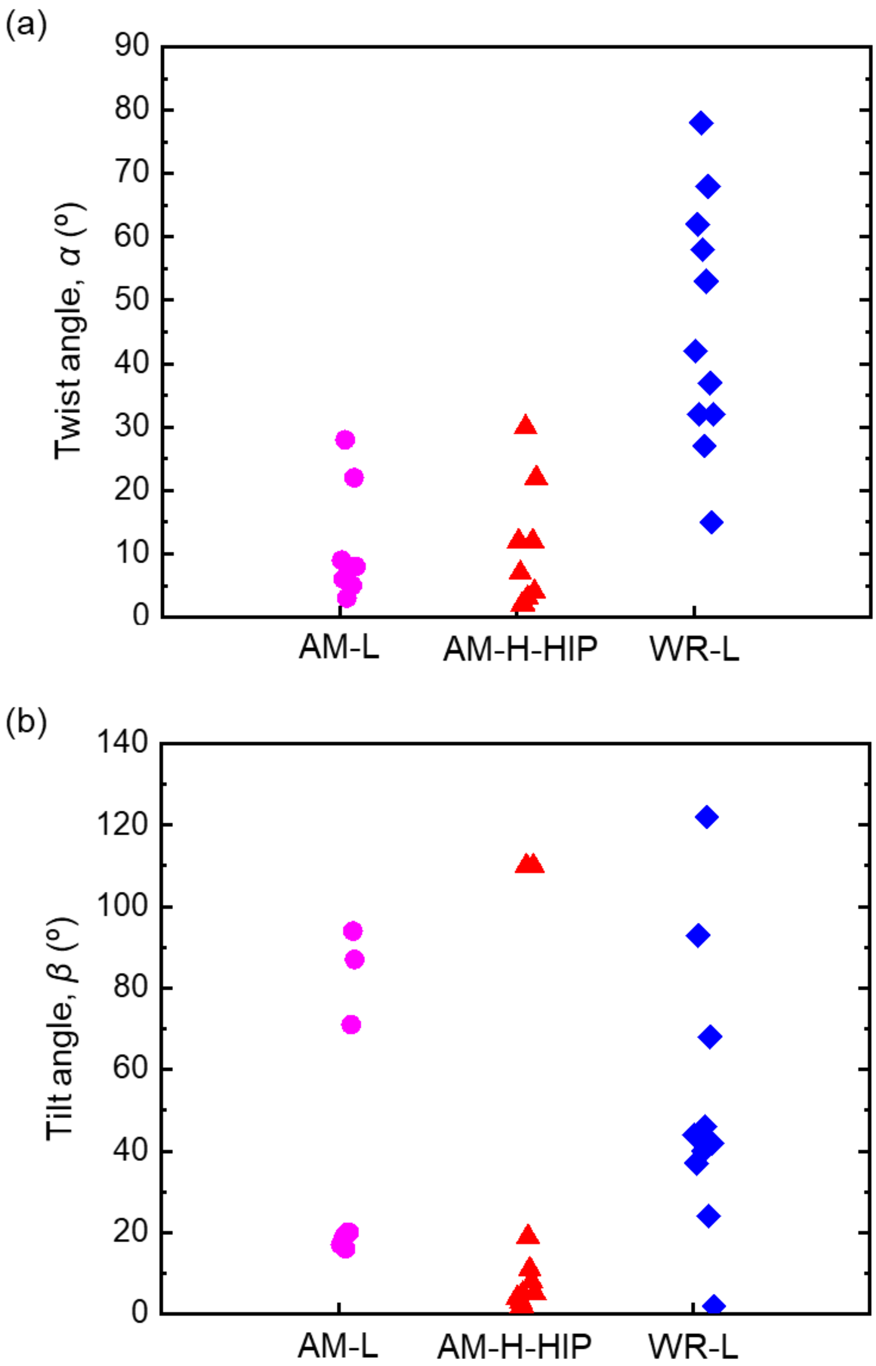

Fig. 4.5. Distribution of (a) twist and (b) tilt angles between neighboring crack-planes along the crack path.

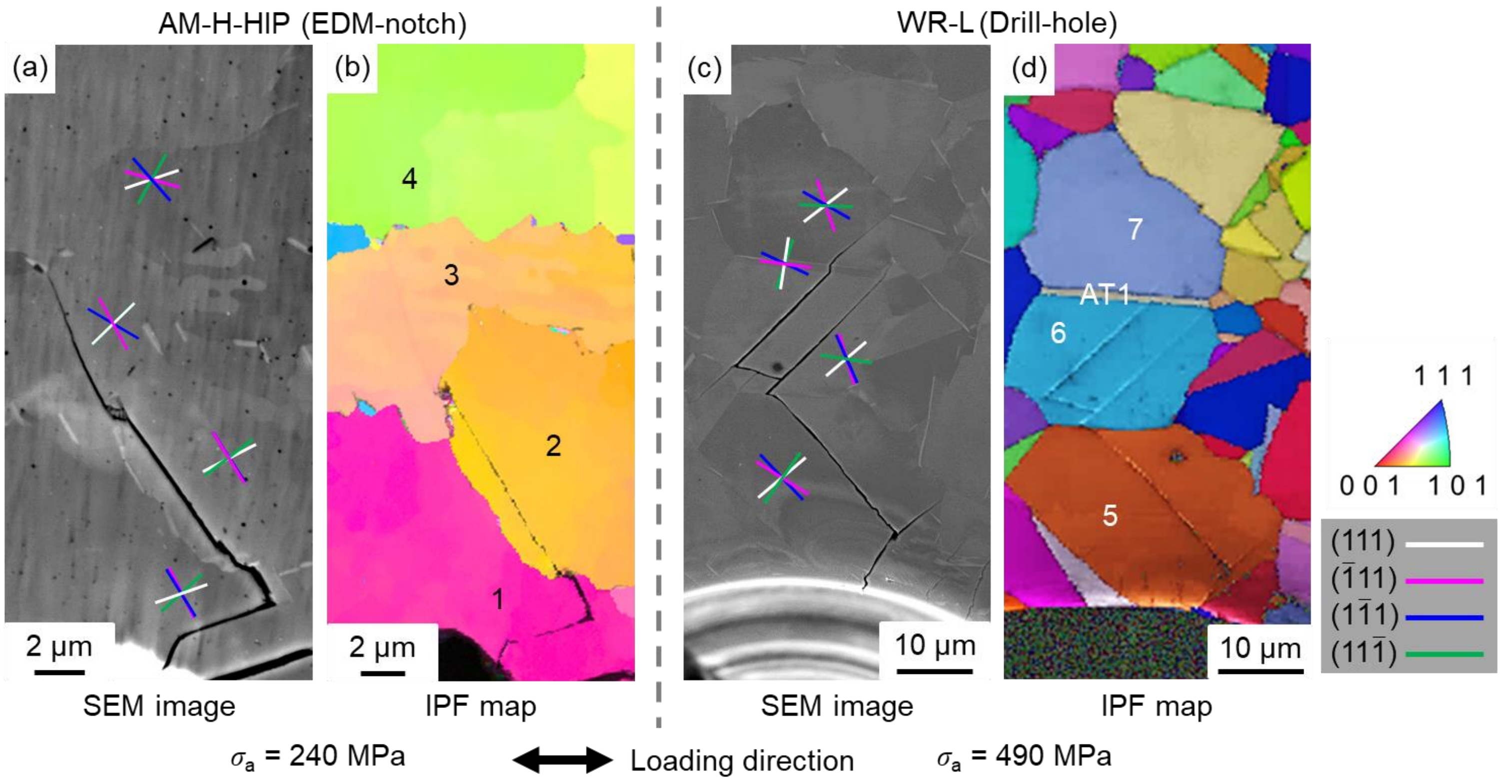

Fig. 4.6. SEM images and IPF maps of crack-growth behavior at the threshold condition: (a)(b) AM-H-HIP with EDM-notch specimen; (c)(d) WR-L with drill-hole specimen.

Table 4.1 Results of calculated SF, α and β values along crack-paths of the push-pull fatigue tests.

Grain	Slip planes	SF	α	β	Grain	Slip planes	SF	α	β
Grain 1	111	0.42	/	/	Grain 5	111	0.39	/	/
	$\bar{1}11$	**0.42**				$\bar{1}11$	0.33		
	$1\bar{1}1$	0.44				**$1\bar{1}1$**	**0.48**		
	$11\bar{1}$	0.48				$11\bar{1}$	0.47		
Grain 2	111	0.32	3	90	Grain 6	**111**	**0.43**	**68**	**93**
	$\bar{1}11$	**0.48**	**13**	**4**		$\bar{1}11$	0.27	29	27
	$1\bar{1}1$	0.46	93	5		$1\bar{1}1$	0.22	43	20
	$11\bar{1}$	0.41	110	80		$11\bar{1}$	0.13	107	38
Grain 3	111	0.49	31	74	AT1	**111**	**0.49**	**13**	**43**
	$\bar{1}11$	**0.49**	**10**	**1**		$\bar{1}11$	0.10	41	48
	$1\bar{1}1$	0.34	100	31		$1\bar{1}1$	0.30	98	65
	$11\bar{1}$	0.34	112	73		$11\bar{1}$	0.42	59	31
Grain 4	111	0.42	35	76	Grain 7	**111**	**0.45**	**37**	**44**
	$\bar{1}11$	0.13	44	41		$\bar{1}11$	0.32	38	27
	$1\bar{1}1$	0.49	43	9		$1\bar{1}1$	0.29	116	69
	$11\bar{1}$	0.45	54	62		$11\bar{1}$	0.03	41	83

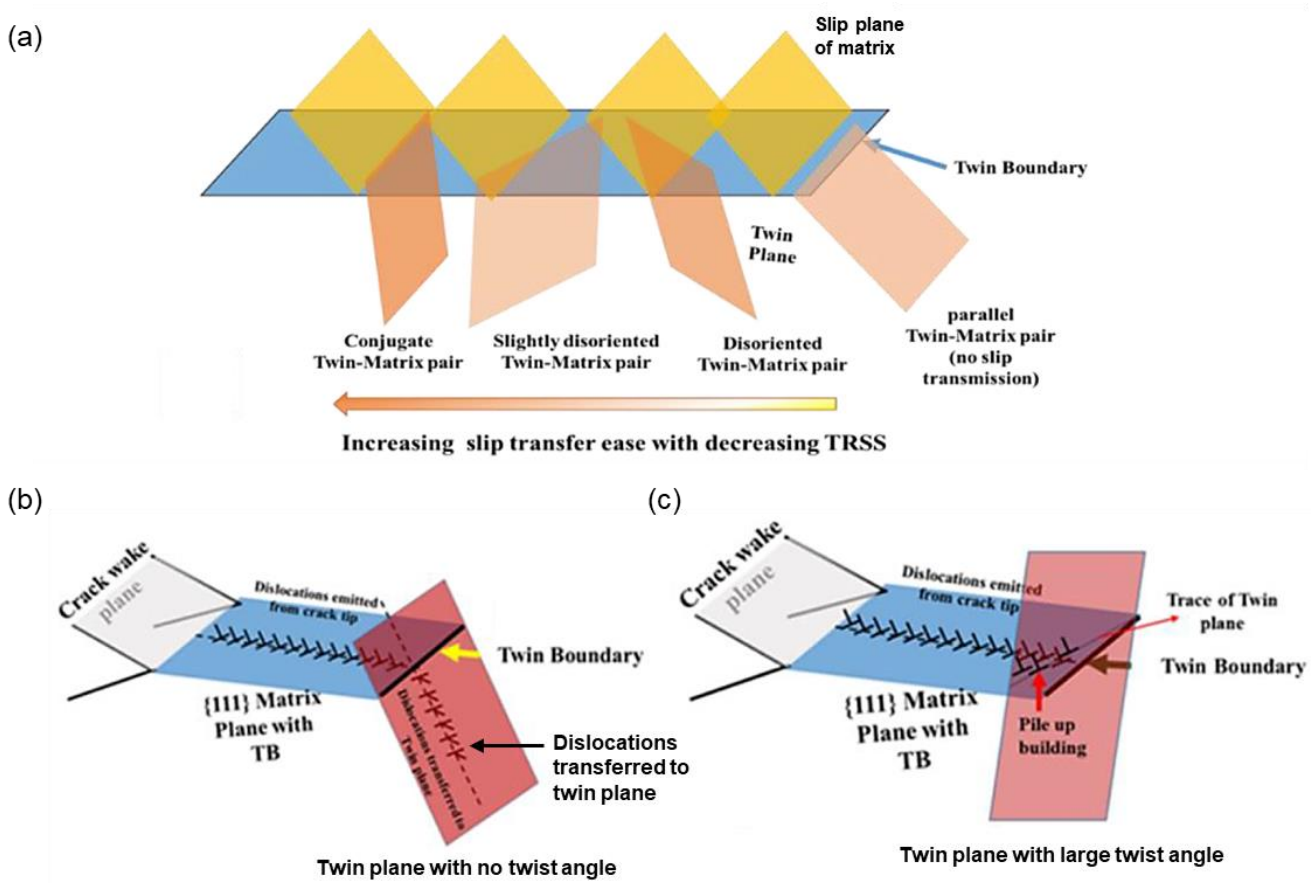

Fig. 4.7. (a) Geometrical relationship between slip/crack planes in the twin and the matrix; Dislocation-twin interaction in (b) twin boundaries with no twist angle; (c) twin boundaries with large twist angle.

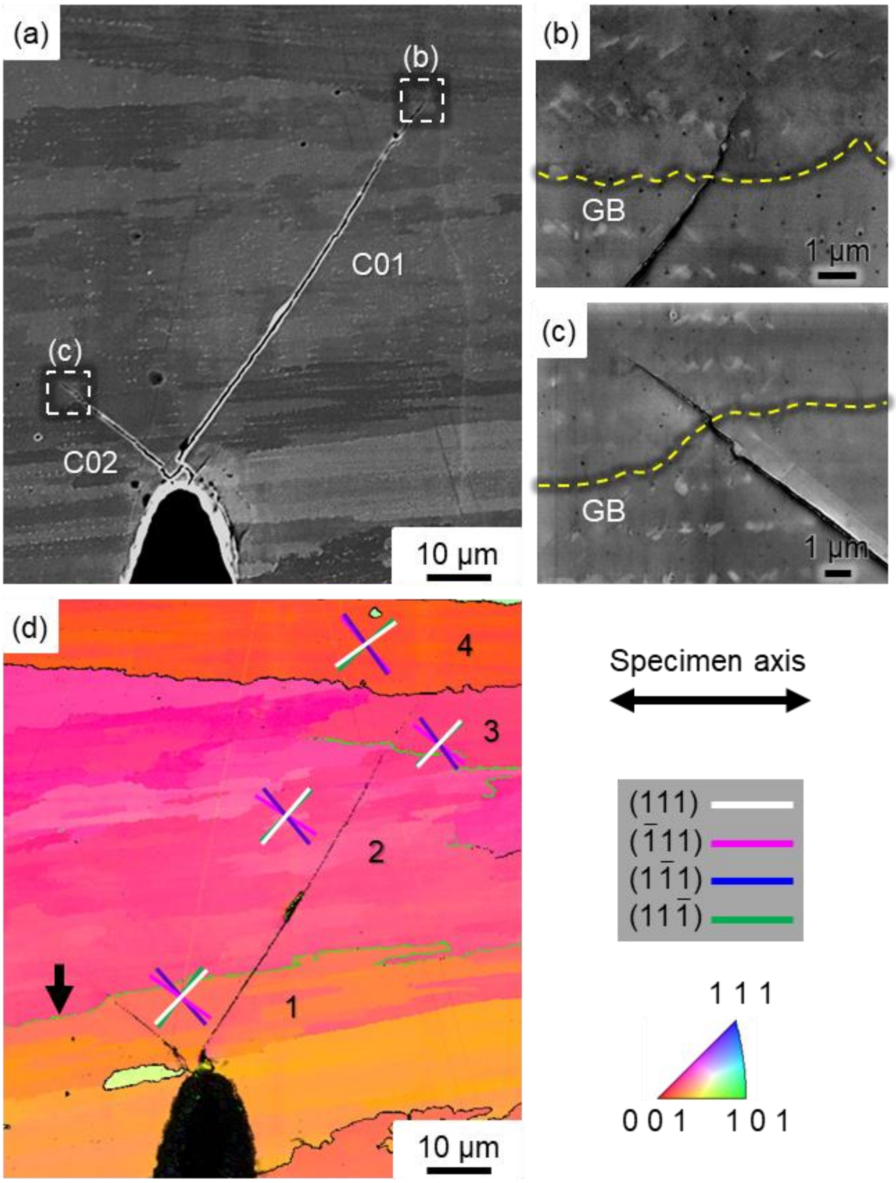

Fig. 4.8. (a) SEM image of cracks emanating from the notch observed *via* the torsional fatigue test using an EDM-notch specimen of AM-L; (b)(c) magnified views of the regions marked by dashed white squares in (a); (d) IPF map of (a).

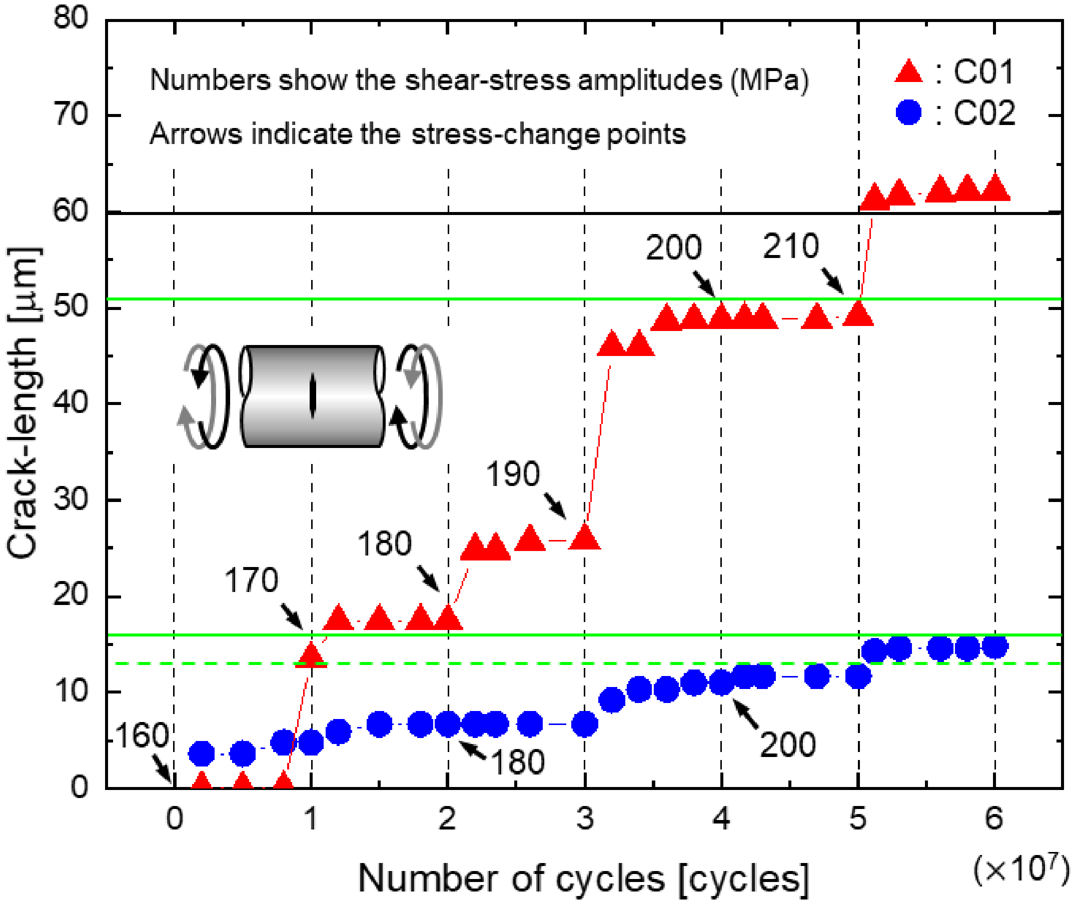

Fig. 4.9. Crack-growth curve obtained *via* the torsional fatigue test using an EDM-notch specimen of AM-L.

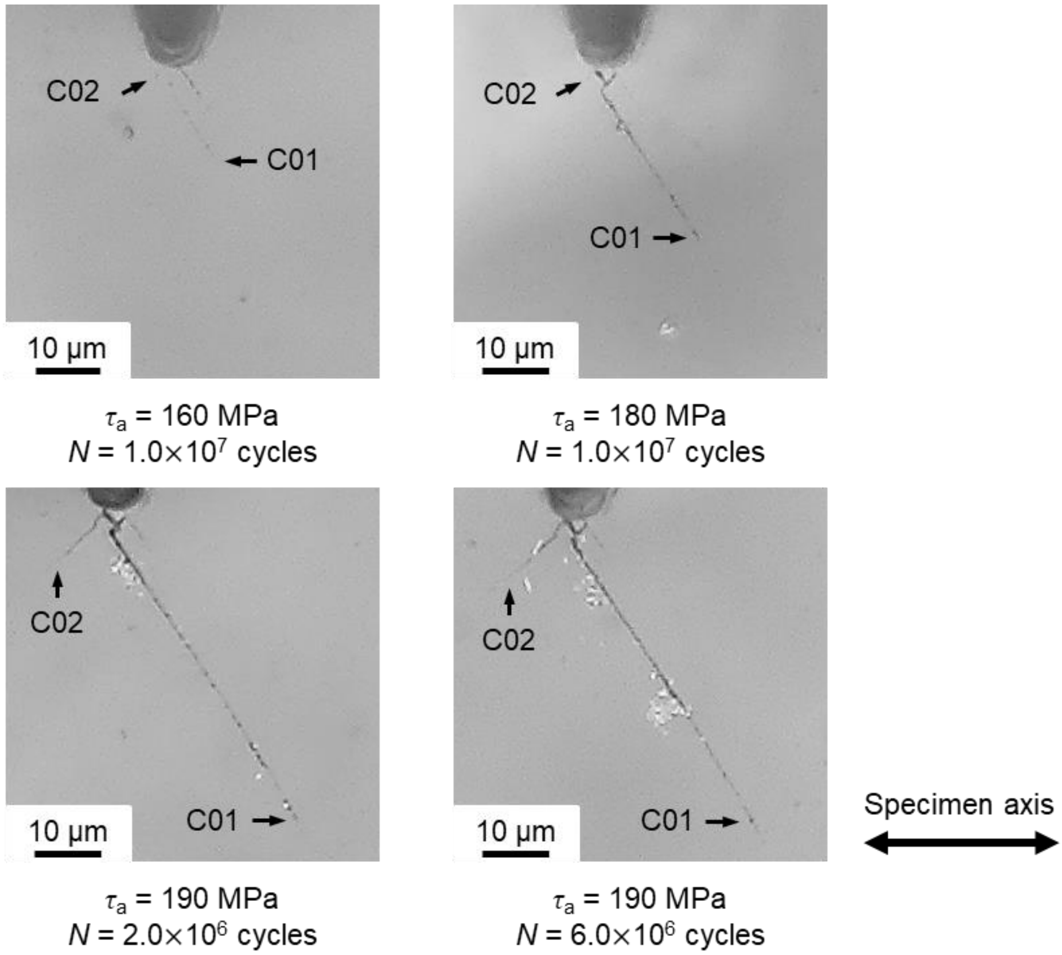

Fig. 4.10. Plastic replica observation of cracks emanating from the notch-tip obtained *via* the torsional fatigue test using an EDM-notch specimen of AM-L.

Table 4.2 Results of calculated SF, α and β values along crack-paths of the torsional fatigue test.

C01

Grain	Slip planes	SF	α	β	Grain	Slip planes	SF	α	β
Grain 1	**111**	**0.46**	/	/	Grain 3	**111**	**0.47**	**8**	**3**
	$\bar{1}11$	0.45				$\bar{1}11$	0.47	70	87
	$1\bar{1}1$	0.43				$1\bar{1}1$	0.40	80	76
	$11\bar{1}$	0.43				$11\bar{1}$	0.45	18	6
Grain 2	**111**	**0.47**	**4**	**4**	Grain 4	111	0.43	78	11
	$\bar{1}11$	0.44	88	79		$\bar{1}11$	0.45	6	84
	$1\bar{1}1$	0.47	5	84		$1\bar{1}1$	0.45	77	79
	$11\bar{1}$	0.39	90	1		$\mathbf{11\bar{1}}$	**0.44**	**18**	**4**

C02

Grain	Slip planes	SF	α	β	Grain	Slip planes	SF	α	β
Grain 1	111	0.46	/	/	Grain 2	111	0.47	74	85
	$\mathbf{\bar{1}11}$	**0.45**				$\mathbf{\bar{1}11}$	**0.44**	**10**	**3**
	$1\bar{1}1$	0.43				$1\bar{1}1$	0.47	83	15
	$11\bar{1}$	0.43				$11\bar{1}$	0.39	12	80

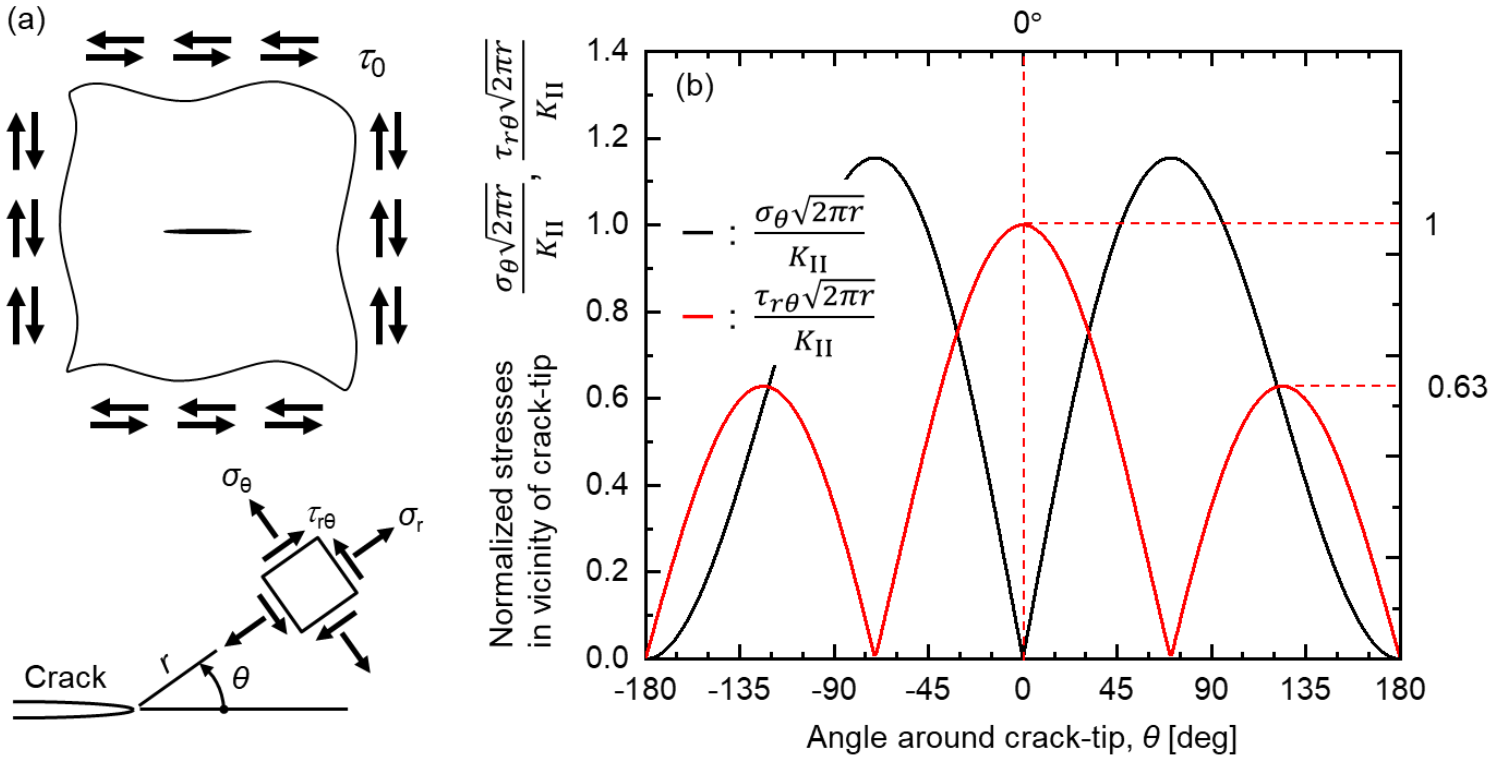

Fig. 4.11. (a) Definition of the stresses near the tip of a Mode II crack under remote shear stress; (b) normalized stresses as a function of an angle around crack-tip.

4.4 Conclusion

The current chapter aimed to explore the factors responsible for the reduced fatigue resistance observed in an additively-manufactured Ni-based superalloy (AM Alloy 718), primarily focusing on the impact of crystallographic texture and annealing twin boundaries. Through the push-pull and torsional fatigue testing near the threshold condition, the relationship between GB misorientation and small fatigue crack-growth resistance was investigated. The following conclusions were drawn:

1. The average value of twist angle along the paths of cracks generated during push-pull fatigue tests was substantially lower in the AM specimens than in the WR one. In addition, small cracks preferentially grew along favorable slip planes with low twist and/or tilt angles. The aforementioned results implies that the twist angle dominated fatigue-crack resistance, while the tilt angle played a secondary role under push-pull fatigue loading.

2. Similar to the GB misorientation, the role of ATBs was also interpreted based on the geometrical relationship between slip/crack planes in the twin and the matrix. Namely, in the presence of compatible relationships between the crack planes in both the twin and the matrix with a low twist angle, small cracks are expected to easily penetrate through ATBs. However, in order to enhance our understanding of the dominant role of this boundary, it is necessary to gather more experimental data on the interaction between arrested cracks and ATBs.

3. Under torsional fatigue loading, both the twist and tilt angles were likely to be the primary factors influencing the small fatigue crack resistance of the alloy. This observation seems to contradict the results obtained from push-pull fatigue tests. This discrepancy can be attributed to the variation in the number of directions with the maximum crack-growth driving force, which depends on the loading mode.

References

[1] Miao J, Pollock TM, Wayne Jones J. Microstructural extremes and the transition from fatigue crack initiation to small crack growth in a polycrystalline nickel-base superalloy. Acta Mater 2012;60:2840–54. https://doi.org/10.1016/j.actamat.2012.01.049.

[2] Lu K, Lu L, Suresh S. Strengthening materials by boundaries at the nanoscale. Science (80-) 2009;324:349–53.

[3] Nishikawa H, Furuya Y, Kitano H, Nakamura T, Kuwabara K, Kanegae Y, et al. In-situ observation of microstructurally small fatigue crack initiation and growth behaviors of additively-manufactured alloy 718. Mater Sci Eng A 2022;835:142682. https://doi.org/10.1016/j.msea.2022.142682.

[4] Kevinsanny, Okazaki S, Takakuwa O, Ogawa Y, Okita K, Funakoshi Y, et al. Effect of defects on the fatigue limit of Ni-based superalloy 718 with different grain sizes. Fatigue Fract Eng Mater Struct 2019;42:1203–13. https://doi.org/10.1111/ffe.12989.

[5] Zhai T, Wilkinson AJ, Martin JW. Crystallographic mechanism for fatigue crack propagation through grain boundaries. Acta Mater 2000;48:4917–27. https://doi.org/10.1016/S1359-6454(00)00214-7.

[6] Wei L, Pan Q, Huang H, Feng L, Wang Y. Influence of grain structure and crystallographic orientation on fatigue crack propagation behavior of 7050 alloy thick plate. Int J Fatigue 2014;66:55–64. https://doi.org/10.1016/j.ijfatigue.2014.03.009.

[7] Ma M, Wang B, Liu H, Yi D, Shen F, Zhai T. Investigation of fatigue crack propagation behavior of 5083 aluminum alloy under various stress ratios: Role of grain boundary and Schmid factor. Mater Sci Eng A 2020;773:138871. https://doi.org/10.1016/j.msea.2019.138871.

[8] Zhang X, Dunne FPE. 3D CP-XFEM modelling of short crack propagation interacting with twist/tilt nickel grain boundaries. J Mech Phys Solids 2022;168:105028. https://doi.org/10.1016/j.jmps.2022.105028.

[9] Schneider M, George EP, Manescau TJ, Záležák T, Hunfeld J, Dlouhý A, et al. Analysis of strengthening due to grain boundaries and annealing twin boundaries in the CrCoNi medium-entropy alloy. Int J Plast 2020;124:155–69. https://doi.org/10.1016/j.ijplas.2019.08.009.

[10] Barat K, Ghosh A, Doharey A, Mukherjee S, Karmakar A. Crystallographic evaluation of low cycle fatigue crack growth in a polycrystalline Ni based superalloy. Int J Plast 2022;149:103174. https://doi.org/10.1016/j.ijplas.2021.103174.

[11] Miao J, Pollock TM, Wayne Jones J. Crystallographic fatigue crack initiation in nickel-based superalloy René 88DT at elevated temperature. Acta Mater

2009;57:5964–74. https://doi.org/10.1016/j.actamat.2009.08.022.

[12] Jiang R, Karpasitis N, Gao N, Reed PAS. Effects of microstructures on fatigue crack initiation and short crack propagation at room temperature in an advanced disc superalloy. Mater Sci Eng A 2015;641:148–59. https://doi.org/10.1016/j.msea.2015.05.065.

[13] Erdogan F, Sih GC. On the Crack Extension in Plates Under Plane Loading and Transverse Shear. J Basic Eng 1963;85:519–25. https://doi.org/10.1115/1.3656897.

5. Concluding remarks

Ni-based superalloy 718 (Alloy 718) has been extensively used for components operating in extremely severe environments and loading conditions (*e.g.*, rocket engines), owing to its outstanding mechanical properties including fracture toughness, creep and fatigue strength, as well as its excellent corrosion resistance in a wide range of temperatures. Notwithstanding, such exceptional properties also hinder the machinability of the alloy into near-net-shape products for which there exists a high demand. Thus, over the past decade, additive manufacturing (AM) has attracted much attention as a next-gen production method for Alloy 718 parts with complex shapes. This novel method presents the possibility of achieving complex geometries and cost-efficient manufacturing. Nevertheless, the widespread adoption of additively-manufactured (AM) Alloy 718 is hindered by concerns regarding their mechanical integrity, which stems from innate features of AM materials such as crystallographic texture, micro-segregation, residual stresses and defects. Considering that Alloy 718 is commonly employed in critical applications like aerospace, where components endure numerous loading cycles during operation, the high-cycle fatigue properties of the alloy play a crucial role in ensuring the structural integrity and safety of critical systems. However, the comprehensive understanding of the influence of these factors on the fatigue strength of AM Alloy 718 is still lacking.

To address the aforementioned issue, the present study aimed to investigate the fatigue limit of AM Alloy 718 by performing torsional and push-pull fatigue tests with specimens having various microstructures and defects, focusing primarily on the impact of the AM features. Given the extensive documentation on the significant influence of small defects in the fatigue behavior of various materials, the initial phase of this study was dedicated to the quantitative evaluation of the effect of defects on the fatigue limit of AM Alloy 718, from the viewpoint of a small crack problem. Based on the macro- and microscopic analyses of the crack arresting mode at the fatigue limit, the determining mechanism of the fatigue limit and fatigue threshold were examined. Following it, the study took a systematic approach to explore the impact of other microstructural factors on the fatigue strength of the AM alloy, utilizing multi-scale electron microscopic analysis. The achievements in this study are summarized as follows:

1. Torsional and push-pull fatigue tests were performed on the AM Alloy 718 sample to examine the influence of defects on fatigue limit. The AM sample exhibited coarse and elongated grains with a strong crystallographic texture along the [001] crystal direction in relation to the build direction (BD). Additionally, both Laves and δ phases were detected within the interiors of the grains and along the grain boundaries (GBs). Based on non-propagating crack observation, it was suggested that the fatigue limit in each case is the threshold condition of a shear-mode, small fatigue-crack propagation. Therefore, the shear-mode, fatigue-crack growth-threshold, $\Delta K_{\tau th}$, was estimated and the following relationship between the $\Delta K_{\tau th}$ and defect size was obtained, $\Delta K_{\tau th} = 0.50(\sqrt{area})^{1/3}$, implying not only a crack-size dependence of shear-mode threshold but also a significantly poor fatigue resistance of AM material, as compared to wrought (WR) materials.

2. The influence of precipitates (*i.e.*, γ'', Laves and δ phases), grain size and residual stress was examined to elucidate the dominating factor responsible for inferior fatigue resistance of AM Alloy 718. A new AM sample (AM-H-HIP), processed with higher energy density and subjected to hot isostatic pressing (HIP), showed a relatively fine-grained microstructure in which Laves phases and intergranular δ phases, observed in the previous AM sample (AM-L), were completely dissolved. In addition, it was presumed that the residual stress that might exist in as-built AM sample can be completely eliminated by HIP. Through push-pull fatigue tests using specimens with as-built surface and a notched specimen, it was proposed that the fatigue limit of all the samples was also governed by the shear-mode, fatigue-crack growth-threshold, $\Delta K_{\tau th}$. The estimation of $\Delta K_{\tau th}$ revealed that the different microstructures between two AM samples resulted in minor difference in fatigue threshold, implying that precipitates, grain size and residual stress are not responsible for inferior fatigue resistance of AM alloys.

3. To elucidate the potential factors behind the reduced fatigue resistance observed in AM Alloy 718, the influence of crystallographic texture and annealing twin boundaries (ATBs) was examined. To this end, a push-pull fatigue test using a WR-L drill-hole specimen and torsional fatigue test using an AM-L EDM-notch specimen were conducted at/near the fatigue limit. Based on the small, fatigue

crack-growth behavior, the role of GBs and ATBs in crystallographic fatigue crack resistance was investigated in terms of the geometric parameters between crack planes of adjacent grains, such as twist and tilt angles. As a result, the average value of twist angle along the crack paths generated during push-pull fatigue tests was substantially lower in the AM specimens than in the WR one. Moreover, it was revealed that the twist angle dominated fatigue-crack resistance, while the tilt angle played a secondary role. The role of ATBs could also be interpreted with the geometric parameters. In contrast to push-pull loading, it is likely that both the twist and tilt angles play a crucial role in determining the small, fatigue-crack resistance of the alloy during torsional fatigue loading, which can be attributed to the differences in the number of directions of the maximum crack-growth driving force.

4. Taking into consideration all of the preceding discussion points raised in this study, it seems that a significant percentage of low GB misorientation angles (*i.e.*, low twist angle under push-pull loading and low twist/tilt angles under torsional fatigue loading) is the principal contributor to poor, small fatigue-crack resistance in AM Alloy 718. However, the current conclusion is based on very limited experimental findings. In addition, the combined effects of multiple factors may possibly hinder a more thorough understanding of their individual roles, potentially limiting the significance of this work. Nonetheless, this study provides a better insight into the influence of the inherent microstructural features of AM parts on the shear-mode, fatigue-crack threshold, aided by multi-scale electron microscopic analysis. In order to shed more light on this issue, further extensive experimental studies will be required, using AM samples with diverse microstructures that have been tailored by varying process parameters and/or post-heat treatments. This will be the focus of future phases of our research.

Acknowledgements

During my Ph.D. of about 3 years, I received so much guidance and support from professors, colleagues, and friends. This thesis could not have been completed without their help and encouragement. I would like to express my gratitude to all of them who have helped me a lot.

Firstly, I would like to express my sincere gratitude to my supervisor, Prof. Hisao Matsunaga who guided me wholeheartedly during my Ph.D. Thanks to his academically rigorous and sincere guidance, discussion, and consideration, I was able to complete the thesis. In addition to research, Prof. Matsunaga took care of me so that I could adapt well to life in Japan. Most of all, I would like to express my deepest appreciation for his thoughtful care and support whenever I encountered the difficult time.

I also would like to sincerely appreciate Prof. Hiroyuki Toda and Prof. Shigeru Hamada, the members of this thesis committee for taking the time to review and evaluate the thesis. The valuable comments and suggestions have been of great help in enhancing the completeness of this thesis.

I would like to sincerely thank Dr. Yuya Tanaka (assistant professor at Fukuoka university), Dr. Yuhei Ogawa (former assistant professor of Kyushu University) and Dr. Saburo Okazaki (Kobe Material Testing Laboratory Co., Ltd.) who gave me invaluable research advice and discussion, experimental help, and kind consideration as a sen-pai of Prof. Matsunaga Laboratory. I also would like to thank all of the members of our laboratory for helping me so that I could adapt well to life in the laboratory. In addition, I would like to thank all the members of Research Center for Hydrogen Industrial Use and Storage (HYDROGENIUS) of Kyushu university for their patiently help and support for research activities.

I would like to express my sincere gratitude to Prof. Joon-Hyun Lee (Pusan national university) who gave me a lot of guidance and encouragement so that I could decide to study the field of fatigue and fracture in Japan. Above all, he greatly helped me to build the invaluable relationship with Prof. Matsunaga. In addition, I would like to thank Prof. Myoung-Hwan Kim (Korea Maritime and Ocean University) who have given me countless precious advice as a great mentor since I had entered Korea Maritime and Ocean University. His continuous encouragement made me not to give up to challenge to study in Japan. I also would like to sincerely appreciate Prof. Kyung-Hun Lee (Korea Maritime and Ocean University), my former supervisor during master course who have led me to grow further not only as a researcher but also as a person. His sincere guidance and consideration have been of great help in building a solid research foundation.

I would like to express my sincere gratitude to my family, Sujin and friends. Thanks to their love and support, I was able to complete my Ph.D.

This study was conducted as part of a collaborative research project among the Japan Aerospace Exploration Agency (JAXA), Kyushu University, the National Institute for Materials Science (NIMS), Metal Technology Co., Ltd., Sanyo Special Steel Co., Ltd. and Matsuura Machinery Corporation. I am grateful to all the members within this project for material fabrication and useful discussion on the fatigue properties of additively-manufactured Alloy 718.

This work was partially supported by the Japan Society for the Promotion of Science Grants-in-Aid for Scientific Research – JSPS KAKENHI (Grant Number 22J12181/23KJ1672).